

The Pennsylvania State University
The Graduate School
College of Engineering

**VIBRATION OF CARBON NANOTUBES WITH
DEFECTS AND THEIR COMPOSITES:
REDUCED-ORDER MODEL AND DAMPING**

A Dissertation in
Mechanical Engineering
by
Robert B. Hudson

©2018 Robert B. Hudson

Submitted in Partial Fulfillment
of the Requirements
for the Degree of

Doctor of Philosophy

August 2018

The dissertation of Robert B. Hudson was reviewed and approved* by the following

Alok Sinha
Professor of Mechanical Engineering
Dissertation Adviser
Chair of Committee

Ruben Kraft
Assistant Professor of Mechanical Engineering

Adri van Duin
Professor of Mechanical Engineering

Mauricio Terrones
Distinguished Professor of Physics, Chemistry and Materials Science & Engineering

Mary Frecker
Professor of Mechanical Engineering
Associate Head of Graduate Programs

*Signatures on file in the Graduate School

Abstract

Carbon nanotubes, and the composites made from them, promise properties unrivaled by more traditional materials. To fully understand, predict, and tune those properties, a plethora of technical and theoretical challenges must be overcome. One such challenge is to find a technique with which to predict the dynamic behavior of carbon nanotubes containing defects. The dynamics of pristine carbon nanotubes are relatively well understood, but their analysis relies heavily on the periodic nature of their structure. When that structure is altered, these analyses are no longer valid. A new model is therefore needed that can incorporate these defects but is still computationally efficient enough to be coupled with a model of a composite matrix and have its vibrational characteristics analyzed under a range of conditions.

In this dissertation, a model of a metallic matrix carbon nanotube composite is developed by first examining the dynamics of two well-known damping models — the microslip and macroslip models. This analysis focuses on the implications of substituting the simpler macroslip models in place of the more mathematically complex microslip model. Specifically, the ability of these two damping models to predict the stability of a system subjected to self-exciting aeroelastic interactions (flutter) is considered. It is discovered that the microslip damper, while capable of stabilizing this system within a certain range of amplitudes, will always dissipate less energy than an equivalent macroslip damper vibrating at the same amplitude. The energy dissipation/amplitude relationships developed here are later employed to characterize the nature of the damping provided by a carbon nanotube composite.

This study of generalized damping models is followed by the application of order reduction methods to defect-bearing carbon nanotubes. First, isotope and Stone-Wales defects are considered, and two well-known order reduction methods, modal domain analysis and modified modal domain analysis, are adapted for use on these atomic-scale systems. These models are demonstrated to predict the natural frequencies and normal modes of the defect-bearing carbon nanotubes with high accuracy, while greatly decreasing the computational costs associated with these calculations. Furthermore, this analysis reveals that even defects as ubiquitous and insignificant as the variation of isotopes within a carbon nanotube can produce large changes in the mode shapes of the resulting structure.

The third and final defect that is considered is a multi-vacancy defect, which results in an even greater change to the structure of a carbon nanotube. As this type of defect removes atoms from the system, previous methods of order reduction are not applicable to it. Instead, a novel method of order reduction is developed, called modal domain reduction that, by combining elements of modal domain analysis and dynamic reduction with a new technique for handling the decrease in the number of degrees of freedom in the system,

permits the vibrational properties of the system to be calculated efficiently and accurately.

Finally, these order reduction techniques for individual carbon nanotubes are incorporated into a model of an aluminum matrix carbon nanotube composite. The composite itself is represented by a reduced-order model, created by applying Guyan, or static, reduction to the full-order matrix model. The interactions between the carbon nanotube and the matrix are calculated using the Lennard-Jones model. Several models of composites, some with pristine carbon nanotubes and other with carbon nanotubes containing a Stone-Wales or a multi-vacancy defect, are subjected to cyclic loading to determine their damping properties. The validity of these models is established through comparisons to published experimental results, and the nature of the observed damping is characterized in terms of the microslip and macroslip damping.

Contents

List of Figures	viii
List of Tables	xi
Acknowledgements	xii
1 Introduction and Literature Review	1
1.1 Introduction	1
1.2 Literature Review	3
1.2.1 Carbon Nanotubes	3
1.2.2 Defects in Carbon Nanotubes	4
1.2.3 Carbon Nanotube Composites	6
1.2.4 System Order Reduction	8
1.3 Organization of this Dissertation	10
2 Background on Crystal Lattices and Carbon Nanotubes	12
2.1 Introduction	12
2.2 The Structure of a Carbon Nanotube	13
2.3 Derivation of the Eigenvector Problem for an Atomic Lattice from the Interaction Tensor Representation	16
3 Microslip Damping	22
3.1 Introduction	22
3.2 Microslip Friction Model	24
3.3 Single Degree of Freedom Model, Nondimensionalization and Describing Function Analysis	27
3.4 Numerical Results and Discussion	30
3.5 Conclusion	32
4 Reduced-Order Models of Carbon Nanotubes: Isotope and Stone-Wales Defects	34
4.1 Introduction	34
4.2 Methods	36
4.2.1 Order reduction techniques	39
4.2.2 Modal domain analysis	41
4.2.3 Modified modal domain analysis	42

4.2.4	Defects	43
4.3	Numerical results	47
4.4	Discussions	55
4.5	Conclusion	57
5	Reduced-Order Models of Carbon Nanotubes: Multi-Vacancy Defects	60
5.1	Introduction	60
5.2	Methods	61
5.2.1	Molecular Dynamics	61
5.2.2	Linearization	63
5.2.3	Order reduction	65
5.3	Estimation of Errors in MDA and MDR	68
5.3.1	Modal domain analysis (MDA)	68
5.3.2	Modal domain reduction (MDR)	70
5.4	Numerical Results and Discussions	72
5.5	Conclusion	80
6	Reduced-Order Modeling of Damping in Aluminum/Carbon Nanotube Composites	81
6.1	Introduction	81
6.2	Methods	83
6.2.1	Overview	83
6.2.2	Simulation Geometry	85
6.2.3	Elastic Interactions	90
6.2.4	Lennard-Jones Interactions	91
6.2.5	Solving Constrained Equations of Motion Using the Conjugate Gradient Method	94
6.3	Results	98
6.3.1	Stiffness	99
6.3.2	Damping as a Function of Vibration Amplitude	100
6.4	Discussion	103
6.5	Conclusion	108
7	Conclusion and Future Work	110
Appendix A Derivation of the Nondimensionalized Single Degree of Freedom Equations of Motion		113
Appendix B Energy Dissipation by Macroslip and Microslip Dampers in Full Slip Conditions		116
Appendix C Proof That the Sum of MAC Values of a Vector and Its Basis is 1		119
Appendix D Supplemental Numerical Analyses of Carbon Nanotubes with Multi-Vacancy Defects		120

Appendix E Loss Factor of a Macroslip Damper in Parallel with a Spring	124
Bibliography	126

List of Figures

2.1	Atoms A and B are mirror images of each other. An atom each of type A and B must be included in a unit cell for graphene.	14
2.2	The hexagonal lattice of graphene, with the carbon atoms represented as gray dots. The dotted lines indicate the boundaries of a representative unit cell.	15
2.3	A strip of graphene that could be rolled into a carbon nanotube. The dotted lines represent the cuts in the graphene sheet that form the strip. \mathbf{c} is the chiral vector and \mathbf{t} is the translation vector.	16
3.1	Schematic of microslip damper	25
3.2	Hysteresis curves of microslip and macroslip damper systems	25
3.3	Dimensional single degree-of-freedom system	28
3.4	Nondimensional single degree-of-freedom system	28
3.5	Amplitudes of limit cycles	30
3.6	Simulated response for initial conditions corresponding to point A in Fig. 3.5	30
3.7	Simulated response for initial conditions corresponding to point B in Fig. 3.5	31
3.8	Phase portrait of response with microslip damper	31
3.9	Comparison of energy dissipated by macroslip and microslip dampers	33
4.1	A (4,4) CNT with the unit cell highlighted and boxed. Note that the unit cell is not of minimal size—this is to ensure that the cell is large enough to contain an entire SWD.	40
4.2	The formation of an SWD via the rotation of a carbon-carbon bond. Note that this transformation results in a system that requires equilibration.	46
4.3	Arrangement of atoms in the isotope defect case, prior to graphene being rolled into a nanotube. ^{12}C atoms represented in blue, ^{13}C in red.	48
4.4	Structure of a CNT with an SWD. Defect circled in red. Three-dimensional rendering performed with visual molecular dynamics [112].	49
4.5	Vibrational frequencies of a pristine (4,4) CNT, as well as the same CNT with an SWD, and the approximations of the perturbed system using MDA and MMDA.	51
4.6	Frequency deviation of a (4,4) CNT with isotope defects.	51
4.7	Frequency deviation of a (4,4) CNT with a single SWD.	52
4.8	MAC of MDA modes versus full-order modes— <i>isotope defects</i>	53
4.9	MAC of MMDA modes versus full-order modes— <i>isotope defects</i>	53
4.10	MAC of pristine modes versus full-order modes— <i>isotope defects</i>	53
4.11	MAC of MDA modes versus full-order modes— <i>SWD</i>	53

4.12	MAC of MMDA modes versus full-order modes—SWD.	54
4.13	MAC of pristine modes versus full-order modes—SWD.	54
4.14	Participation factors for a CNT with isotope defects.	55
4.15	Participation factors of a CNT with an SWD.	55
4.16	Maximum atom displacement of mode 51 from the full-order model, and as predicted by MMDA and MDA results.	58
5.1	Detail of a four atom multi-vacancy in a (10,0) nanotube (a) before and (b) after simulated annealing and quenching. Figure generated using VMD [112].	62
5.2	Detail of a two atom multi-vacancy in a (10,10) nanotube (a) before and (b) after simulated annealing and quenching. Figure generated using VMD [112].	63
5.3	Natural frequencies of the pristine and perturbed (10, 0) CNT, with predicted frequencies found using MDA and MDR	74
5.4	Errors in predicted natural frequencies of the (10,0) CNT	74
5.5	Natural frequencies of the pristine and perturbed (10,10) CNTs, with the frequencies predicted by MDA and a) MDR with $\omega = 0$ and b) MDR with $\omega = 1.8\text{THz}$	75
5.6	Errors in the natural frequencies of the (10,10) CNT predicted by MDR . . .	76
5.7	MAC values of the MDR reduced-order system versus the full-order perturbed system for the (10, 0) CNT	77
5.8	MAC values of the MDR reduced-order system versus the full-order perturbed system for the (10, 10) CNT, with a) an input frequency of 0 Hz b) an input frequency of 1.8 THz	77
5.9	Sum of MAC values of the pristine system versus the full-order perturbed system for the (10, 0) CNT	78
5.10	Average error of the first 100 natural frequencies of the (10,10) CNT versus computational times as the size of the reduced-order model is varied. Arrows indicate direction of increasing n_r	79
6.1	Flowchart of the solution procedure	85
6.2	Example of the composite geometry, rendered in VMD [112]. Carbon-carbon bonds are red and aluminum atoms are shown in blue.	86
6.3	A schematic representation of the loading applied to a unit cell of the composite simulation. The hatching at the ends of the block of composite material indicate that the atoms on those planes are prevented from moving parallel to the CNT.	87
6.4	Representative hysteresis curves for Al/CNT composites with various defects undergoing a cyclic load with amplitude $0.21\text{ eV}/\text{\AA}$	101
6.5	Representative hysteresis curves for Al/CNT composites with the distance between loading and unloading curves exaggerated by a factor of six	101
6.6	Energy dissipation per cycle for Al/CNT composites as a function of maximum strain	102
6.7	Loss factors for the Al/CNT composites as a function of maximum strain. Error bars indicate standard error based on five trials.	107

D.1	Frequency (a) and frequency error (b) for MDR ($\omega = 0$) and MDA approximations of a (6,6) CNT with a single 2-atom MVD.	121
D.2	Frequency (a) and frequency error (b) for MDR ($\omega = 0$) and MDA approximations of a (6,6) CNT with a single 4-atom MVD.	121
D.3	Frequency (a) and frequency error (b) for MDR ($\omega = 0$) and MDA approximations of a (10,0) CNT with a single 2-atom MVD.	122
D.4	Frequency (a) and frequency error (b) for MDR ($\omega = 0$) and MDA approximations of a (10,10) CNT with a single 4-atom MVD.	122
D.5	Frequency (a) and frequency error (b) for MDR ($\omega = 0$) and MDA approximations of a (17,0) CNT with a single 2-atom MVD.	123
D.6	Frequency (a) and frequency error (b) for MDR ($\omega = 0$) and MDA approximations of a (17,0) CNT with a single 4-atom MVD.	123

List of Tables

2.1	Components of the interaction tensor of graphitic carbon in dynes/cm, from [5].	21
6.1	Relative stiffnesses of Al/CNT composites with various defects	100

Acknowledgements

I would first like to thank my advisor, Dr. Sinha, without whom this dissertation would not have been possible. Through his patience guidance and his immense knowledge, Dr. Sinha not only helped me overcome the problems that emerged in researching, but he also demonstrated what it means to be an insightful researcher and a thoughtful mentor. I am equally grateful for the example he set for me and for the skills and information he taught me. I would also like to thank the other members of my committee, Dr. van Duin, Dr. Kraft, and Dr. Terrones, for their perceptive comments and questions, and their willingness to share with me their knowledge.

Over the course of this degree, my parents and my wife, Chelsea, have been a constant source of support and encouragement. In particular, I would like to thank Chelsea, who was always being there to cheer me up when things went badly, to share in my excitement when things went well, and to remind me that the hard work would be worth it in the end, all while pursuing her own PhD. It is to her that this dissertation is dedicated.

Research presented in this dissertation was supported in part by a Seed Grant award from the Institute for CyberScience at the Pennsylvania State University.

Chapter 1

Introduction and Literature Review

1.1 Introduction

Carbon nanotubes (CNTs), and the composites made from them, promise properties unrivaled by more traditional materials [1–3]. To fully understand, predict, and tune those properties, a plethora of technical and theoretical challenges must be overcome. One such challenge is to find a technique with which to predict the dynamic behavior of CNTs containing inevitable defects. The dynamics of pristine CNTs are relatively well understood, but the analysis of them relies heavily on the uniform nature of their structure [4, 5]. When that structure is altered, these analyses cease to be valid. A new model is therefore needed that can incorporate these defects but is still computationally efficient enough to be coupled with a model of a composite matrix and have its vibrational characteristics analyzed under a range of conditions.

The phonon dispersion of pristine CNTs, that is to say CNTs that do not have the periodicity of their structure interrupted, has been well studied [6, 7]. Numerical analyses of phonon dispersion of pristine CNTs rely on the assumption that the CNT is made up of an infinite number of repeating units — an assumption that is incorrect when defects are present. Growing interest in the use of CNTs as nanomechanical resonators for radio frequency applications [8], strain and pressure sensors [9] and mass sensors [10] require that

the vibrational response of realistic nanotubes — CNTs with defects — be fully understood.

There is a need for materials that combine high structural strength with the ability to damp vibrations, particularly in the construction of turbine rotors [11, 12]. Rotors are subject to fatigue and eventual failure if their vibration is insufficiently damped, as a result either of flutter (self-exciting aeroelastic interactions) [13] or to localized vibrations caused by mistuning [14]. These effects are frequently mitigated by attaching friction dampers to the rotor blades [15]. This increases the weight of the turbine, as well as the production costs. The development of composite materials that are strong enough for turbine applications and that also inherently possess the necessary damping properties would provide a simple and elegant solution to these problems. CNT composites not only promise these properties, but have already been used in applications that require high strength and significant material damping, ranging from bicycle frames to wind turbine blades [16]. However, the requirements for turbine rotors are more strenuous, and before such materials can be used models are required that can efficiently and accurately predict the behavior of parts constructed from them. As CNT composite will inevitably contain CNTs with defects in them, it is important the interaction between defect-bearing CNTs and the composite matrix in which they are embedded is examined.

The research presented here seeks to address some of these gaps in our understanding of the dynamics of defect-bearing CNTs. First, two damping models that have the potential to accurately model the behavior of CNT composites are compared, and their ability to stabilize a system subjected to flutter is discussed. Following that, changes to the vibrational properties of CNTs due to defects are investigated directly using order reduction techniques. These methods, which are common in structural dynamics literature, permit the properties of complex systems to be calculated efficiently by removing from the models those degrees of freedom that have minimal impact on the properties that are being examined. The resulting model allows the analysis of systems that would otherwise be too costly to simulate. Reduced-order models of CNTs containing isotope, Stone-Wales, and multi-

vacancy defects are developed, and their vibrational properties are analyzed and compared to those predicted by the corresponding full-order models. Two of the order reduction methods used here (modal domain analysis and modified modal domain analysis) are well-known in structural mechanics literature, however prior to this work they have not been used to model atomic-scale systems. The third order reduction method, modal domain reduction, is novel. Following the development of these reduced order models of CNTs, the models are incorporated into simulations of aluminum/CNT composites, and the impact of the defects is observed and characterized using the damping models that were developed initially. The research presented here represents the first time that order reduction methods are used to analyze and simulate defect-bearing CNTs.

1.2 Literature Review

1.2.1 Carbon Nanotubes

Since their discovery by Iijima in 1991 [17], carbon nanotubes have been at the forefront of research in nanotechnology. Like graphene, the structure of a carbon nanotube formed from carbon atoms bonded in an hexagonal lattice. To form a nanotube, a section of this lattice is ‘rolled’ into a cylinder. An individual cylinder is a single walled carbon nanotube (SWNT). If multiple such cylinders are nested within each one another, the structure is a multi-walled carbon nanotube (MWNT) [18]. Much of the interest in carbon nanotubes has been due to the theoretical prediction and later experimental confirmation of their remarkable mechanical and electrical properties. Reported Young’s moduli for SWCNTs are in excess of 1 TPa [19]. Other research has shown that the yield strength of a SWCNT is on the order of 50 GPa [20]. It should be noted, though, that measuring these properties at the nano-scale is no easy task, and the exact stiffness and strength of a SWCNT is a topic of ongoing research.

In addition to experimental studies, there has been a widespread effort to explain and predict the properties of carbon nanotubes theoretically and through numerical simulation [2].

There are two broad and sometimes overlapping categories into which these studies fall. One group of studies seeks to start at the atomic level, either by using first-principles approaches such as density functional theory or by employing molecular dynamics approaches [2,21–25]. The other group of studies approximates a carbon nanotube as a continuous solid, and tries to find parameters for established continuum models that will fit the measured results for carbon nanotubes [26–29]. The overlap between these two camps comes when the atomic structure of carbon nanotubes is considered, but the interatomic interactions are simplified to the point that the system has more in common with a discretized continuous system than a true molecular dynamics simulation [30–32]. These molecular structural mechanics models have the advantage that they are less computationally intensive than full-fledged molecular dynamics simulations, while still being sensitive to changes in the arrangement of atoms in the structure. However, like their continuum counterparts, they rely heavily on previous results (be they experimental or theoretical) to determine the properties of the structural elements that represent bonds and atoms.

1.2.2 Defects in Carbon Nanotubes

It has been hypothesized that many of the properties of carbon nanotubes rely so heavily on the structure of the nanotube that defects in the structure could radically change the behavior of the nanotube as a whole [1,2]. Studying carbon nanotubes containing defects — especially defects that appear irregularly in the nanotube — involves complications not found in pristine (defect-free) carbon nanotubes. A pristine carbon nanotube is a periodic structure, which is to say that the structure of the nanotube repeats itself after a certain distance. This allows a nanotube to be simulated by modeling a small section of its structure, with periodic boundary conditions [5]. When this periodicity is broken, for example by an irregular defect in the nanotube, a much larger simulation is usually required.

There are, generally speaking, four types of defects that can occur in carbon nanotubes (or graphitic structures in general). The first are vacancies, in which atoms are removed

from the structure but the remainder of the structure does not significantly change. The second are topological defects, which are caused by carbon atoms forming non-hexagonal rings. The third are rehybridization defects, in which some of the bonds between carbon atoms have an intermediate hybridized character, lying somewhere between sp^2 and sp^3 . The final type of defect is the presence of atoms of different materials, usually caused by doping or functionalization of the structure [33–35].

The importance of understanding the role defects play in determining the mechanical properties of carbon nanotubes has been emphasized by experiential studies examining the density of defects in typical nanotubes and the impact of these defects. One study found that a high quality carbon nanotube contains, on average, one defect per $4\mu\text{m}$ [36]. This low density makes an accurate simulation of these nanotubes especially difficult, as the total number of atoms involved would be extremely large. However, the consequences of defects was made clear by Gao *et al.*, who showed that a defect-rich carbon nanotube produced using pyrolysis was ten times weaker than a structurally more perfect nanotube formed using the electrical discharge method [37].

Several studies have attempted to numerically predict the properties of carbon nanotubes containing defects, using both molecular dynamics and molecular structural mechanics approached. In one such study, Zhang *et al.* [38] used molecular dynamics to investigate the fracture strength of carbon nanotubes containing vacancy defects. Elasticity was not investigated explicitly in this study, but the stress-strain curves for pristine and defective nanotubes suggest that the stiffness decreases in the presence of vacancies [38]. Sakharova *et al.* [39] looked specifically at the elasticity of carbon nanotubes with vacancies, and found a similar trend. In their study, a molecular structural dynamics model was employed and the simulation considered on the order of 6000 atoms. It was determined that the Young’s modulus, shear modulus, and Poisson ratio are all sensitive to the presence of vacancies. Furthermore, a linear relationship was established between the percentage of sites in the nanotube that contained a vacancy and the Young’s and shear moduli [39].

The inability of continuum models to accurately predict the properties of carbon nanotubes containing defects is not without precedent. It has been well established that relatively small, aperiodic perturbations in an otherwise periodic system can lead to vibration mode localization [40–42]. Vibration mode localization refers to the drastic spatial variation in system response of a near-periodic system, which is not present in the response of the fully periodic system. To illustrate this, consider a periodic system. Such a system is, by definition, made up of identical units. If the loading on each unit is identical and the initial conditions on each unit are identical, then the response of each unit will be identical. However, if the system is perturbed such that it is no longer periodic, the same loading and initial conditions can result in one or more units experiencing a response of much higher amplitude than the rest of the system [40,41]. Continuum models of carbon nanotubes make assumptions concerning the uniformity of the nanotube material [2] that do not allow for localization to be accounted for.

The results of numerical and experimental studies indicate that the presence of defects in a carbon nanotube have a profound impact on its mechanical properties, but the results themselves are not sufficient to form the basis of a model of a carbon nanotube containing defects for vibrational analysis. While the elasticity of a structure as a whole is very important in understanding its vibrational response, a deeper investigation of the local deviations from this overall elasticity is required to calculate the mode shapes of the structure. Furthermore, vacancies are not the only defects that may be present in a carbon nanotube. A method of analyzing carbon nanotubes with a variety of defects is therefore needed.

1.2.3 Carbon Nanotube Composites

As attractive as the properties of carbon nanotubes are, the scale on which carbon nanotubes exist limits their use as a structural material. Some of these limitations can be overcome by incorporating carbon nanotubes in composite materials. Though combining carbon nanotubes with weaker materials inevitably results in composites that are less strong

than individual carbon nanotubes, they still hold the potential to outperform more traditional materials [1, 43]. These composites have yet to reach their full potential, but substantial headway has been made in creating carbon nanotube impregnated resins [3, 43–45]. Research has also shown that the properties of carbon nanotubes can be harnessed by embedding them in metallic composites [11, 46–49]. In addition to increasing the stiffness and strength of the metals (although it should be mentioned that the change in those properties varied greatly between these studies), it has been shown that embedding carbon nanotubes in metals can lead to increased vibrational damping in the composites, and some cases an increased resistance to softening at high temperatures [11, 47].

Of the papers cited previously in relation to metal/CNT composites, of particular interest is the 1998 study by Kuzumaki *et al.* [46]. In it, two important details concerning aluminum reinforced with carbon nanotubes were observed. The first was that, unlike with carbon fibers, there was no carbide formation at the interface of the carbon nanotubes and the aluminum matrix. From a theoretical standpoint, this both emphasizes the stability of a the nanotubes' structure, and paves the way for a relatively simple model. Had there been carbide formation at the interface, that would have impacted the behavior of the composite — something that would have to be considered in any theoretical model. The second detail that was revealed was that, when the mechanical properties of the composite were compared to those of pure aluminum, the difference in strength was less than predicted using the Kelly-Tyson formula. This formula, however, does not account for interfacial slip between the matrix and the reinforcing fiber [50] — something that was later identified as the source of these composites' damping properties [51]. This interfacial slip appears to be key to understanding the dynamic behavior of carbon nanotubes. Naturally, these experimental findings have been followed by theoretical studies that attempt to explain these results [52–59].

While many of the existing studies concerning the vibration of composites containing carbon nanotubes produce good results, each has its shortcomings. Several of these stud-

ies [53–55, 58] rely on continuum models of carbon nanotubes. While this is common in nanotechnology literature, such models overlook the anisotropic nature of carbon nanotubes, and cannot accurately represent the stiffness of a nanotube in both tension and bending [2]. Furthermore, the comparisons to experimental results and molecular dynamics simulations show that there are elements of the behavior of carbon nanotubes, especially those with larger diameters, that defy simplification using continuum methods [60].

Those studies that take a more detailed view of carbon nanotubes, largely by modeling them at an atomic level, [52, 57, 59] are limited in the length of the carbon nanotubes under consideration, as the added complexity of these methods results in additional computational costs. The truncated length of the nanotubes result in a arguably skewed model of the interfacial friction between the nanotube and the matrix. All three of the studies listed used a stick-slip damper (also referred to as an elastic perfectly plastic model in materials science literature) to calculate the force of the nanotubes due to van der Waals interactions, after [59]. The difference in behavior of a small and large number of stick-slip damper in series is, in effect, the difference between a macroslip and a microslip damper (the latter being capable of partial slip) [61]. The dynamic behavior of microslip and macroslip dampers is different enough to raise concerns about the overall accuracy of these analyses [62]. Though quite different in their approaches and conclusions, all these studies mentioned here — using both continuum or atomistic methods — succeed in highlighting a very real interest on the part of the scientific community in understanding energy dissipation in nanocomposites, and the need for techniques that allow the complexities of these structures to be handled accurately, but with moderate computational effort.

1.2.4 System Order Reduction

Reducing the order of a system, that is to say reducing the number of equations that must be solved, is a process with obvious ramifications for complex systems such as those found in molecular dynamics simulations. This process can be approached from either a physical or a

mathematical standpoint. From the physical side, it is sometimes possible to observe that a given system can be broken down into sub-systems, identical in construction and behavior. These periodic units allow a quasi-infinite system, such as a crystal lattice, to be modeled by a modest number of atoms in a volume with periodic boundary conditions [4, 63]. In many ways this is an ideal order reduction method for vibrational analysis, as the vibrational frequencies and modes of the periodic unit can be calculated more easily than those for the full system, yet the Floquet-Bloch theorem allows the modes and frequencies of the full system to be extrapolated from those of the unit cell without significant computational effort and without loss of accuracy [4, 64, 65].

Though periodic systems are ideal for order reduction, many systems cannot be modeled that way. Some, though, are close to being periodic; they can be thought of as periodic systems that have been perturbed. This is similar to a situation that occurs on the macroscale when the parameters of a periodic system (such as a bladed rotor) are subject to small, random changes — referred to in turbomachinery literature as ‘mistuning’ [66, 67]. Though the methods used to address mistuning were developed for use in a finite elements framework, they can be expanded to handle certain atomic scale systems. The behavior of an atomic system predicted using an empirical force field with the assumption that displacements are small (a necessary assumption for a linear vibrational analysis [68]) can be summarized in terms of mass and stiffness matrices. These matrices are not fundamentally different than the mass and stiffness matrices of a finite element system, and so an order reduction algorithm that can be applied to a finite element system can be applied to that linearized atomic system.

A method of efficiently computing the vibrational response of this type of mistuned system was proposed by Yang and Griffin [69]. Their method, which involved projecting the system onto a reduced basis comprised of some of the modes of the nominal system¹, from which it derived the name SNM (subset of nominal modes). This technique is also referred

¹In the context of rotor dynamics, aperiodicities in the system represent flaws in the rotor due to manufacturing error. Therefore, the nominal system is the periodic system from which the real system deviates.

to as modal domain analysis (MDA) [66].

MDA succeeded in predicting the vibrational response of system in which the stiffness matrix was perturbed, however it failed when both the stiffness and mass matrices were perturbed. To correct this, an addition was made to this method by Sinha [66]. In this modified modal domain analysis method (MMDA), the reduced-order basis set comprised not only certain modes of the nominally tuned system, but also modes of what might be termed ‘periodically mistuned’ systems. The mass and stiffness matrices were mistuned, and were then subjected to proper orthogonal decomposition (POD). The largest valued POD features were each used in turn to uniformly perturb the tuned system (thus maintaining its periodicity). The modes of these systems were then used in the development of the reduced-order basis set.

1.3 Organization of this Dissertation

Following this introduction, further background information on the structure of pristine CNTs and on the mathematics that underly the analysis of their phonon dispersion (that is to say, their vibrational properties) is presented in Chapter 2. Then, in Chapter 3, microslip and macroslip dampers are described in detail, an analysis of the ability of a microslip damper to stabilize flutter is presented, and the energy dissipation of both types of dampers as a function of displacement is discussed. Chapters 4 and 5 are concerned with the development of reduced-order models of CNTs with defects. In Chapter 4, modal domain analysis and modified modal domain analysis are adapted for use with atomic systems. They are applied to CNTs with isotope and Stone-Wales defects, and the results are discussed. A new method of order reduction, modal domain reduction, is developed in Chapter 5 and applied to CNTs with multi-vacancy defects. These models are combined with a reduced-order model of bulk aluminum to form a model of an Al/CNT composite in Chapter 6. This is used to simulate the behavior of an Al/CNT in which the CNTs contain defects, and to determine its response

to low frequency excitation. The results of this simulation allow the stiffness and damping of the composite to be estimated, and for the damping properties to be classified in terms of the dampers discussed in Chapter 3.

Chapter 2

Background on Crystal Lattices and Carbon Nanotubes

2.1 Introduction

There is a considerable body of research stretching back to the early part of the 20th century concerning the behavior of individual atoms in infinite crystal lattices [64, 70]. The assumption that the crystal lattice is infinite has proved beneficial for analysis, as it allows the lattice to be represented accurately by a small unit cell with periodic boundary conditions [5]. Such lattices are frequently referred to as periodic lattices, a convention that is adhered to in this dissertation. Periodic lattices are not merely studied out of convenience; they can provide accurate insights into the behavior of bulk solids, provided that the structure of the solid is largely free from defects [4].

Among the many properties that can be ascertained using relatively small unit cells with periodic boundary conditions are the normal modes and modal frequencies of the system. In atomic lattices, those vibrational properties are more commonly described in terms of phonons. Phonons are quantized packets of vibrational energy, so to study the vibrational behavior of a crystal is to study the behavior of phonons in that crystal [71]. Phonons are characterized by their frequency and by their wavevector, a quantity that indicates both the

direction of wave propagation and the spatial periodicity of the wave. Though the notion of phonon dispersion is more common in the physics literature, in keeping with the conventions of engineering vibrational analysis normal modes and modal frequency are used more often in this work. It can be easily seen that a wavevector and a normal mode contain the same information — they both describe the shape made by a collection of atoms as they vibrate. The frequency of a phonon and the frequency of the corresponding normal mode are, of course, the same. In one situation, though, the wavevector cannot be avoided. The Floquet-Bloch theorem is defined in terms of wavevectors [4, 64], rendering the use of normal modes inconvenient. In that context only is the wavevector used here.

For the purposes of computational efficiency, it is highly advantageous to model a repeating atomic structure as a periodic lattice whenever possible. However, this is not always feasible. There are a number of defects that can occur in a crystal lattice that break the periodicity of the structure in a way that significantly alters the properties of the crystal [72]. Such defects include doping, vacancies, and various topological and structural defects that occur due to the arrangement and bond character of the carbon atoms [33–35]. In general, these defects are aperiodic — that is to say that they prevent the nanotube from being represented by a small unit cell. What is required to analyze these is a technique for reducing the computational effort needed to simulate the vibration of a large system with aperiodic flaws, without compromising the accuracy of the results.

2.2 The Structure of a Carbon Nanotube

A single walled carbon nanotube is nothing more than a strip of graphene rolled into a cylinder. Therefore, to understand the structure of a carbon nanotube, first the structure of graphene must be understood. Graphene is a lattice of sp^2 bonded carbon atoms — meaning that each carbon atom is bonded to three others. The angle between the bonds is equal, resulting in an hexagonal lattice. [18]. To form a carbon nanotube, a section of graphene is

rolled in such a way that the arrangement of atoms at the edges to be joined is identical. The resulting tube has an unbroken lattice structure.

Two pieces of information are needed to describe a atomic lattice: the position of the atoms in a ‘unit cell’, and the set of lattice vectors. Such a lattice is composed of copies of the unit cell — an arbitrary but finite volume that contains at least one atom — each translated to a position relative to the origin described by a linear combination of the lattice vectors. In other words, if the lattice vectors are $\mathbf{a}_1, \dots, \mathbf{a}_n$ and the position of the atoms in the unit cell are $\mathbf{p}_1, \dots, \mathbf{p}_m$, then the positions of all the atoms in the lattice are described by the set $P = \left\{ \sum_{i=1}^m \sum_{j=1}^n (\alpha_j \mathbf{a}_j + \mathbf{p}_i) \mid \alpha_j \in \mathbb{Z} \right\}$ [4].

To describe a hexagonal lattice such as graphene, the unit cell must contain two atoms. In a hexagonal lattice, any two bonded atoms are reflections of each other. A reflection cannot be described in terms of a translation, so the unit cell must contain two atoms that are mirror images of each other — atoms A and B in Fig. 2.1 [5].

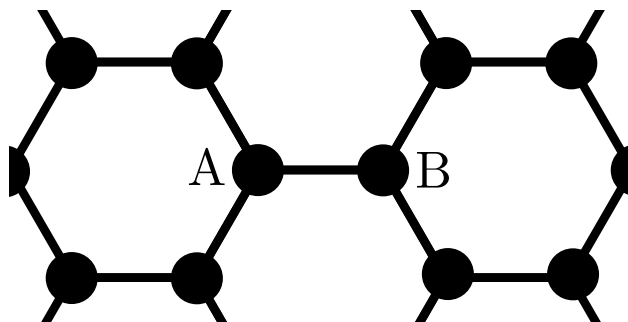


Figure 2.1: Atoms A and B are mirror images of each other. An atom each of type A and B must be included in a unit cell for graphene.

It is implicit from the mathematical definition of an atomic lattice that the lattice extends to infinity in all directions. While this is clearly not the case for any actual arrangement of atoms, it is a useful approximation when the vibration of atoms far from the edges is under consideration. The periodicity of the structure allows for the vibrational properties of the entire lattice to be calculated from the properties of a single unit cell. For graphene, this means that only two atoms are needed for such a model (see Fig. 2.2). When a carbon nanotube is modeled, the procedure is slightly different.

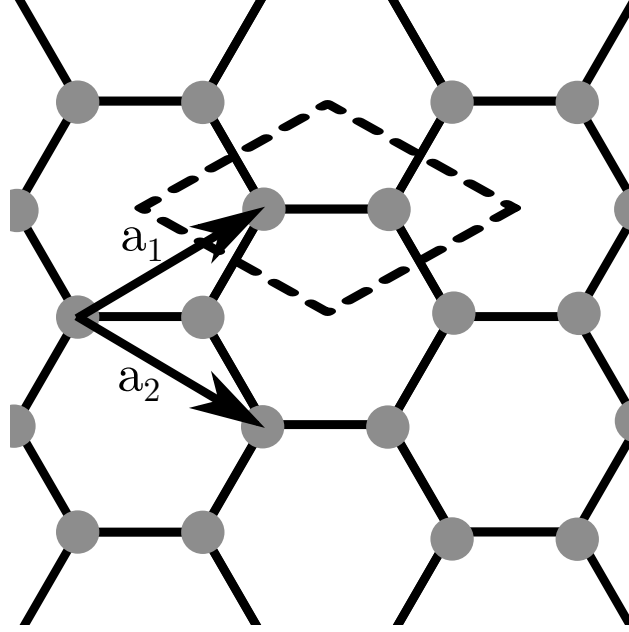


Figure 2.2: The hexagonal lattice of graphene, with the carbon atoms represented as gray dots. The dotted lines indicate the boundaries of a representative unit cell.

As was previously mentioned, a carbon nanotube can be thought of as a rolled up strip of graphene. The graphene must be ‘cut’ in such a way that when its edges are joined to form a cylinder, the lattice structure of the carbon atoms is not disturbed. This condition can be summarized in the following way: a graphene strip can form a carbon nanotube if and only if a line drawn from one side of the strip to the other, perpendicular to the edge, can be written as $\alpha\mathbf{a}_1 + \beta\mathbf{a}_2$, $\alpha, \beta \in \mathbb{Z}$. This line is the chiral vector of the nanotube. In conjunction with the chiral vector there is another vector, defined in a similar way, that runs parallel to the edges of the graphene strip and that can be written in terms of integer multiples of the lattice vectors (with the added stipulation that those integers must be relatively prime). This is the translation vector, and it indicates the shortest distance an atom can be translated perpendicular to the edge of the strip, such that it is coincident with an identical atom (see Fig. 2.3) The rectangle described by the chiral and translation vectors will be used as the unit cell for the carbon nanotube.

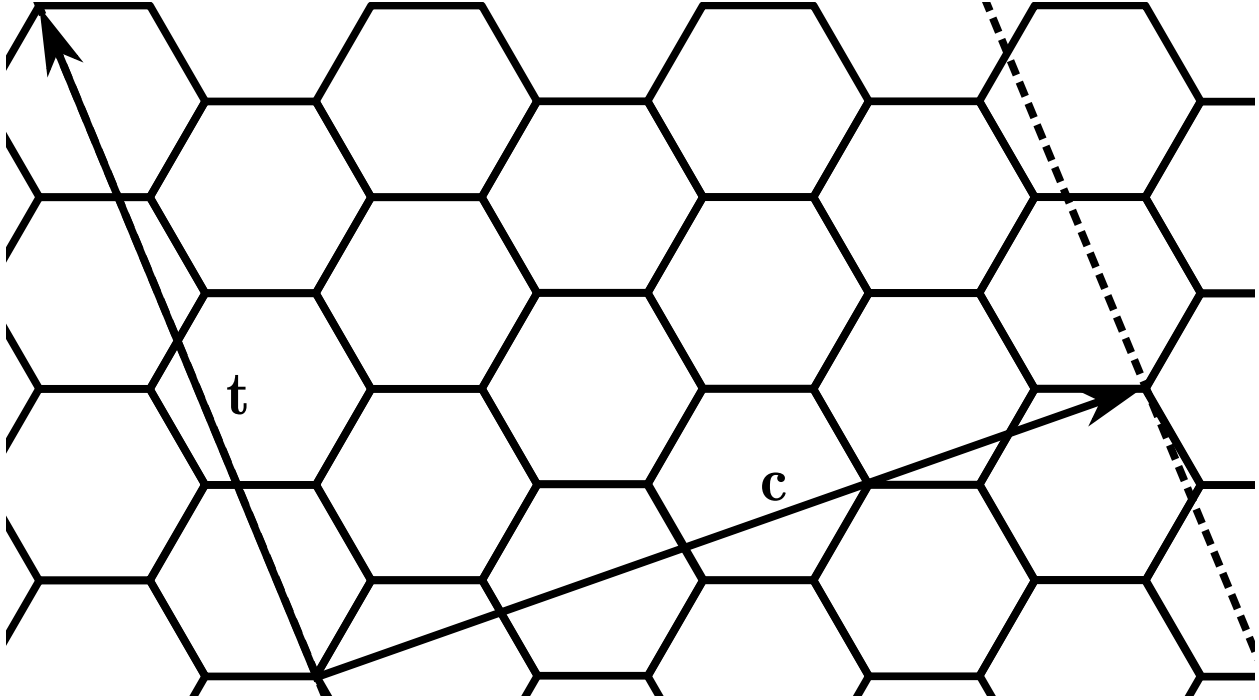


Figure 2.3: A strip of graphene that could be rolled into a carbon nanotube. The dotted lines represent the cuts in the graphene sheet that form the strip. \mathbf{c} is the chiral vector and \mathbf{t} is the translation vector.

2.3 Derivation of the Eigenvector Problem for an Atomic Lattice from the Interaction Tensor Representation

A common approach to calculating the forces on an atom in a lattice uses a constant interaction tensor. The prevalence of this model in prior studies of crystal lattices dictate that an examination of it is required. Before this examination is undertaken, it should be emphasized that the derivation presented here, which uses the interaction tensor to produce an eigenvalue problem, (the solution to which provides the frequencies and modes of the system) is by no means an original concept — similar derivations can be found in a number of sources, including Cleland and Jorio *et al.* [4, 5]. However, neither source provides a complete and detailed derivation for a system in which the unit cell contains two atoms.

Rather than looking at the ‘stiffness’ of the bonds connecting atoms, this section will use the more concise interaction tensor (after [4]) of two adjacent atoms. Although the bonds are not explicitly modeled as springs, this model is still equivalent to a harmonic force field. The interaction tensor, $\Phi^{(i,j)}$ is defined as the curvature of the interaction energy between atoms i and j , i.e.:

$$\Phi_{\alpha\beta}^{(i,j)} = \frac{\partial^2 U}{\partial r_{i,\alpha} \partial r_{j,\beta}} \quad (\text{where } r_{i,\alpha} \text{ is the } \alpha \text{ component of the position of atom } i) \quad (2.3.1)$$

Note that $\Phi_{\alpha\beta}^{(i,j)}$ corresponds to $\Phi_{\alpha\beta}(\mathbf{R}_i, \mathbf{R}_j)$ in the notation used by Cleland, and the element in the α^{th} row and the β^{th} column of $-K^{(i,j)}$, in the notation used by Jorio *et al.* The position vector used here is \mathbf{r} , rather than \mathbf{y} , in keeping with Cleland. Similarly, \mathbf{u} is the displacement vector, rather than \mathbf{x} .

Consider an atom located at real lattice point \mathbf{R}_j . Furthermore, consider a continuous lattice displacement $\mathbf{u}(\mathbf{r}, t)$, where \mathbf{r} is a point in space; this is not restricted to lattice points. At time t , the position of an atom originally located at \mathbf{R}_j is now $\mathbf{r}_j(t) = \mathbf{R}_j + \mathbf{u}(\mathbf{r}_j(t), t)$. It is important to note that the displacement is evaluated at the instantaneous position of the atom, not the original position. For small displacements, the instantaneous position can be approximated by the original positions, resulting in the relationship: $\mathbf{r}_j(t) = \mathbf{R}_j + \mathbf{u}(\mathbf{R}_j, t)$. For brevity, $\mathbf{u}_j(t) := \mathbf{u}(\mathbf{R}_j, t)$. Therefore $\mathbf{r}_j(t) = \mathbf{R}_j + \mathbf{u}_j(t)$. The equations of motion can then be derived. It should be observed that Φ is a tensor, and in keeping with Cleland’s notation, the dot (inner product) of two vectors and a tensor in this context is taken to mean the double sum (i.e. $\mathbf{v}_1 \cdot \mathbf{T} \cdot \mathbf{v}_2 = \mathbf{v}_2^T [\mathbf{T}] \mathbf{v}_1$, where $[\mathbf{T}]$ is the matrix representation of the tensor \mathbf{T} , and the vectors $\mathbf{v}_1, \mathbf{v}_2$ are taken to be column vectors).

The kinetic energy of the system is

$$T = \frac{1}{2} m \sum_{j=1}^N \left| \frac{\partial \mathbf{r}_j}{\partial t} \right|^2 = \frac{1}{2} m \sum_{j=1}^N \left| \frac{\partial \mathbf{u}_j}{\partial t} \right|^2 \quad (2.3.2)$$

where m is the mass of each atom in the unit cell (it is assumed here that all the atoms in

the system have the same mass). The potential energy is

$$U = \frac{1}{2} \sum_{jk} \mathbf{u}_j \cdot \Phi^{(j,k)} \cdot \mathbf{u}_k \quad (2.3.3)$$

The full derivation of equation 2.3.3 can be found in [4], §2.6. The Hamiltonian of the system is then:

$$H = \frac{1}{2} \sum_{j=1}^N m \left| \frac{\partial \mathbf{u}_j}{\partial t} \right|^2 + \frac{1}{2} \sum_{jk} \mathbf{u}_j \cdot \Phi^{(j,k)} \cdot \mathbf{u}_k \quad (2.3.4)$$

Taking the generalized position q_i to be u_a , where $a = [i/3] - (i \bmod 3)$, the generalized momentum p_i is \dot{q}_i/M , and the Hamiltonian can then be written:

$$H = \frac{1}{2} \sum_{j=1}^{3N} \left[\frac{p_j^2}{m} + \sum_{k=1}^{3N} q_j \Phi^{jk} q_k \right] \quad (2.3.5)$$

The equations of motion for the system can then be found using Hamilton's equations:

$$\frac{dq_i}{dt} = \frac{\partial H}{\partial p_i} = \frac{p_j}{m} \quad (2.3.6)$$

$$\frac{dp_i}{dt} = -\frac{\partial H}{\partial q_i} = -\sum_{k=1}^{3N} \Phi^{jk} q_k \quad (2.3.7)$$

Combining these and converting back into terms of \mathbf{u} :

$$m \frac{d^2 \mathbf{u}_{j\alpha}}{dt^2} = -\sum_{k=1}^N \sum_{\alpha=1}^3 \Phi_{\alpha\beta}^{(j,k)} \mathbf{u}_{k\beta} \quad (2.3.8)$$

Until this point, the main difference between this derivation and that presented by Cleland had been in nomenclature. However, it is now necessary to diverge further, as Cleland's method does not allow for a unit cell to contain more than one atom. Let us consider a unit cell that contains two atoms, originally at lattice points \mathbf{R}_i and \mathbf{R}_{i+1} . The positions of the atoms can be condensed into a single vector with six components $\mathbf{r}_{[a]} = [\mathbf{r}_{i1}, \mathbf{r}_{i2}, \mathbf{r}_{i3}, \mathbf{r}_{(i+1)1}, \mathbf{r}_{(i+1)2}, \mathbf{r}_{(i+1)3}]^T$ (a subscript in brackets indicates a quantity relat-

ing to a unit cell). $\mathbf{r}_{[a]}$ can clearly be broken down into $\mathbf{R}_{[a]} + \mathbf{u}_{[a]}$, and so equation 2.3.8 can be rewritten as:

$$m \frac{d^2 \mathbf{u}_{[a]}}{dt^2} = - \sum_{b=1}^{N/2} \Phi^{[a,b]} \mathbf{u}_{[b]} \quad (2.3.9)$$

where:

$$\Phi^{[a,b]} = \begin{bmatrix} \Phi^{(j,k)} & \Phi^{(j,k+1)} \\ \Phi^{(j+1,k)} & \Phi^{(j+1,k+1)} \end{bmatrix} \quad (2.3.10)$$

Now, a general form of $\mathbf{u}_{[a]}$ can be inserted into equation 2.3.9. The general solution to this equation is of the form $\mathbf{u}_{[a]} = \mathbf{A}_{[a]}(\mathbf{r}_{[a]})e^{i\omega t}$. In addition to this, Bloch's theorem states that $\mathbf{A}_{[a]}(\mathbf{r}_{[a]}) = \mathbf{A}e^{i\mathbf{k}\cdot\mathbf{R}_{[a]}}$, where \mathbf{k} is the wave vector for that particular mode. Subsequently, $\mathbf{u}_{[a]} = \mathbf{A}e^{i\mathbf{k}\cdot\mathbf{R}_{[a]}}e^{i\omega t}$. Substituting this into equation 2.3.9 gives:

$$m\omega^2 \mathbf{A}e^{i\mathbf{k}\cdot\mathbf{R}_{[a]}}e^{i\omega t} = \sum_{b=1}^{N/2} \Phi^{[a,b]} \mathbf{A}e^{i\mathbf{k}\cdot\mathbf{R}_{[b]}}e^{i\omega t} \quad (2.3.11)$$

After a little algebra:

$$m\omega^2 \mathbf{A} = \sum_{b=1}^{N/2} \Phi^{[a,b]} \mathbf{A}e^{i\mathbf{k}\cdot(\mathbf{R}_{[b]} - \mathbf{R}_{[a]})} \quad (2.3.12)$$

It is clear that only the relative positions of the atoms are relevant, so a coordinate system is chosen such that $\mathbf{R}_{[a]} = \mathbf{0}$. This reduces the above equation to:

$$m\omega^2 \mathbf{A} = \sum_{b=1}^{N/2} \Phi^{[a,b]} \mathbf{A}e^{i\mathbf{k}\cdot\mathbf{R}_{[b]}} \quad (2.3.13)$$

From this, the dynamical matrix can be defined:

$$\mathbf{D} = \sum_{b=1}^{N/2} \Phi^{[a,b]} e^{i\mathbf{k}\cdot\mathbf{R}_{[b]}} \quad (2.3.14)$$

therefore:

$$m\omega^2 \mathbf{A} = \mathbf{D}\mathbf{A} \rightarrow (\mathbf{D} - m\omega^2 \mathbf{I}) \mathbf{A} = 0 \quad (2.3.15)$$

While this is sufficient to continue, it is instructive to note that \mathbf{D} is the Fourier transform of

Φ , a fact which underlines the nature of Bloch's theorem: it is not imposed on the problem, it is rather a natural feature due to the periodicity of the system.

Just as $\Phi^{[a,b]}$ can be broken down into four sub-matrices, \mathbf{D} can be broken into four sub-matrices:

$$\mathbf{D} = \begin{bmatrix} D_{11} & D_{12} \\ D_{21} & D_{22} \end{bmatrix} = \sum_{b=1}^{N/2} \begin{bmatrix} \Phi^{(j,k)} & \Phi^{(j,k+1)} \\ \Phi^{(j+1,k)} & \Phi^{(j+1,k+1)} \end{bmatrix} e^{i\mathbf{k}\cdot\mathbf{R}_{[b]}} \quad (2.3.16)$$

Note that atoms j and k are the first atoms in their respective unit cells (the A atoms, in Jorio's notation — see figure 2.1). Therefore atoms $j + 1$ and $k + 1$ are the second atoms (the B atoms). It follows, then, that $\sum_k \Phi^{[j,k]}$ is the sum of all interaction tensors between atom j and every other A atom in the lattice, and so D_{11} dynamical matrix of the A atom in a unit cell with respect to all other A atoms. Similarly, D_{22} is the dynamical matrix of the B atom with respect to all other B atoms. D_{12} and D_{21} are the dynamical matrices of the A atom with respect to all B atoms and the B atom with respect to all A atoms, respectively.

So far, this derivation has assumed that all atoms influence the movement of all other atoms. While this is not necessarily an incorrect assumption, it makes assembling the dynamical matrices computationally very expensive. Instead, only the influence of four nearest 'layers' of neighbors are considered. However, before the interaction tensors between atoms is calculated, a further approximation should be explained. If the radius of a nanotube is sufficiently large, atoms interact with their close neighbors as if they were coplanar (that is to say that the variation in position in the radial direction is insignificant in comparison to the interatomic spacing). Therefore the relative radial positions of neighbors in equilibrium can be ignored, and the nanotube can be treated as a flat plane of atoms with periodic boundary conditions on two opposite sides [5].

With these assumptions and approximations in place, the interaction tensors for two atoms, j and k , which are n^{th} neighbors with respect to each other can be calculated as

follows:

$$\Phi^{(jk)} = U^{-1}(\theta)\Phi_n U(\theta)$$

where

$$U(\theta) = \begin{bmatrix} \cos \theta & \sin \theta & 0 \\ -\sin \theta & \cos \theta & 0 \\ 0 & 0 & 1 \end{bmatrix}$$

$$\Phi_n = \begin{bmatrix} \phi_{n1} & 0 & 0 \\ 0 & \phi_{n2} & 0 \\ 0 & 0 & \phi_{n3} \end{bmatrix}$$

and θ is the in-plane angle between i and j . Example components of Φ_n , calculated by Jorio *et al.* [5], are given in Table 2.1.

Table 2.1: Components of the interaction tensor of graphitic carbon in dynes/cm, from [5].

Neighbor:	1	2	3	4
ϕ_{n1}	36.50	8.80	3.00	-1.92
ϕ_{n2}	24.50	-3.23	-5.25	2.29
ϕ_{n2}	9.82	-0.40	0.15	-0.58

Chapter 3

Microslip Damping

3.1 Introduction

One of the most promising avenues for developing nanocomposite materials is the possibility of taking a material already quite well suited to a task, and enhancing specific properties of it through the addition of certain nanostructures [43, 73]. For example, rotor blades for turbomachinery applications require high strength to withstand the extreme loads placed on them, tolerance to extreme temperatures, and the ability to withstand self-exciting dynamic loads without yielding or fatiguing [13, 74, 75]. This third criterion arises from flutter, an aeroelasticity interaction between the rotor blade and the airflow around it which, if left unchecked, causes the rotor blade to oscillate with increasing amplitude [13, 75]. Modern superalloys are sufficient to satisfy the strength and temperature criteria, but like most high-strength materials, they exhibit very little material damping [76]. As a result, mechanical dampers are needed to ensure that blade oscillations remain within a safe range [12, 75, 77]. The need for such dampers could be removed, however, if the material from which rotor blades are constructed could have its material damping increased to the point that it was capable of stabilizing flutter. Recent work pertaining to carbon nanotubes embedded in metals suggest that these composites could achieve just such an increase in damping. [3, 11, 43, 46, 48].

It has long been known that fibers embedded in another material can provide damping,

due to slipping at the interface between the fibers and the material in which they are embedded (the matrix) [47]. Analysis has also shown that, in cases where the only loads on the fibers are imparted by the matrix, these fibers undergo partial slip — that is to say that a portion of the fiber’s length does not slip relative to the matrix, while the rest does [47,78]. A common approach in studies of interfacial slip, whether at the nanoscale or the macroscale, is to utilize a macroslip friction model, which does not consider partial slip [57, 58, 75, 79]. The macroslip model assumes that the damper acts as a linear spring until some maximum displacement is reached [12, 75]. Beyond this maximum displacement, the damper provides a constant force until the motion reverses its direction. Studies by Sinha and Griffin [12, 75] succeeded in showing that a rotor blade subjected to negative damping can be stabilized by a macroslip damper, using the method of describing functions (also known as the method of harmonic balance). However, it was also shown that this stabilization could only take place if the magnitude of the negative damping is less than some maximum value and the amplitude of the blades oscillations is less than some upper limit. All these results are reflection of the fact that work done by the negative damping is proportional to the square of amplitude, whereas the energy dissipated by the macroslip friction damper is proportional to the amplitude. Later, Ferri and Whiteman [80] also used the method of harmonic balance, and presented analytical results for the interaction between negative viscous damping and a displacement dependent macroslip friction model. They considered a rigid damper, and also found global stability under certain conditions.

Despite the successful analysis of macroslip dampers in rotors, this model is not sufficient for modeling a blade constructed from a fiber composite material, with high material damping. The nature of the loading on fibers requires that partial slip (when a portion of the damper moves but the rest stays fixed) occurs when there is a sufficient load applied to the fibers [81]. This is better approximated using a microslip model, which accommodates this partial slip situation [15, 82]. Recently, Martel et al. [83] have studied the stabilizing effects of microslip friction damping models developed by Oloffson [84] on the spring-mass

model of a rotor stage.

This chapter deals with a fundamental study of comparison between the stabilizing effects of microslip and macroslip friction damping models. The microslip friction model developed by Menq et al. [61,81] has been used. Unlike macroslip friction dampers, energy dissipated by a microslip friction damper is not proportional to amplitude. Therefore, the following issues have been addressed using the describing function method: i. Are the amplitudes of stable limit cycles lower for microslip? ii. How do the limits on the maximum amplitude of transient disturbances for a stable limit cycle compare? iii. Does microslip friction stabilize a higher value of negative damping? and iv. What is the relationship between energy dissipation per cycle by microslip and amplitude of vibration?

The organization of this chapter is as follows. First, the microslip model is described. Then, a non-dimensional single degree of freedom model incorporating a microslip friction damper is developed. Next, the describing function method is employed to determine the amplitudes of limit cycles. Lastly, numerical results for microslip models are presented along with comparisons to those from macroslip friction models.

3.2 Microslip Friction Model

The microslip friction model used in this investigation was developed by Menq et al. [61, 81]. The behavior of this damper can be likened to the behavior of an elastically deformable, massless block resting on a shear layer. The block has coefficient of elasticity E , cross sectional area α , and length L . The shear layer has stiffness per unit length k_s and maximum possible shear force per unit length τ_m , shown in Fig. 3.1. The behavior of a microslip damper relative to a macroslip damper is illustrated in Fig. 3.2.

While the forces applied to the block are small enough, the block and the shear layer both stretch at the same rate and no slipping takes place between them. In this no slip state,

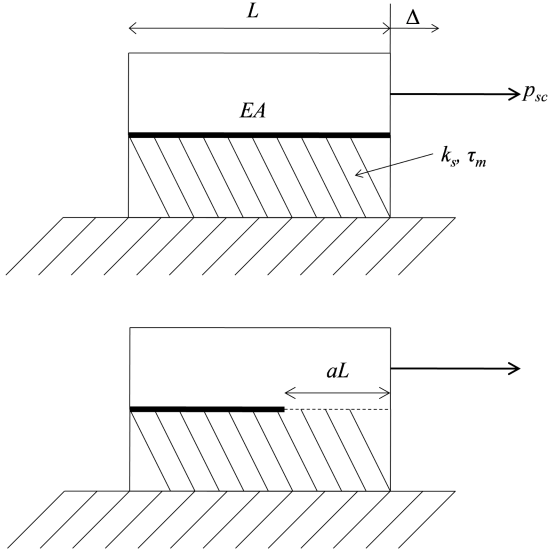


Figure 3.1: Schematic of microslip damper

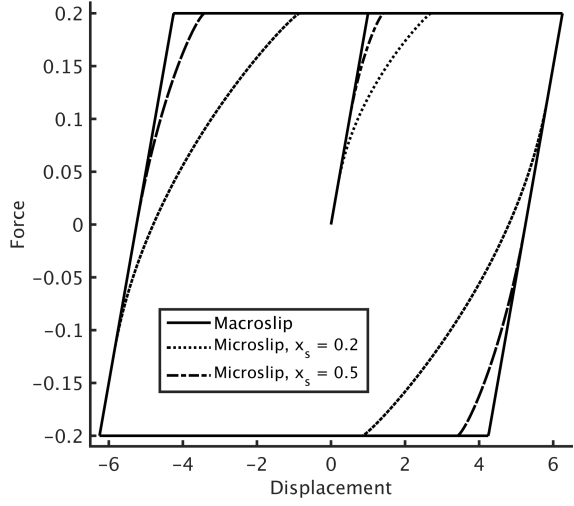


Figure 3.2: Hysteresis curves of microslip and macroslip damper systems

the damper force p_{sc} is proportional to total deflection Δ as follows:

$$p_{sc}(\Delta) = k_d \Delta \quad (3.2.1)$$

where:

$$k_d = k_s L \tanh(\lambda) / \lambda \quad (3.2.2)$$

$$\lambda = \sqrt{k_s L^2 / E \alpha} \quad (3.2.3)$$

When the force is relaxed, both the block and the shear layer return to their undeformed configurations – in other words the damper acts as a linear spring with stiffness k_d . If a sufficiently large force is applied, the block will deform enough that its leading edge will begin to slide on the shear layer. At this point the damper ceases to be fully elastic, and cannot return to its undeformed state without the addition of energy to the system. This will be referred to as the partial slip state. The damper begins to slip when Δ equals Δ_s , defined:

$$\Delta_s = \tau_m / k_s \quad (3.2.4)$$

Let a be the fraction of the length of the damper which is slipping (see Fig. 3.1). The deflection and damper force are expressed as functions of a :

$$\Delta a = (\tau_m/k_s) \{1 + \lambda^2 a [(a/2) + \tanh \lambda (1 - a)/\lambda]\} \quad (3.2.5)$$

$$p_{sc}(a) = (\tau_m L) [a + \tanh \lambda (1 - a)/\lambda] \quad (3.2.6)$$

If a larger force is applied to the block, sufficient that the boundary between the slipping and non-slipping regions reaches the trailing edge of the block, the damper is said to be in its full slip state. The damper leaves the partial slip state when Δ equals Δ_{fs} :

$$\Delta_{fs} = (\tau_s/k_s) + (\tau_m L^2/2E\alpha) \quad (3.2.7)$$

In the full slip state, the damper force is constant and independent of the displacement of the damper:

$$p_{sc} = p_{fs}^* = \tau_m L \quad (3.2.8)$$

The preceding equations provide a ‘skeleton curve’ (hence the subscript ‘sc’) for the behavior of the damper as it moves from rest. For subsequent unloadings and reloadings, the Massing rule [85] is applied to determine damper force p^* as a function of damper displacement Δ , which is a function of blade displacement x^* . When the direction of loading is reversed after slipping, the damper will follow the force/displacement curve described as follows:

$$p^*(x^*) = 2 [p_{sc}((x^* - x_0^*)/2)] + p_0 \quad (3.2.9)$$

where p_0 and x_0^* are the force and displacement respectively at which loading is reversed. Further, $\Delta = x^*$ for the initial loading, and $\Delta = (x^* - x_0^*)/2$ for subsequent loadings and unloadings after slipping.

3.3 Single Degree of Freedom Model, Nondimensionalization and Describing Function Analysis

It is assumed that, like a blade-friction damper system, the dynamics of a composite blade vibrating at a specific frequency can be accurately modeled by a single degree of freedom system, Fig. 3.3. This model for blade-damper systems has been derived by Griffin [77] and has been validated by experimental data. The blade is considered to be linearly elastic with modal stiffness k . Aerodynamic forces on the blade are represented by negative damping, c , acting on the blade. In the preceding formulation of the microslip damper model, the behavior of the damper is determined by parameters τ_m , $E\alpha$, L , and k_s (here $E\alpha$ is treated as a single parameter, as the two terms are not separated). The differential equation of motion for the single degree of freedom system is:

$$m \frac{d^2 x^*}{dt^{*2}} + c \frac{dx^*}{dt^*} + kx^* + p^*(x^*, \tau_m, E\alpha, L, k_s) = 0 \quad (3.3.1)$$

where damper force p^* is defined by eq. 3.2.9.

To achieve a greater generality in these results, the system will be nondimensionalized. This reduces the number of microslip friction parameters to two, specifically ϵ and x_s (Appendix A), where ϵ is the nondimensional stiffness and x_s is the nondimensional distance at which slipping starts. Furthermore, the following nondimensional quantities will be introduced:

$$\epsilon := k_s / (k + k_d) \quad (3.3.2a)$$

$$\zeta_+ := -c / \sqrt{4m(k + k_d)} \quad (3.3.2b)$$

$$x = x^* / x_0 \quad (3.3.2c)$$

$$t = t^* / T \quad (3.3.2d)$$

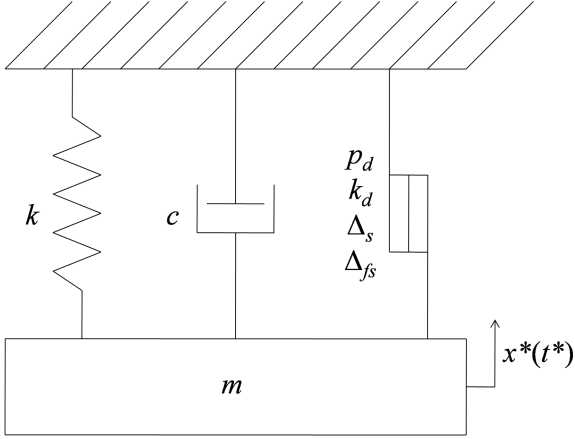


Figure 3.3: Dimensional single degree-of-freedom system

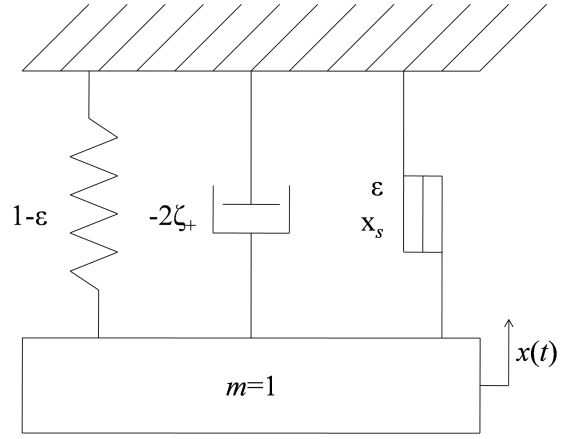


Figure 3.4: Nondimensional single degree-of-freedom system

$$\omega = \omega^* T \quad (3.3.2e)$$

$$x_0 : p_{fs}^*/k_d \quad (3.3.2f)$$

$$T = \sqrt{m/(k + k_d)} \quad (3.3.2g)$$

$$x_s := \Delta_s/x_0 \quad (3.3.2h)$$

Here ζ_+ , x , t , and ω are the nondimensional magnitude of negative damping ratio, displacement, time and frequency, respectively. The slip distance x_0 and inverse of the natural frequency of fully stuck system T are the characteristic length and time used in this nondimensionalization. The nondimensional system (Figure 5) can be described by the equation:

$$\frac{d^2 x}{dt^2} - 2\zeta_+ \frac{dx}{dt} + (1 - \epsilon)x + p(x, \epsilon, x_s) = 0 \quad (3.3.3)$$

Here $p(x, \epsilon, x_s)$ (defined in Appendix A) is the nondimensional force exerted by the damper. For the sake of brevity, the parameters on which it depends are often suppressed and written simply as $p(x)$.

Assuming that the steady-state response is harmonic:

$$x = A \sin \omega t \quad (3.3.4)$$

Substituting equation 3.3.4 into 3.3.3

$$-\omega^2 A \sin \omega t - 2\zeta_+ \omega A \cos \omega t + A(1 - \epsilon) \sin \omega t + p(x) = 0 \quad (3.3.5)$$

Because the displacement is assumed to be harmonic, the nonlinear damper force, $p(x)$, will be periodic and may be described by a Fourier series expansion. Using only the fundamental frequency terms of this series

$$p(x) = g \cos \omega t + h \sin \omega t \quad (3.3.6)$$

The coefficients g and h are found by performing the following integrations numerically:

$$g = \int_0^\pi p(A \sin \theta) \cos \theta d\theta \quad (3.3.7)$$

$$h = \int_0^\pi p(A \sin \theta) \sin \theta d\theta \quad (3.3.8)$$

Substituting eq. 3.3.6 into eq. 3.3.5 and equating the coefficients of $\sin(\omega t)$ and $\cos(\omega t)$ on both sides, the following two algebraic equations are obtained:

$$-\omega^2 A + A(1 - \epsilon) + h = 0 \quad (3.3.9)$$

$$-2\zeta_+ \omega A + g = 0 \quad (3.3.10)$$

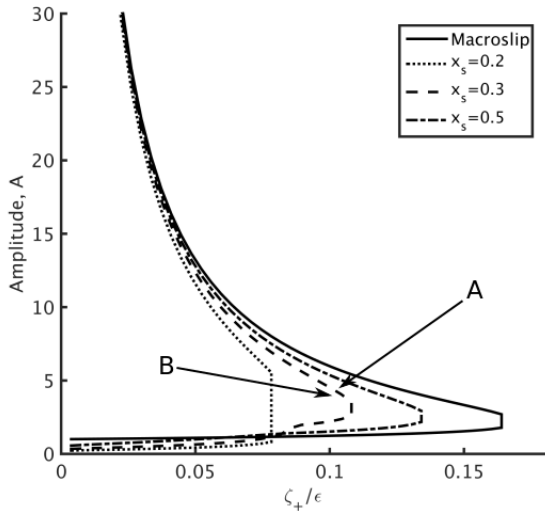


Figure 3.5: Amplitudes of limit cycles

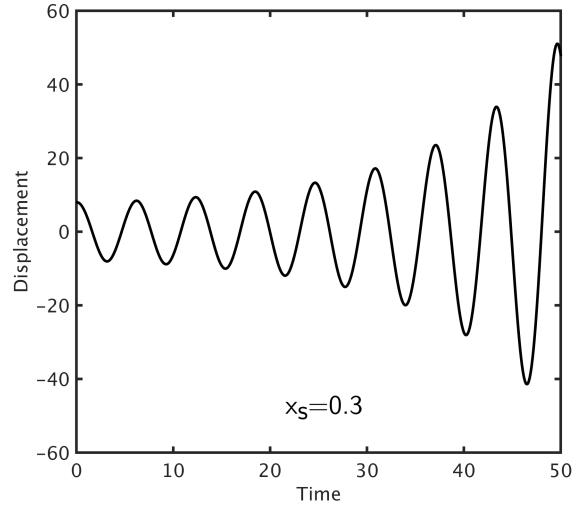


Figure 3.6: Simulated response for initial conditions corresponding to point A in Fig. 3.5

Recombining eqs. 3.3.9 and 3.3.10 and solving for A produces:

$$A = \left[-h \pm \sqrt{h^2 + (1 - \epsilon) g^2 / \zeta_+^2} \right] / 2(1 - \epsilon) \quad (3.3.11)$$

3.4 Numerical Results and Discussion

In general, eq. 3.3.11 produces two solutions, A_L and A_U , such that $A_L < A_U$ (Fig. 3.5). As with the macroslip damper, the lower amplitude A_L is that of a stable limit cycle, while the upper amplitude A_U marks the maximum amplitude of transient disturbances below which the system is stable [75]. The behaviors of the system when given unstable and stable initial conditions are shown in Fig. 3.6 and 3.7, respectively. The phase portraits of the responses are shown in Fig. 3.8. For any damper parameters (ϵ and x_s) there is a value of ζ_+ such that the limit cycle and the boundary of stability become coincident. For values of ζ_+ greater than this, the system is globally unstable.

The behavior of the microslip damper model can be described through a comparison to that of the macroslip damper model in an otherwise identical system. Using the nondimen-

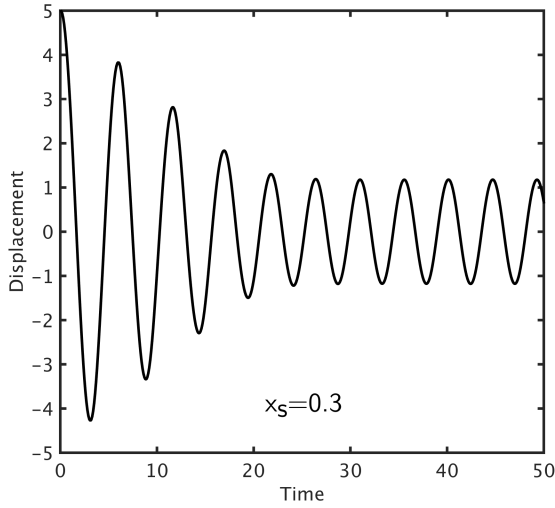


Figure 3.7: Simulated response for initial conditions corresponding to point B in Fig. 3.5

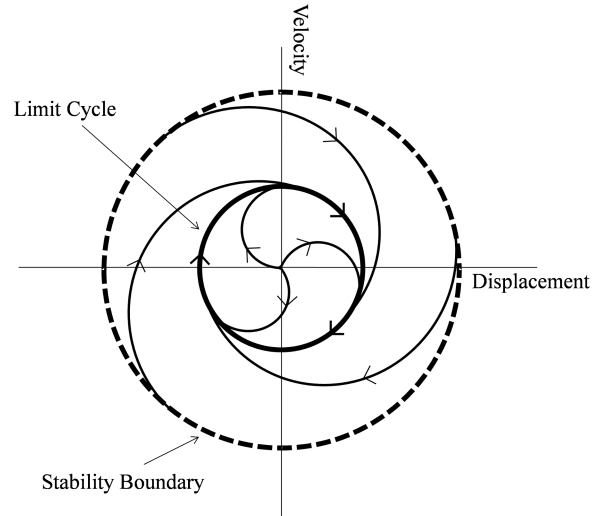


Figure 3.8: Phase portrait of response with microslip damper

sionalized macroslip damper model [75], microslip damper which provides force $p_m(x, \epsilon, x_s)$ can be matched to macroslip damper which provides force $p_M(x, \epsilon)$. The behaviors of both dampers before partial slipping starts and after full slipping starts are identical. The only difference between the two dampers occurs when the microslip damper is in the partial slip region of its behavior.

While the microslip damper is partially slipping, it behaves, in part, inelastically. Subsequently, energy is removed from the system and damping takes place. If the nondimensional displacement is less than one, the macroslip damper will not slip, and so will act elastically and contribute no damping. Therefore, for $A < 1$, the microslip damper provides greater damping than the macroslip damper, Fig. 3.9. Also, there is an amplitude A_t below which the microslip damper dissipates a greater amount of energy. That is why the amplitude of the microslip damper's stable limit cycle is lower for small amount of negative damping, Fig. 3.5.

For $A > A_t$, the energy dissipated by a macroslip damper is higher (Appendix B), and therefore the amplitude of the stable limit cycle is lower for the microslip damper. Also, it is seen that the amplitude at which the system becomes unstable is always lower for microslip

dampers, which suggests that, at full slip, a macroslip damper provides more damping than a comparable microslip damper.

Because at large amplitudes the macroslip damper provides more damping, the maximum amount of negative damping that can be stabilized by a macroslip damper is always larger than the maximum amount damped by a comparable microslip damper. The system has a limit cycle when the energy added by flutter is equal to the energy dissipated by the damper. Therefore, as the macroslip damper dissipates more energy, the amount of flutter that it can stabilize must be larger. This is verified by the amplitude plot in Fig. 3.5. A limit cycle is stable [86] when

$$\frac{\partial EG}{\partial A} < 0 \quad (3.4.1)$$

where EG is the difference between work done per cycle by negative damping and energy dissipated per cycle by friction dampers.

As can be observed from Fig. 3.9, the energy dissipated by two microslip dampers with different values of slip distance x_s can, at a specific amplitude, be equal. This effect does not occur with macroslip dampers, and can be explained as follows: Consider two dampers with equal values of ϵ , but one (damper A) with x_s equal to x_{sA} and the other (damper B) with x_s equal to x_{sB} , such that $x_{sA} < x_{sB}$. For $x_{sA} < A < x_{sB}$, it is clear that damper A slips and damper B does not. Therefore the damping provided by damper A is larger. However, when both dampers are slipping fully, damper B will dissipate more energy (Appendix B). Subsequently, as the amount of damping provided is a continuous function of amplitude, there must be an amplitude at which both dampers provide the same amount of damping.

3.5 Conclusion

The preceding results show that a composite rotor blade (modeled as a microslip damper) is capable of stabilizing negative damping. Furthermore, for small values of negative damping, this microslip damping causes the system to enter a stable limit cycle with a lower

amplitude than a macroslip damper (friction damper with macroslip) with comparable parameters would. However, it is shown that the amount of flutter (the magnitude of the negative viscous damping coefficient) and the maximum amplitude of a transient disturbance that can be stabilized by macroslip damping are always lower than those which can be stabilized by a macroslip damper with comparable parameters. Also, it has been found that macroslip damping with different values of slip distance can dissipate same amount of energy per cycle for the same amplitude of vibration.

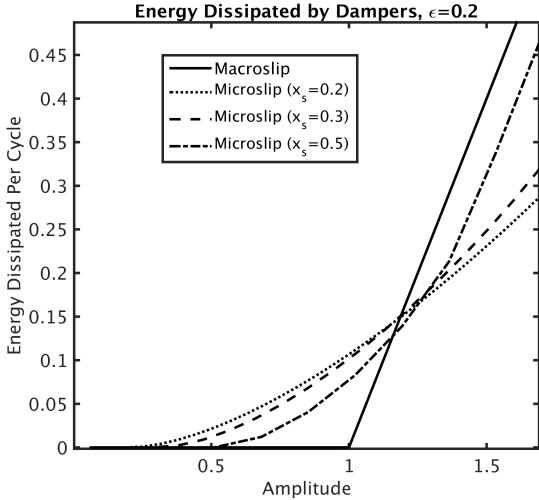


Figure 3.9: Comparison of energy dissipated by macroslip and microslip dampers

Chapter 4

Reduced-Order Models of Carbon

Nanotubes: Isotope and Stone-Wales Defects

4.1 Introduction

If the properties of carbon nanotubes are to be fully understood and possibly modified for specific purposes, it is vital that the impact of defects on these properties is fully understood. Defects in carbon nanotubes (CNTs) are both inevitable and mathematically problematic. Not only have point defects been observed in situ by Fan et al. [36], but the presence of isotope defects—specifically a mixture of ^{12}C and ^{13}C —can be inferred by the ubiquitous presence of both isotopes [4]. Furthermore, any crystal lattice that is of finite size must at some point be terminated, and this termination is itself a defect [87]. These defects are a significant impediment to the analysis of CNTs, as they rob the nanotubes of their periodicity.

Like its planar analogue, graphene, a pristine CNT (one which is without defects) can be thought of as an unending sequence of identical, repeating units [88]. This allows the free vibration characteristics of the nanotube to be calculated by considering the behavior of only one of these units and invoking the Floquet–Bloch theorem [4, 89]. Breaking the nanotube’s periodicity by introducing a defect renders this approach invalid, and results in

greatly increased computational expense.

The presence of defects in an otherwise periodic structure has significant consequences for its vibrational properties. It has been shown that disorder in an atomic system leads to fundamental changes in the nature of wave propagation in that system, a result that has a commensurately large impact on the vibrational modes—that is to say, the phonon dispersion—of the system [90]. Furthermore, the phonon dispersion of a CNT has profound implications for its mechanical and transport properties [5]. Understanding and, perhaps, harnessing the emergent properties due to these defects require accurate and efficient methods for determining the vibrational characteristics of almost-periodic atomic systems. In this chapter, two such methods are considered, and each is applied to two dissimilar types of defect.

Of the many defects that can affect CNTs, those under consideration in this chapter are isotope defects and Stone–Wales defects (SWDs) in single-walled CNTs. As previously mentioned, isotope defects are simply the presence of multiple isotopes of carbon distributed randomly throughout the structure [4]. This has the effect of perturbing the mass matrix of the system, but it does not influence interatomic interactions or the stiffness matrix. An SWD, which will be described in more detail later, is the rearrangement of certain bonds in the nanotube. While a pristine nanotube consists exclusively of hexagonal rings of carbon, an SWD is the presence of adjacent pentagonal and heptagonal rings [91]. This alters the manner in which the carbon atoms interact without changing their masses. In other words, the stiffness matrix changes, but the mass matrix remains unchanged.

Prior attempts have been made, notably by Chen et al. [92] and Georgantzinis et al. [93], to account for the impact of defects on the vibration of CNTs using numerical methods. These studies report changes in the natural frequencies of CNTs due to the presence of defects but do not consider changes in the corresponding mode shapes. Both of these investigations rely on the molecular structural mechanics model developed by Li and Chou [30]. They require a full-order model of the perturbed CNT—restricting their use to relatively short

CNTs. Furthermore, the molecular structural mechanics model does not permit for the relaxation of an atomic structure after a defect is created and for the subsequent alterations to the interatomic stiffnesses.

Periodic systems with inevitable defects are not unique to the atomic scale. Rotor blades, the circular arrangement of which causes them to be periodic, have proved to be a fertile area of investigation not only for the behavior of such systems with defects but also for the development of order reduction methods to handle the increase in complexity that these defects bring [14, 66, 94]. Two such methods, modal domain analysis (MDA) and modified modal domain analysis (MMDA), are here applied to CNTs with isotope defects and SWDs.

4.2 Methods

While the equations of motion that govern the behavior of a system of atoms are far from being simple [4, 95], this study pertains only to the vibrational properties of such a system. Specifically, the properties of interest are the vibrational modes and natural frequencies of CNTs. The concepts of vibrational modes and frequencies are defined in a rigorous sense only for linear systems, that is to say, systems in which interactive force is proportional to displacement [68]. The equations of motion that will be used here are derived by first finding a static equilibrium for the system in question — effectively reducing its temperature to 0 °K — and assuming that during vibration atoms are only displaced a small distance from this equilibrium. This ‘frozen phonon’ approach [96] allows the system to be linearized, and so permits the equations of motion for free vibration to be written as

$$\mathbf{M}\ddot{\mathbf{x}}(t) + \mathbf{C}\dot{\mathbf{x}}(t) + \mathbf{K}\mathbf{x}(t) = \mathbf{0} \quad (4.2.1)$$

where $\mathbf{x}(t)$ contains the positions of the atoms in the system and \mathbf{M} , \mathbf{C} and \mathbf{K} are the constant mass, damping and stiffness matrices, respectively. Vibrational modes and frequencies are properties of the undamped system; therefore, the damping matrix \mathbf{C} can be set to

zero [68]. Note that, for the remainder of this chapter, the time dependence of \mathbf{x} will be implied.

While the stiffness matrix in eq. 4.2.1 could be found using *ab initio* methods [97], such calculations for large-scale aperiodic systems are unfeasibly expensive and time-consuming. Therefore, the stiffness matrix is here built using molecular dynamics techniques. It is typical to express the interactions among atoms in terms of an interaction potential, Φ [4]. Of the many functions proposed for the interaction potential of a CNT, the one chosen for this study is the Tersoff potential using the optimized parameters found by Lindsay and Broido [98–100]. While modifications and improvements have been made to this potential [101, 102], which increase its ability to accurately model physical systems, the purpose of the interaction potential in this chapter is primarily for demonstrating the validity of order reduction techniques. The Tersoff potential combines ease of implementation with sufficient accuracy to reflect the impact of structural changes in the CNT on the stiffness matrix. The methods described here are applicable to any potential function that can be linearized in the manner that will be described.

The first step in the linearization process is to ensure that the system is at a stable equilibrium. A standard procedure in molecular dynamics, this is achieved by altering the positions of the atoms until the total potential energy reaches a local minimum [95]. This computation has been performed using the built-in energy minimization feature of the software package LAMMPS, with energy tolerance of 10^{-9} eV and force tolerance of 10^{-12} eVÅ⁻¹ [103]. While the minimum potential energy condition does not ensure stability, its stability can be checked by ensuring that all the predicted natural frequencies of the linearized system are real [104].

The potential energy of the system is

$$T(\mathbf{x}) = \frac{1}{2} \sum_{a \neq b} \Phi_{ab}(\mathbf{x}) \quad (4.2.2)$$

where Φ_{ab} is the interaction potential between atoms a and b . The relative stiffness of the

α^{th} and β^{th} degrees of freedom is

$$k_{\alpha\beta} = \frac{\partial^2 T(\mathbf{x})}{\partial x_\alpha \partial x_\beta} \quad (4.2.3)$$

where x_α and x_β indicate the α^{th} and β^{th} components of the displacement vector \mathbf{x} [95].

At this point, it is convenient to explain the nomenclature that will be used in the remainder of this chapter, as regards the positions of individual atoms. Consider a system of n atoms. Each atom is treated as a point mass, and has three degrees of freedom. It follows, therefore, that $\mathbf{x} \in \mathbb{R}^{3n \times 1}$. A single component of \mathbf{x} , x_α , indicates the position of a single degree of freedom of the system. Of course, the order in which the degrees of freedom are written in the position vector does not alter the way it functions, but for simplicity the convention used here is

$$\mathbf{x} = \begin{bmatrix} \mathbf{u}_1 \cdot \hat{\mathbf{e}}_1 \\ \mathbf{u}_1 \cdot \hat{\mathbf{e}}_2 \\ \vdots \\ \mathbf{u}_n \cdot \hat{\mathbf{e}}_3 \end{bmatrix} \quad (4.2.4)$$

where \mathbf{u}_a is the position vector of the a^{th} atom and $\{\hat{\mathbf{e}}_1, \hat{\mathbf{e}}_2, \hat{\mathbf{e}}_3\}$ is the set of unit vectors that define the coordinate system. Once again, it is implicit that \mathbf{x} is a function of time.

The formulation for $k_{\alpha\beta}$, the stiffness of one degree of freedom with respect to another, allows for a global stiffness matrix $\mathbf{K} \in \mathbb{R}^{\gamma \times \gamma}$, where $\gamma = 3n$ is the number of degrees of freedom in the system, to be constructed

$$\mathbf{K} := \begin{bmatrix} k_{11} & \dots & k_{1\gamma} \\ \vdots & \ddots & \\ k_{\gamma 1} & \dots & k_{\gamma\gamma} \end{bmatrix} \quad (4.2.5)$$

The mass matrix \mathbf{M} is defined as

$$\mathbf{M} := \begin{bmatrix} m_1 \mathbf{I}_3 & \mathbf{0} & \dots & \mathbf{0} \\ \mathbf{0} & m_2 \mathbf{I}_3 & & \vdots \\ \vdots & & \ddots & \mathbf{0} \\ \mathbf{0} & \dots & \mathbf{0} & m_n \mathbf{I}_3 \end{bmatrix} \quad (4.2.6)$$

where m_a is the mass of the a^{th} atom, and \mathbf{I}_3 is the 3×3 mass matrix. Using these definitions, the linearized equations of motion for this system of atoms can be written as

$$\mathbf{M}\ddot{\mathbf{x}} + \mathbf{K}\mathbf{x} = \mathbf{0} \quad (4.2.7)$$

The ability of the linearized Tersoff potential to predict the phonon dispersion and thermal conductivity of pristine graphene sheets and single-walled CNTs is validated against experimental data in Lindsay and Broido's [98] derivation of the improved Tersoff parameters. In that work, the components of the interatomic stiffness matrix \mathbf{K} are referred to as the harmonic interatomic force constants.

4.2.1 Order reduction techniques

For the purposes of this study, there are two systems to consider: a pristine (fully periodic) system, with mass matrix \mathbf{M}_p and stiffness matrix \mathbf{K}_p , and a perturbed system, with mass matrix $\mathbf{M}_d = \mathbf{M}_p + \delta\mathbf{M}$ and stiffness matrix $\mathbf{K}_d = \mathbf{K}_p + \delta\mathbf{K}$. The vibrational frequencies and modes for each system can be found from the following eigenproblems:

$$(\mathbf{K}_p - \mathbf{M}_p \omega_p^2) \mathbf{v}_p = \mathbf{0} \quad (4.2.8)$$

and

$$(\mathbf{K}_d - \mathbf{M}_d \omega_d^2) \mathbf{v}_d = \mathbf{0} \quad (4.2.9)$$

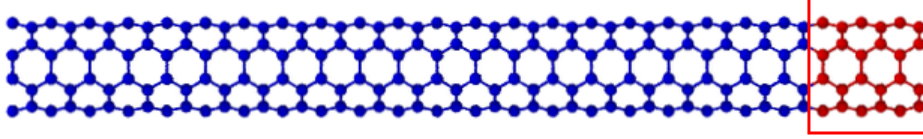


Figure 4.1: A (4,4) CNT with the unit cell highlighted and boxed. Note that the unit cell is not of minimal size—this is to ensure that the cell is large enough to contain an entire SWD.

where the symbols ω and \mathbf{v} represent a natural frequency and the corresponding mode vector or mode shape, respectively.

The periodicity of the pristine system makes it unnecessary to solve the full-order eigenproblem (eq. 4.2.8) for that case. Instead, the Floquet–Bloch theorem allows the order of the problem to be reduced to that of one periodic unit (referred to as a unit cell) with no loss of accuracy [4, 89, 105]. A unit cell of a CNT is shown in Fig. 4.1.

When the periodicity of the pristine system is broken by the presence of a defect, the Floquet–Bloch theorem is no longer applicable. Therefore, finding the modes and frequencies of the perturbed system is a much more computationally expensive process. To mitigate this, order reduction techniques are used to limit the size of the system while maintaining approximately accurate mode shapes and natural frequencies within a certain frequency range. The two methods of order reduction considered here are MDA and MMDA. While both have been described in detail elsewhere [14, 66, 94], their application to almost-periodic atomic systems is novel.

Both techniques follow the same basic steps: an order reduction matrix ($\mathbf{T} \in \mathbb{R}^{\gamma \times \zeta}$, where γ is the number of degrees of freedom in the full-order system and ζ is the number of degrees of freedom in the reduced-order system) is constructed. The manner in which the matrix \mathbf{T} is constructed is the only difference between the two methods. A reduced-order position vector \mathbf{y} is defined such that

$$\mathbf{x} = \mathbf{T}\mathbf{y} \tag{4.2.10}$$

Eq. 4.2.10 is substituted into the equations of motion (eq. 4.2.7), and the equations of

motion are left-multiplied by \mathbf{T}^T , resulting in

$$\mathbf{M}_r \ddot{\mathbf{y}} + \mathbf{K}_r \mathbf{y} = \mathbf{0} \quad (4.2.11)$$

where

$$\mathbf{K}_r = \mathbf{T}^T \mathbf{K}_d \mathbf{T} \quad (4.2.12)$$

and

$$\mathbf{M}_r = \mathbf{T}^T \mathbf{M}_d \mathbf{T} \quad (4.2.13)$$

The corresponding eigenproblem that results in the mode shapes and modal frequencies is then

$$(\mathbf{K}_r - \omega_r^2 \mathbf{M}_r) \mathbf{v}_y = \mathbf{0} \quad (4.2.14)$$

The prediction of natural frequencies from the reduced-order model is represented by ω_r . The modal vector \mathbf{v}_r from the reduced-order model in physical coordinates is computed by the following relationship:

$$\mathbf{v}_r = \mathbf{T}^T \mathbf{v}_y \quad (4.2.15)$$

4.2.2 Modal domain analysis

MDA seeks to reduce the order of the system by first transforming it from physical coordinates—each of which corresponds directly to the position of a single atom in a certain direction—to modal coordinates, in which the position vectors of atoms are given as a linear combination of vibrational modes of the pristine nanotube. Order reduction is then achieved by eliminating certain of these modal coordinates [94].

As the pristine system is periodic, its vibrational modes and frequencies can be found efficiently using the Floquet–Bloch theorem. These modes, denoted $\mathbf{v}_1, \dots, \mathbf{v}_\gamma$, together form a $\gamma \times \gamma$ matrix

$$\mathbf{V} = [\mathbf{v}_1 \dots \mathbf{v}_\gamma] \quad (4.2.16)$$

Note that the modes of this system are orthogonal; therefore, the matrix \mathbf{V} is of full rank. This matrix allows for position vectors to be transformed from the modal domain as follows:

$$\mathbf{x} = \mathbf{V}\mathbf{y} \quad (4.2.17)$$

where \mathbf{y} is a position vector in modal coordinates. As the matrix \mathbf{V} is of full rank, this transformation is isomorphic [106]. Order reduction can be achieved by removing certain modes from matrix \mathbf{V} to form the order reduction matrix, \mathbf{T} , in eq. 4.2.10

$$\mathbf{T} = [\mathbf{v}_\alpha \ \mathbf{v}_\beta \ \dots], \ \mathbf{v}_\alpha, \mathbf{v}_\beta, \dots \in \{\mathbf{v}_1 \ \dots \ \mathbf{v}_\gamma\}, \ \zeta := \text{Rank}(\mathbf{T}) < \gamma \quad (4.2.18)$$

It should be noted that the transformation from physical coordinates to reduced-order coordinates is no longer isomorphic, as the dimension of the modal coordinate space is lower than that of the physical coordinate space [106].

4.2.3 Modified modal domain analysis

MMDA applies the same rationale as MDA, with one significant difference: the order reduction matrix \mathbf{T} is built from the modes of the pristine system and the modes of other periodic systems, chosen to represent the differences in mode shapes due to the presence of defects [66]. In this case, only one such system will be used, and its modes are designated $\mathbf{v}_{A1} \dots \mathbf{v}_{A\gamma}$. Note that this system must be of the same order as the full system. Just as with MDA, the number of modes used to construct the transformation matrix must be less than the order of the full system, or else no order reduction is achieved. The order reduction matrix can, therefore, be written

$$\mathbf{T} = [\mathbf{v}_\alpha \ \mathbf{v}_\beta \ \dots \ \mathbf{v}_\rho \ \mathbf{v}_\sigma \ \dots], \ \mathbf{v}_\alpha, \mathbf{v}_\beta, \dots \in \{\mathbf{v}_1 \ \dots \ \mathbf{v}_\gamma\}, \ \mathbf{v}_\rho, \mathbf{v}_\sigma, \dots \in \{\mathbf{v}_{A1} \ \dots \ \mathbf{v}_{A\gamma}\} \quad (4.2.19)$$

Once again, $\zeta := \text{Rank}(\mathbf{T}) < \gamma$.

4.2.4 Defects

Two types of CNT defect are considered here: isotope defects and SWDs. Isotope defects refer simply to the presence of various carbon isotopes distributed through the structure that result in a perturbed mass matrix, while the stiffness matrix remains unchanged. As structural defects, SWDs influence how the atoms in a nanotube interact and so result in a perturbed stiffness matrix, but do not affect the mass matrix.

Isotope defect

As the nanotubes comprise carbon atoms, the masses used in the presence of isotope defects correspond to those of ^{12}C and ^{13}C . The resulting mass matrix is referred to as \mathbf{M}_d . The stiffness matrix is not affected — i.e. $\mathbf{K}_d = \mathbf{K}_p$.

For MDA, the only mode shapes that are required are those of the pristine system, which are found using the Floquet–Bloch theorem. MMDA attempts to improve on the accuracy of MDA by supplementing the order reduction matrix with mode shapes that reflect the characteristics of the defects, as well as the pristine system. To that end, a separate system is required that exhibits relevant behaviors of the perturbed system, but is itself periodic (and so can be readily analyzed). Following the approach used in [66, 107], this system is found by employing proper orthogonal decomposition (POD) [108, 109] to identify the dominant features in the mass matrix due to the defects.

As the aim of this analysis is to efficiently generate the basis vectors that form the matrix \mathbf{T} , eq. 4.2.10, using a periodic system that retains important characteristics of the perturbed system, the perturbed system is first broken down into cells, analogous to the repeated unit cell of the periodic system. Let η be the number of degrees of freedom in a unit cell. The masses of atoms in these cells will be compared, and the most prominent features will be used to form the unit cell for a new, ‘periodically perturbed’ system.

To divide the system into cells, the mass matrix \mathbf{M}_d can be split into $\nu = \gamma/\eta$ sub-matrices

as follows:

$$\mathbf{M}_d = \begin{bmatrix} \mathbf{M}_{d1} & \mathbf{0} & \dots & \mathbf{0} \\ \mathbf{0} & \mathbf{M}_{d2} & & \vdots \\ \vdots & & \ddots & \mathbf{0} \\ \mathbf{0} & \dots & \mathbf{0} & \mathbf{M}_{d\nu} \end{bmatrix} = \mathbf{M}_p + \begin{bmatrix} \delta\mathbf{M}_1 & \mathbf{0} & \dots & \mathbf{0} \\ \mathbf{0} & \delta\mathbf{M}_2 & & \vdots \\ \vdots & & \ddots & \mathbf{0} \\ \mathbf{0} & \dots & \mathbf{0} & \delta\mathbf{M}_\nu \end{bmatrix} \quad (4.2.20)$$

Each block-diagonal matrix of dimension η is the mass matrix of an individual cell. Furthermore, the atoms in the system are modeled as point masses, so each block-diagonal matrix $\delta\mathbf{M}_a$ is itself diagonal. A new, more concise matrix can be assembled thus

$$\mathbf{M}_c := [\text{diag}(\delta\mathbf{M}_1) \dots \text{diag}(\delta\mathbf{M}_\eta)] \quad (4.2.21)$$

where $\text{diag}(\delta\mathbf{M}_a)$ indicates a column vector containing the diagonal elements of $\delta\mathbf{M}_a$. $\mathbf{M}_c \in \mathbb{R}^{\eta \times \nu}$. Using a singular value decomposition, this matrix can be written as

$$\mathbf{M}_c = \mathbf{U}\mathbf{\Sigma}\mathbf{V}^T \quad (4.2.22)$$

where $\mathbf{U} \in \mathbb{R}^{\eta \times \eta}$, $\mathbf{\Sigma} \in \mathbb{R}^{\eta \times \nu}$ and $\mathbf{V} \in \mathbb{R}^{\nu \times \nu}$ [26,27]. $\text{diag}(\mathbf{\Sigma}) = [\sigma_1 \ \sigma_2 \ \dots \ \sigma_p \ 0 \ \dots \ 0]^T$, where $p = \min(\nu, \eta)$, and $\sigma_i \geq \sigma_{i+1}$. Eq. 4.2.22 can also be written as

$$\mathbf{M}_c = \sum_{i=1}^p \mathbf{u}_i \sigma_i \mathbf{v}_i^T \quad (4.2.23)$$

where \mathbf{u}_i is the i^{th} column of \mathbf{U} and \mathbf{v}_i is the i^{th} column of \mathbf{V} [14,109]. The columns of \mathbf{U} are the POD features of \mathbf{M}_c and form an orthonormal basis for the columns of \mathbf{M}_c . Furthermore, since $\sigma_1 \geq \sigma_{i+1}$, the first POD component represents the most dominant feature of \mathbf{M}_c , the second POD component represents the next dominant feature, and so on [108].

Using these POD features, new matrices, $\delta\mathbf{M}_{\text{POD}1}$ to $\delta\mathbf{M}_{\text{POD}p}$, are formed as follows: let

\mathbf{W}_i be a diagonal matrix, such that $\text{diag}(\mathbf{W}_i) = \mathbf{u}_i$; Then $\delta\mathbf{M}_{\text{POD}i}$ can be defined

$$\delta\mathbf{M}_{\text{POD}i} := \sigma_i \begin{bmatrix} \mathbf{W}_i & \mathbf{0} & \dots & \mathbf{0} \\ \mathbf{0} & \mathbf{W}_i & & \vdots \\ \vdots & & \ddots & \mathbf{0} \\ \mathbf{0} & \dots & \mathbf{0} & \mathbf{W}_i \end{bmatrix} \quad (4.2.24)$$

From each $\delta\mathbf{M}_{\text{POD}i}$, the periodically perturbed mass matrices $\mathbf{M}_{\text{POD}i} = \mathbf{M}_p + \delta\mathbf{M}_{\text{POD}i}$ can be defined. As these mass matrices are periodic, the natural frequencies and mode shapes of a system with stiffness matrix \mathbf{K}_p and mass matrix $\mathbf{M}_{\text{POD}i}$ can be efficiently calculated using the Floquet–Bloch theorem. A selection of the resulting mode shapes, denoted $\mathbf{v}_{\text{POD}ij}$ to indicate the j^{th} mode of the system build using the i^{th} POD feature, can be combined with certain modes of the pristine system to form the order reduction matrix, \mathbf{T} (eq. 4.2.19).

Stone-Wales defect

Introducing an SWD into the system requires rearranging the atoms, and so alters the stiffness matrix but not the mass matrix. An SWD can be created simply by taking two neighboring (i.e. bonded) atoms and rotating them 90° about the center of their bond, in the plane tangent to the surface of the nanotube (Fig. 4.2) [91,110]. As the positions of some of the atoms will have been changed, there is no guarantee that the system is at equilibrium. It is necessary, therefore, to repeat the energy minimization procedure. Once that has been completed, the perturbed stiffness matrix \mathbf{K}_p can be assembled in the same manner as for the pristine system. Note that the defect causes the atoms in its vicinity to be arranged into two heptagons and two pentagons—a defining characteristic of an SWD [91].

Analyzing the system using MDA proceeds in the same manner as for the system with isotope defects, and therefore needs no further explanation. MMDA, on the other hand, requires a different approach. It is neither feasible nor meaningful to break down the perturbed stiffness matrix and perform POD on it. The size of the matrix makes these computations

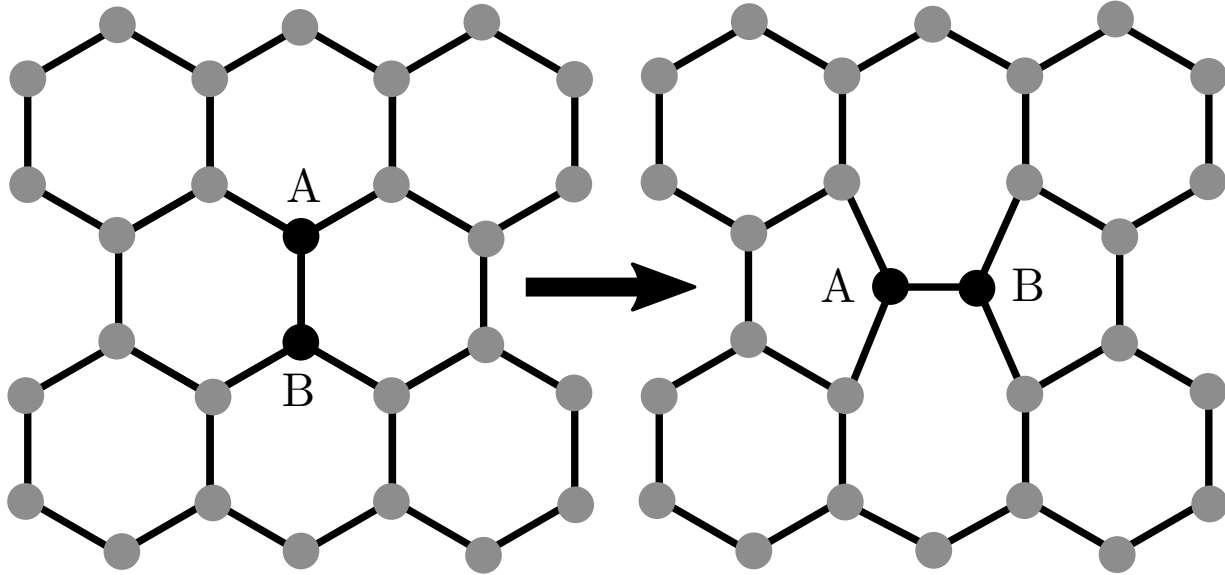


Figure 4.2: The formation of an SWD via the rotation of a carbon-carbon bond. Note that this transformation results in a system that requires equilibration.

very difficult, and there is no guarantee that the resulting POD features will produce a stable system. A similar problem occurs when the positions of the atoms are analyzed using POD. The features that are isolated must be energy minimized before their stiffness matrices can be calculated, which frequently results in the system either returning to its unperturbed state or becoming unstable and breaking apart.

An alternative approach is to once again break down the system into cells, but then directly compare the structure of each cell, choose the cell with the largest perturbation and use that cell as the basis for a ‘periodically perturbed’ system. For the case that is examined here—a single SWD—finding the most perturbed cell is simply a matter of identifying which cell contains the defect. To determine the modes of a system constructed using the most perturbed cell (the cell containing the defect), the Floquet–Bloch theorem requires information pertaining not only to the stiffnesses of the atoms in the unit cell relative to the other atoms in the unit cell, but also to the stiffnesses of those atoms relative to atoms in neighboring unit cells. If the cell containing an SWD is used as a unit cell, then every cell in this new system contains an SWD. This raises a problem: the defect in one cell can potentially interact with the defect in another—a situation that could only arise if the

perturbed system contained a high density of defects. To counteract this, the stiffnesses resulting from the interactions between the cell containing an SWD and the unperturbed cells around it are also included in the definition of the unit cell of the periodically perturbed system.

The entire process can be summarized mathematically as follows: it can be assumed without any loss of generality that the most varied cell is the first cell, i.e. the degrees of freedom pertaining to it are numbered 1 to η where η is the number of degrees of freedom in a cell. A transformation matrix can be defined

$$\mathbf{T}_c(k) = \begin{bmatrix} \mathbf{I}_\eta \\ \exp\left(i\frac{2\pi k}{\nu} \times 1\right) \mathbf{I}_\eta \\ \exp\left(i\frac{2\pi k}{\nu} \times 2\right) \mathbf{I}_\eta \\ \vdots \end{bmatrix} \quad (4.2.25)$$

where $\mathbf{T}_c \in \mathbb{R}^{\nu \times \eta}$ and $k \in \mathbb{Z}$, $0 \leq k < \nu$. The eigenproblem for the periodically perturbed system is then

$$(\mathbf{K} - \omega^2 \mathbf{M}) \mathbf{T}_c(k) \mathbf{v}_p = \mathbf{0} \quad (4.2.26)$$

where $\mathbf{v} \in \mathbb{R}^{\eta \times 1}$, so to extrapolate the corresponding mode of the complete partially perturbed system it is necessary to left-multiply it by \mathbf{T}_c . Note that the eigenproblem must be solved ν times, once with each possible value of wavenumber k , to produce the full set of frequencies and mode shapes for basis vectors in eq. 4.2.19.

4.3 Numerical results

To demonstrate the validity and relative effectiveness of these two techniques — MDA and MMDA — in approximating the vibrational modes and natural frequencies of a CNT containing defects, a series of test cases are constructed. Each test begins with a model of a pristine CNT. To avoid end effects, periodic boundary conditions are applied to the

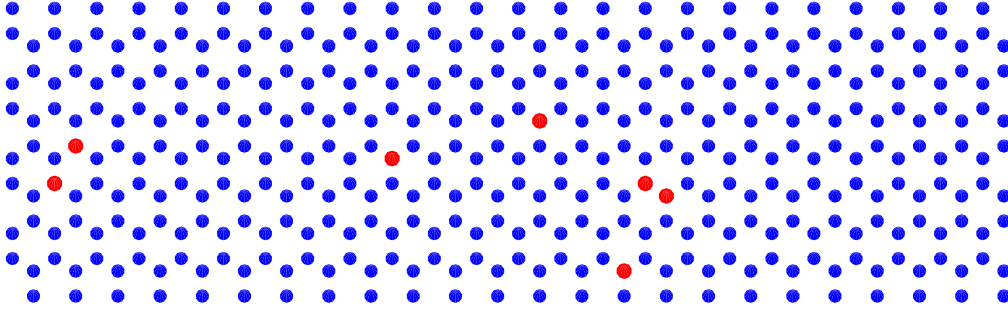


Figure 4.3: Arrangement of atoms in the isotope defect case, prior to graphene being rolled into a nanotube. ^{12}C atoms represented in blue, ^{13}C in red.

models. Several nanotubes of varying length, diameter and chirality have been considered. These results are quite similar; therefore, for the sake of brevity, only the results from the nanotube with chiral vector (4,4) and length 59.3\AA (aspect ratio ≈ 10) will be presented. This chiral vector indicates that this is an ‘armchair’ nanotube with a diameter of 5.425\AA . This nanotube model contains a total of 384 atoms (subsequently the full-order system contains 1152 degrees of freedom). Note that the periodic boundary condition means that the nanotube’s length is, in effect, infinite, so the length given above refers to the maximum vibrational wavelength of the full-order system.

Each of the two types of defects under consideration, isotope and Stone-Wales, is applied separately to the nanotube. For the isotope defect case, the isotope masses correspond to ^{12}C and ^{13}C atoms, with approximately 1.1% of the atoms in the system assigned the mass of ^{13}C in an effort to match the relative abundance of these isotopes in nature [111]. The distribution of isotopes in this model is illustrated in Fig. 4.3. Only the mass matrix, eq. 4.2.24, generated from the first POD feature is used to generate basis vectors for MMDA. The Stone-Wales case involves a single SWD, located at a randomly chosen position in the nanotube. The position of this defect and its impact on the overall shape of the nanotube is illustrated in Fig. 4.4.

Both MDA and MMDA achieve order reduction by approximating only certain modes of the full-order system. These modes are generally selected by first choosing a frequency range of interest, then building the order reduction matrices, equations 4.2.18 and 4.2.19,

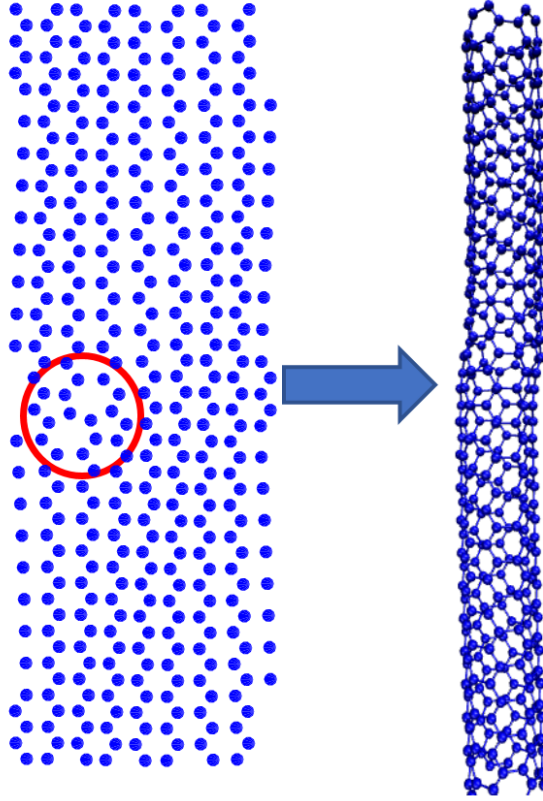


Figure 4.4: Structure of a CNT with an SWD. Defect circled in red. Three-dimensional rendering performed with visual molecular dynamics [112].

from modes with frequencies in this range [94]. In this study, approximations are made for the first 100 modes of the perturbed system — corresponding to the frequency range from 0 to 12.5 THz. The MMDA order reduction matrix contains the first 100 modes of the pristine system and the first 100 modes of the ‘periodically perturbed’ system that is generated using the methods described earlier. The MDA order reduction matrix is constructed from the first 200 modes of the pristine system. The choice of size of the order reduction matrices ensures that both order reduction techniques require approximately the same computational effort. Note that, while the use of 200 modes in creating the MDA order reduction matrix allows for the estimation of the first 200 modes of the perturbed system (with the expectation that the first 100 predicted modes will be more accurate than the second 100), only the first 100 modes of the MMDA approximation are expected to be relevant. For this reason, only the results relating to the first 100 modes are shown here.

In keeping with previous work on almost periodic systems [66, 107], the accuracy of the approximations found here is measured by comparing the frequency deviation of a given mode (the predicted frequency of the perturbed system minus the frequency of the corresponding mode of the pristine system) with the frequency deviation of the full-order model. Each of these values is presented as a percentage of the pristine frequency for the mode in question. In the cases that are considered here, the modal frequencies of the perturbed systems do not deviate drastically from those of the pristine system — in general, the frequency deviations are less than 5% of the frequency of the pristine system (figures 4.5 - 4.7). Therefore, a plot of the frequencies themselves does not provide much information concerning the accuracy of the order reduction techniques under consideration. One such plot (Fig. 4.5) is presented to illustrate this. Note that in all the results shown here, rigid body modes (modes that correspond to zero frequencies) are excluded, as both approximation methods are capable of predicting those modes exactly. Plots of the frequency deviations for the isotope defect and SWD cases are presented in figures 4.6 and 4.7, respectively. Each plot contains the results for the full-order system, in addition to the frequencies estimated using MDA and MMDA.

The modal frequencies are only one part of the results produced by these order reduction methods; both MDA and MMDA provide approximate mode shapes that correspond to each frequency. These mode shapes are critical in predicting or matching the results of spectroscopic analyses [5]. A comparison with the mode shapes of the full-order system is achieved here using the modal assurance criterion (MAC) [113], which takes two mode shapes and returns a value between zero and one (inclusive), where one indicates identical modes and zero indicates orthogonal modes.

To give a full picture of the relationship between the modes of the full-order system and the modes of the reduced-order systems, the MAC of each mode of the reduced-order systems is calculated with respect to each mode of the full-order system. Should the values on the diagonal of the plot be close to 1, this will show not only that the modes of the full-order system are correctly predicted by the reduced-order system, but also that the associated

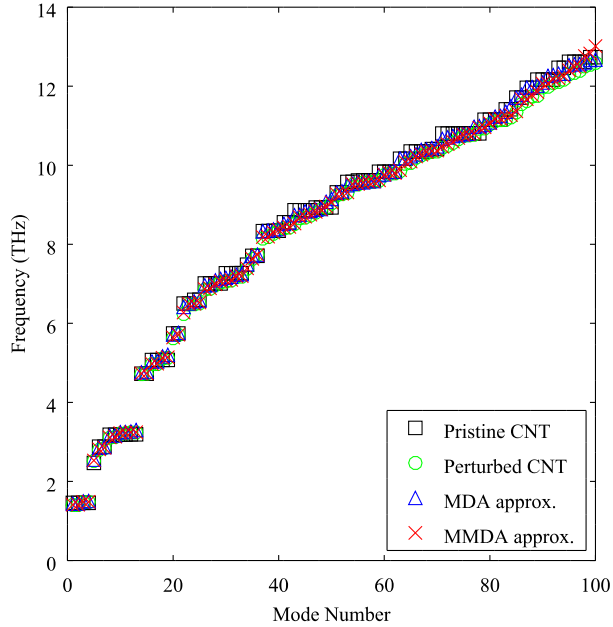


Figure 4.5: Vibrational frequencies of a pristine (4,4) CNT, as well as the same CNT with an SWD, and the approximations of the perturbed system using MDA and MMDA.

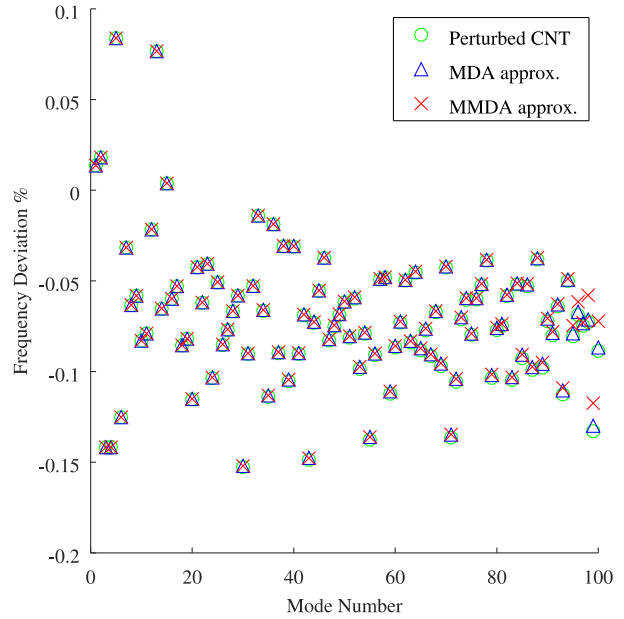


Figure 4.6: Frequency deviation of a (4,4) CNT with isotope defects.

modal frequencies are similar. Plots of the MAC for MDA and MMDA approximations of the system containing an isotope defect are shown in figures 4.8 and 4.9, while Fig. 4.10 shows the MAC of the modes of the pristine system with respect to the full-order system. Similar results for the SWD case are shown in figures 4.11 – 4.13.

The presence of defects in the otherwise periodic structure of a CNT has the potential to cause mode localization—the confinement of the majority of the energy of the mode to a small portion of the CNT [6,36]. To visualize localization in the defect-bearing CNT, the participation factor—after [114]—is used. Originally defined for a system in which each atom has one degree of freedom, the participation factor can be extended to three-dimensional systems as follows (note that this extension is necessary, as the application of the original form of the participation factor to a system with atoms having multiple degrees of freedom results in participation factor values that are dependent on the coordinate system used). For

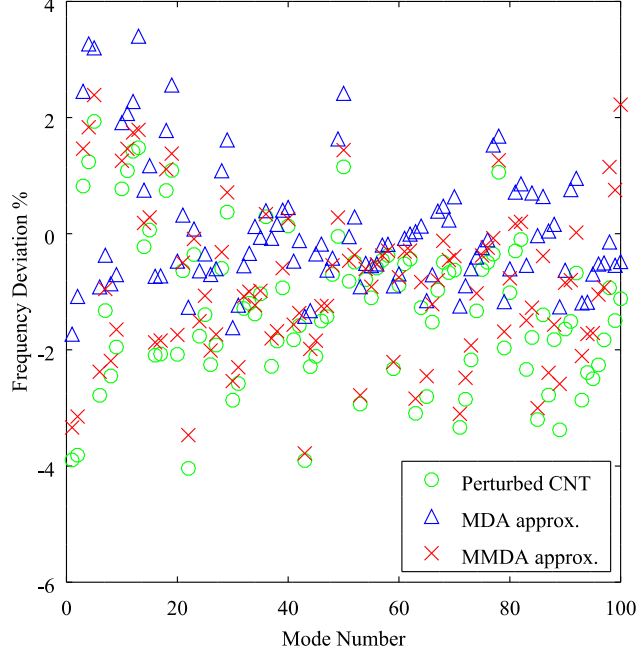


Figure 4.7: Frequency deviation of a (4,4) CNT with a single SWD.

each mode $\mathbf{v} = [v_1 \ v_2 \ \dots \ v_\gamma]^T$, a new vector μ is defined such that

$$\mu := \left[(v_1^2 + v_2^2 + v_3^2)^{1/2} \quad (v_4^2 + v_5^2 + v_6^2)^{1/2} \quad \dots \right]^T \quad (4.3.1)$$

In other words, μ contains the magnitude of the displacement of each atom in that mode of vibration. The participation factor (pf) is then calculated by first normalizing μ such that $(\mu \cdot \mu)^2 = 1$ then

$$pf := \frac{1}{(\mu \cdot \mu)^4} \quad (4.3.2)$$

The value of the participation factor lies between zero and the number of atoms in the system, with smaller values indicating more localized modes.

The participation factors of the full-order perturbed system and the pristine system are shown for the CNT with isotope defects and with an SWD in figures 4.14 and 4.15, respectively. As localization requires some perturbation of a periodic linear system, there is no localization in the modes of the pristine system [90]. Subsequently, the modes of the perturbed system with participation factors much lower than those of the pristine system

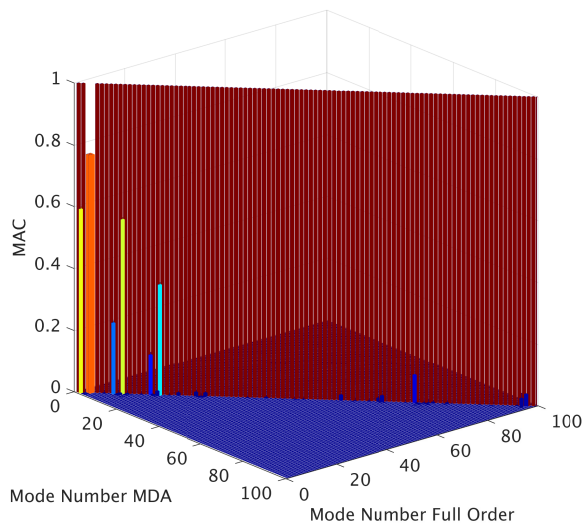


Figure 4.8: MAC of MDA modes versus full-order modes—*isotope defects*.

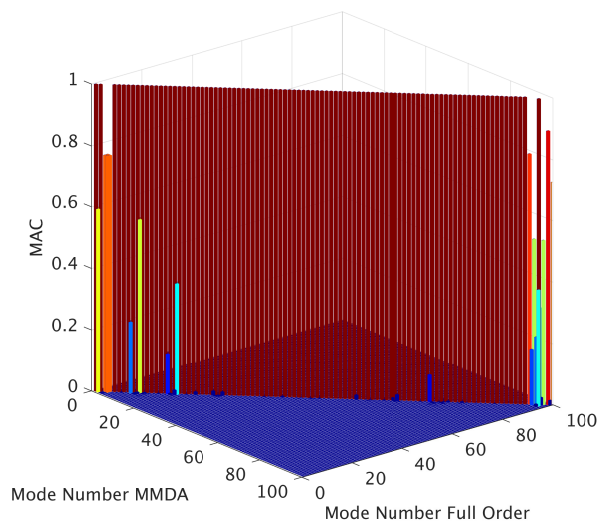


Figure 4.9: MAC of MMDA modes versus full-order modes—*isotope defects*.

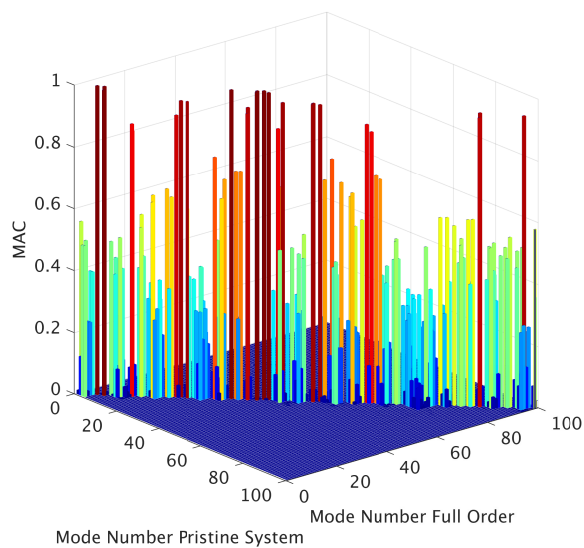


Figure 4.10: MAC of pristine modes versus full-order modes—*isotope defects*.

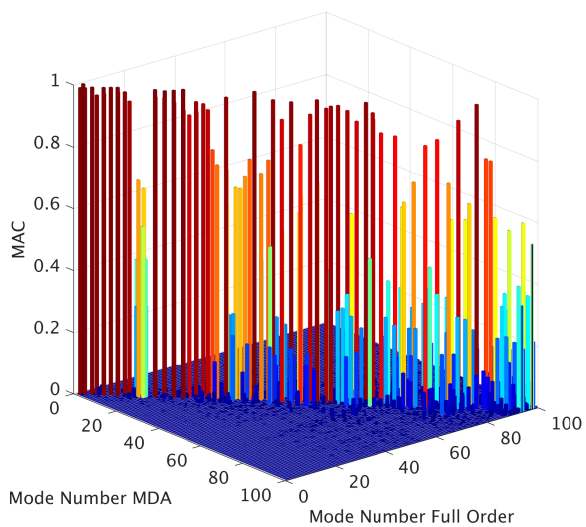


Figure 4.11: MAC of MDA modes versus full-order modes—*SWD*.

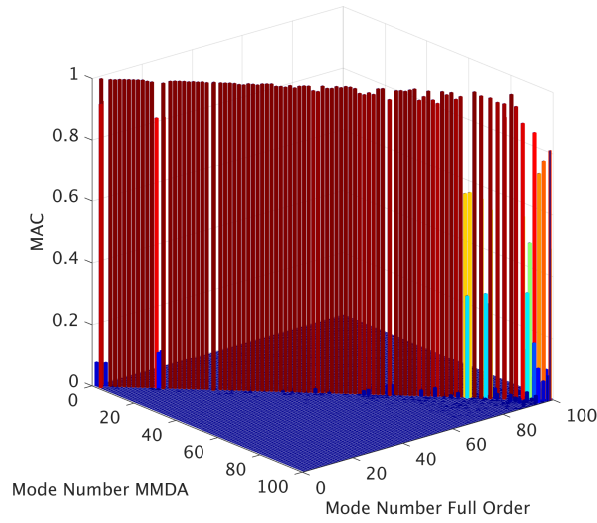


Figure 4.12: MAC of MMDA modes versus full-order modes—SWD.

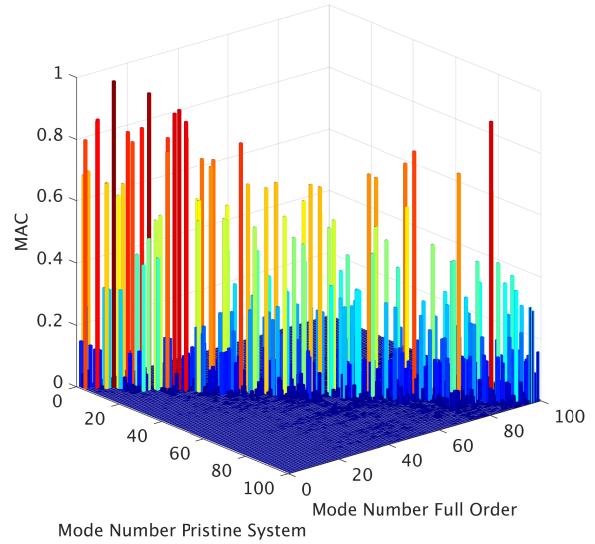


Figure 4.13: MAC of pristine modes versus full-order modes—SWD.

can be said to show localization.

To illustrate the relative efficiency of MDA and MMDA compared with solving the full-order eigenproblem, the Matlab implementations of MDA and MMDA developed for this article are timed as they estimate the eigenvalues and eigenvectors of the system. Note that the algorithm for finding the eigenvalues of the full-order system and the MDA algorithm do not change between the isotope defect case and the SWD case, while the MMDA algorithm does change. Running on a single core of an Intel Xenon E5-2650 v4 processor, with a clock speed of 2.2 GHz, the full-order system requires on average 19.251 s to solve. For the same system, the MDA algorithm requires only 0.652 s to run. For the isotope defect and SWD cases, MMDA requires 1.225 s and 1.395 s respectively. Each of these results is the average of 10 trials. Further increases in efficiency are possible as both the MDA and MMDA algorithms are highly parallelizable.

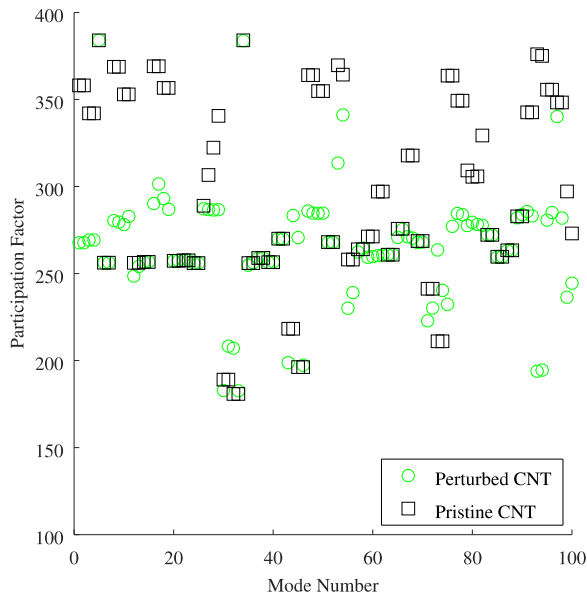


Figure 4.14: Participation factors for a CNT with isotope defects.

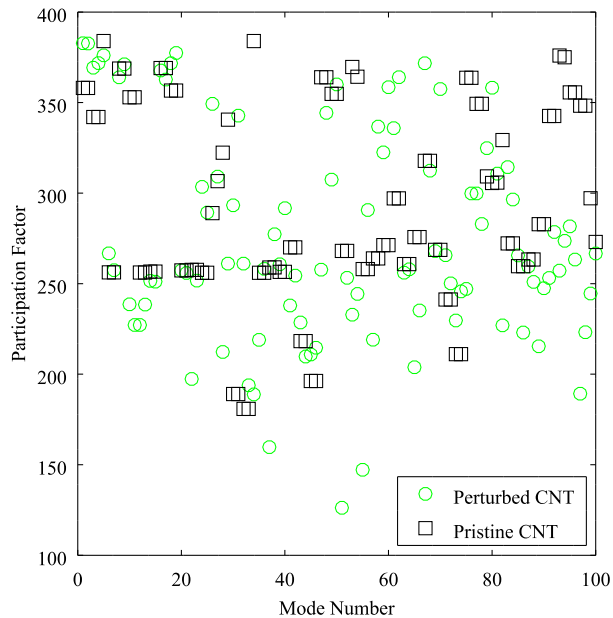


Figure 4.15: Participation factors of a CNT with an SWD.

4.4 Discussions

The aim of this investigation has been to determine whether either MDA or MMDA is a suitable technique for approximating the vibrational response of a CNT containing one or more defects. In this context, the vibrational response is summarized by the vibrational mode shapes and their associated frequencies. First, isotope defects are considered. From the frequency deviation of the full-order and reduced-order systems shown in Fig. 4.6, it is clear that both MDA and MMDA are successful in approximating the natural frequencies of the system. However, the MMDA results diverge slightly from the full-order results towards the end of the plotted frequency range—a result that is most likely due to the use of only 100 modes of the pristine system [66].

The frequency results alone are hardly enough to justify the use of order reduction techniques—the frequency deviation is so small that an analysis of the pristine system produces frequencies that are within 0.15% of the frequencies of the system that contains defects. A comparison of the mode shape of the pristine system and the system with isotope defects tells

a very different story, however. In Fig. 4.10, it is clearly shown that the mode shapes of the pristine system differ greatly from those of the perturbed system, with only about 10 modes of the two systems matching closely. Figures 4.8 and 4.9, which show the MAC results for the MDA and MMDA mode shapes, respectively, demonstrate that both techniques produce mode shapes that correspond almost exactly to the mode shapes of the full-order system.

The presence of an SWD—a much more notable defect than an isotope defect—results in relatively large frequency deviations. For the nanotube used here, that deviation peaks at roughly 4% of the frequency of the pristine nanotube. Therefore, the frequencies of the pristine nanotube alone are enough to motivate the development of reduced-order models. Of the two reduced-order models discussed here, it is clear from Fig. 4.7 that MMDA produces much more accurate frequency approximations than MDA. MMDA succeeds in matching almost every frequency of the full-order system much more closely than MDA.

The MAC results further indicate that MMDA produces a valid and useful approximation of the perturbed system. The modes of the pristine system deviate significantly with respect to those of the full-order perturbed system across the frequency range in question (Fig. 4.13), indicating that the presence of an SWD has a large impact on the system’s mode shapes. The MDA modes only matched the modes of the full-order system closely in a handful of cases (Fig. 4.11). MMDA, by contrast, produced high MAC values for the vast majority of modes (Fig. 4.12).

It is of especial interest that the reduced-order methods described here, particularly MMDA, are capable of efficiently predicting the mode shapes of the perturbed systems, as those systems have the potential to exhibit mode localization. The participation factor for each of the first 100 modes of the pristine and perturbed system are plotted in figures 4.14 and 4.15. Figure 4.14, which presents the results for the isotope defect case, shows that the participation factor for the modes of the perturbed system is generally lower than those of the pristine system, but not enough to be considered as localized modes. The lowest participation factor for the isotope defect case is slightly below 200, which is similar to the

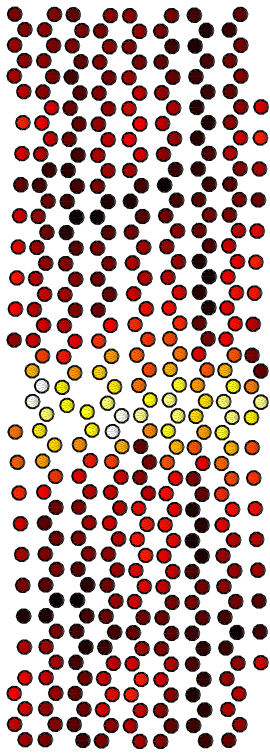
lowest participation factors of the pristine system. In the SWD case (Fig. 4.15), several modes have notably low participation factors. In particular, mode 51 has a participation factor of roughly 125, far lower than any modes of the pristine system. This is a strong indication that mode 51 of the full-order system exhibits localization.

An illustration of the relative ability of the two order reduction techniques to predict mode localization is given in Fig. 4.16. Here, mode 51 of the system containing the SWD is examined. As in Fig. 4.3, the nanotube is shown ‘unrolled’, to allow each atom to be clearly seen. The shade of each atom indicates the maximum displacement of that atom, divided by the largest displacement in that mode. Note that, due to frequency errors in the MDA results, the mode displayed is numbered mode 53 in the previous figures. This mode most closely matches mode 51 of the full-order system, and was therefore picked for this comparison. No such step was necessary for the MMDA results—mode 51 of the MMDA results matched mode 51 of the full-order results closely. It can be seen in Fig. 4.16 that, in both the full-order and MMDA results, the vast majority of atomic movement is confined to a small band containing the SWD. The atoms with the greatest displacement in both these results are members of the five-atom rings formed by the defect. The MDA results, on the other hand, erroneously show many more atoms participating in this mode, and the greatest displacement is not confined to atoms immediately involved in the defect.

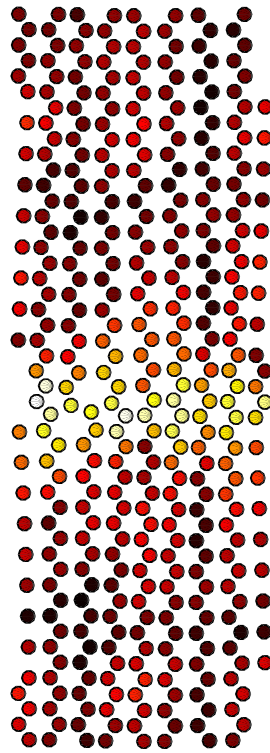
4.5 Conclusion

Overall, the results found in this study indicate that order reduction techniques—namely MDA and MMDA—allow the prediction of the vibrational properties of CNTs containing isotope defects and SWDs with significantly decreased computational effort. MDA produces accurate results for the isotope perturbation case, but is unable to closely match the frequencies or mode shapes when the stiffness matrix was perturbed by the presence of an SWD. For both types of defect, MMDA is able to accurately predict the first 100 natural

Perturbed - Full Order



Perturbed - MMDA



Perturbed - MDA

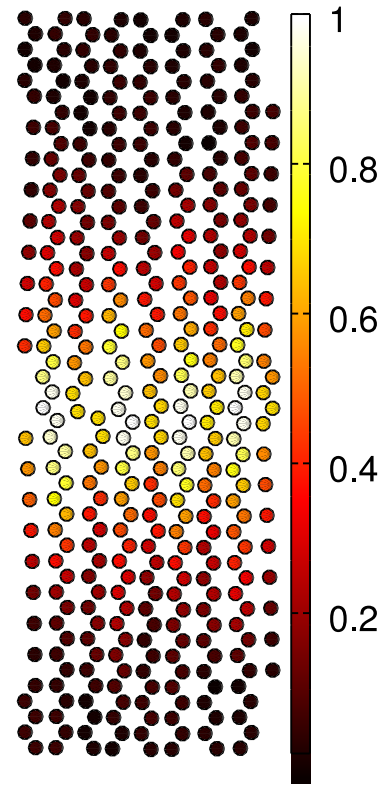


Figure 4.16: Maximum atom displacement of mode 51 from the full-order model, and as predicted by MMDA and MDA results.

frequencies and mode shapes based on a system with 200 degrees of freedom (the full-order system contained 1152 degrees of freedom). Furthermore, the mode shapes predicted using the MMDA method replicate the mode localization in the full-order system. The success of these methods demonstrates that they are suitable tools for future studies into the impact of defect types and locations on the phonon dispersion of CNTs of varying size and chirality.

Chapter 5

Reduced-Order Models of Carbon

Nanotubes: Multi-Vacancy Defects

5.1 Introduction

The isotope and Stone-Wales defects examined in the previous chapter are, in some respects, small perturbations to the structure of a single-walled carbon nanotubes (SWCNT). Each defect impacts only the mass or stiffness of the system, and the perturbed system contains the same number of degrees of freedom as the pristine system. A defect with a potentially larger impact, which will be considered in this chapter, is a multi-vacancy defect (MVD) (the absence of a group of atoms from a CNT). It should be noted that single vacancies (the absence of isolated atoms) in SWCNTs are expected to be unstable [115], but stable multi-vacancies are readily induced [116], well documented [117], and are expected to produce significant changes to the mechanical properties of a SWCNT [118]¹. The calculation of these properties, specifically the natural frequencies and normal modes of vibration of the SWCNT, without order reduction would be extremely costly due to the aperiodicity of the MVDs. A distinguishing feature of SWCNT with vacancy defects is that they contain fewer atoms than a comparable pristine SWCNT. As a result, modified modal domain analysis

¹In this chapter, it becomes essential to differentiate between single-walled and multi-walled carbon nanotubes, as the nature and impact of MVD differs greatly between these two types of CNT [115]

(MMDA) is not applicable here as it is not clear how a pristine system will be perturbed in a periodic manner to capture the characteristics of a vacancy defect.

A novel method of order reduction for a SCWNT with MVDs is presented here. The method, called modal domain reduction (MDR), permits the defect-bearing system to contain fewer degrees of freedom than the pristine system. This is achieved by combining elements of modal domain analysis (MDA) and dynamic reduction (DR), along with stipulations for handling the degrees of freedom of the pristine system that are not present in the defect-bearing system. The DR method is an approach that splits a system into primary and secondary degrees of freedoms and reduces the order of the system by explicitly calculating the behavior of the primary degrees of freedom while approximating the influence of the secondary degrees of freedom at some given frequency [119].

MDR is demonstrated on two example SWCNT models with MVDs. Care is taken to produce molecular dynamics (MD) models of vacancy-bearing SWCNTs that exhibit the ‘self-healing’ expected of irradiated CNTs [116, 118, 120]. These models are then linearized, and the MDR is applied to reduce the size of the linear systems. Finally, the natural frequencies and normal modes of their reduced-order models are calculated and compared with those of the full-order models, to illustrate the success of this method. As with other order reduction methods, MDR allows the user to select a band of frequencies in which error is minimized.

5.2 Methods

5.2.1 Molecular Dynamics

Two types of models are used in this work: MD models and linearized approximations of those MD models. To avoid confusion, only the MD models will be referred to here as ‘models’, while the linearized approximations will be called ‘systems’. The 2nd generation Reactive Empirical Bond Order (REBO) potential is chosen to govern the carbon-carbon

interaction in the MD model of the SWCNT, as it provides sufficient detail to capture not only the behavior of sp^2 bonded carbon atoms but also those bonds whose order has been altered by the presence of the vacancy [101]. The parameters used are those developed by Brenner *et al.* and modified by Lindsay and Broido to better match the experimentally determined phonon dispersion of graphene [98].

The MD model of a defect-bearing SWCNT begin with a pristine SWCNT with periodic boundary conditions on its ends, to prevent the effects of termination impacting the results. This model is energy minimized using the conjugate-gradient method built into the LAMMPS software package [103]. Energy minimization ensures that the system is at static equilibrium, which has been found to be stable for all simulated cases. This SWCNT will be referred to as the pristine model.

A multi-vacancy is created in the SWCNT by removing a cluster of neighboring atoms (see Figs. 5.1 and 5.2). This can result in the extensive re-arrangement of its structure in the region of the defect [120,121]. It is therefore necessary to allow the SWCNT model to reach a more stable (or lower energy) equilibrium than could be found through conjugate-gradient energy minimization alone. This is achieved by simulated annealing and quenching [116].

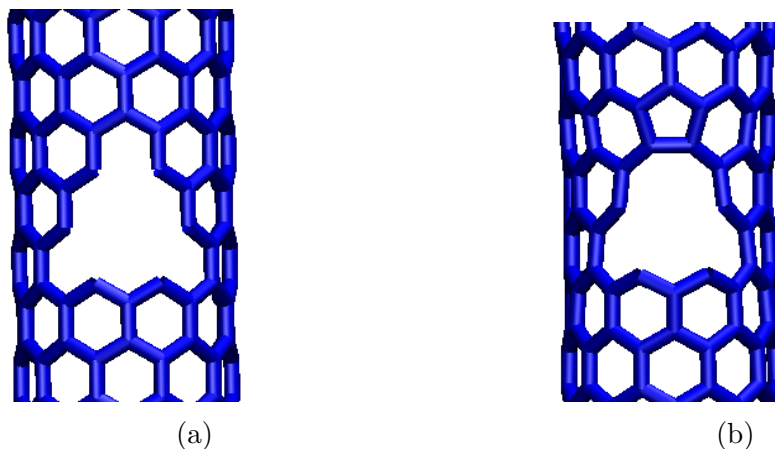


Figure 5.1: Detail of a four atom multi-vacancy in a (10,0) nanotube (a) before and (b) after simulated annealing and quenching. Figure generated using VMD [112].

The model is initially energy minimized to prevent a temperature spike at the beginning of the simulation caused by residual unbalanced forces. The temperature of the model is

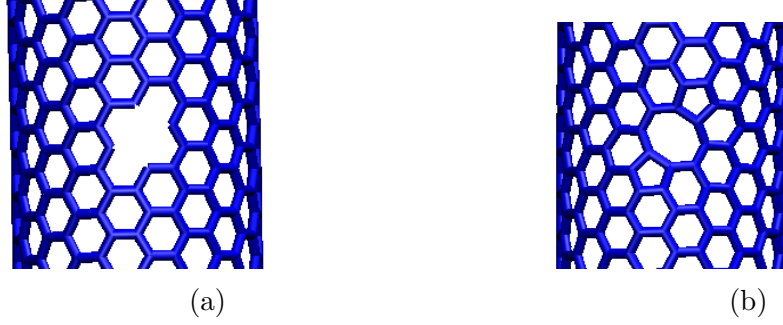


Figure 5.2: Detail of a two atom multi-vacancy in a (10,10) nanotube (a) before and (b) after simulated annealing and quenching. Figure generated using VMD [112].

controlled using a Nosé-Hover thermostat [122], and is increased from 0° K to 1500° K over the course of 10 ps (the number of atoms in the system and the volume of the simulation domain are held constant). This high temperature is chosen to allow the expected rearrangement of atoms to take place on a feasible time scale for atomistic simulation. The model is held at 1500° K for 100 ps, then cooled to absolute zero at a rate of 0.1° K/fs. Similar parameters are used by Krasheninnikov et al. [116]. The system is then energy minimized again, to ensure that it contains no unbalanced forces prior to linearization.

5.2.2 Linearization

Natural frequencies and normal modes are only rigorously defined for linear systems – systems in which the interatomic forces are linearly proportional to the displacements of atoms from equilibrium [68]. It is therefore necessary to linearize a MD model about its static equilibrium configuration to compute the linear stiffness matrix. The linearization is achieved by using a finite difference method to calculate the stiffness between each pair of degrees of freedom (DOFs) in the model as follows:

$$k_{\alpha\beta} = \frac{\partial^2 T(\mathbf{x})}{\partial x_\alpha \partial x_\beta} = \frac{\partial f_\alpha(\mathbf{x})}{\partial x_\beta} \approx \frac{f_\alpha(\mathbf{x} + \Delta \mathbf{x}_\beta) - f_\alpha(\mathbf{x} - \Delta \mathbf{x}_\beta)}{2\Delta x_\beta} \quad (5.2.1)$$

where T is the total potential energy of the model, f_α is the force on the α^{th} DOF, and \mathbf{x} is a vector containing the positions of each atom. Here, x_α and x_β are the components of

\mathbf{x} corresponding to the α^{th} and β^{th} DOFs, and $\Delta\mathbf{x}_\beta$ indicates a vector with all elements as zeros except one, which is Δx_β at the location of the β^{th} DOF. This method requires that the system be at equilibrium. The stiffness matrix of the perturbed system, \mathbf{K}_v , is then constructed from these stiffnesses, such that $k_{\alpha\beta}$ is the component in the α^{th} row and β^{th} column of \mathbf{K}_v . The same process is applied to the pristine model to produce the stiffness matrix \mathbf{K}_p . Note that the MVD in the perturbed system means that \mathbf{K}_v and \mathbf{K}_p are not of the same size.

The atoms in the linearized model can be represented as point masses, allowing the mass matrices \mathbf{M}_v and \mathbf{M}_p to be assembled as

$$\mathbf{M}_p := \begin{bmatrix} m_1\mathbf{I}_3 & \mathbf{0} & \dots & \mathbf{0} \\ \mathbf{0} & m_2\mathbf{I}_3 & & \vdots \\ \vdots & & \ddots & \mathbf{0} \\ \mathbf{0} & \dots & \mathbf{0} & m_n\mathbf{I}_3 \end{bmatrix} \quad \mathbf{M}_v := \begin{bmatrix} m_1\mathbf{I}_3 & \mathbf{0} & \dots & \mathbf{0} \\ \mathbf{0} & m_2\mathbf{I}_3 & & \vdots \\ \vdots & & \ddots & \mathbf{0} \\ \mathbf{0} & \dots & \mathbf{0} & m_{n-r}\mathbf{I}_3 \end{bmatrix} \quad (5.2.2)$$

where \mathbf{I}_3 is the 3×3 identity matrix, n is the number of atoms in the pristine system, r is the number of atoms removed to form the MVD, and m_i is the mass of the i^{th} atom.

The linearized equations of motion for the pristine and perturbed systems are

$$\mathbf{M}_p\ddot{\mathbf{x}}_p + \mathbf{K}_p\mathbf{x}_p = \mathbf{0} \quad (5.2.3a)$$

$$\mathbf{M}_v\ddot{\mathbf{x}}_v + \mathbf{K}_v\mathbf{x}_v = \mathbf{0} \quad (5.2.3b)$$

where \mathbf{x}_p and \mathbf{x}_v are displacement vectors of pristine and perturbed systems, respectively. Here, it is assumed that all atoms have the same mass, m , therefore $\mathbf{M}_v = m\mathbf{I}_{3(n-r)}$.

5.2.3 Order reduction

Natural frequencies and normal modes of the perturbed system can be calculated from the eigenproblem

$$(\mathbf{K}_v - \omega_i^2 \mathbf{M}_v) \mathbf{v}_i = \mathbf{0} \quad (5.2.4)$$

where ω_i indicates a natural frequency of the system and \mathbf{v}_i is the correspond mode shape. Solving this eigenproblem for the full-order system can be computationally expensive, making the analysis of the full system impractical for models that approach the size of physical CNT. To enable the calculation of the natural frequencies and normal modes of a large system containing MVDs, an order reduction method has been developed. This method is the combination of modal domain analysis (MDA) and dynamic reduction (DR).

The method of order reduction used here has similarities to the modal reduction method developed by Kammer [123] and the System Equivalent Reduction Expansion Process (SEREP) method [124], where the system is first transformed into modal coordinates, then its order is reduced using dynamic condensation. These methods are unsuited to this type of problem, however, as they use the modes of the full-order system to perform the transformation into modal coordinates [119]. Fortunately, for defect-bearing CNTs there exists a pristine system that is periodic and can be analyzed efficiently. If, as with MDA, it is assumed that the modes of the perturbed system are related to those of the pristine system, the modes of the pristine system can be used to transform the system to modal coordinates. The subsequent application of dynamic condensation permits the possibility that many modes of the pristine system, which need not have similar frequencies, can participate in a mode of the perturbed system. As the method described here differs in key ways from both MDA and existing modal reduction methods, but shares fundamental similarities with both, it will be referred to as modal domain reduction (MDR).

The transformation to modal coordinates requires several steps. First the modes of the pristine system, $\mathbf{v}_1, \dots, \mathbf{v}_{3n}$, where n is the number of atoms in the system, must be found

using Bloch's theorem [4]. Let these modes be numbered in order of ascending frequency. These modes can then be combined into a matrix

$$\mathbf{V} = [\mathbf{v}_1 \dots \mathbf{v}_{3n}] \quad (5.2.5)$$

In the case of a vacancy defect, the pristine system contains more atoms than the perturbed system. Therefore, the rows of \mathbf{V} that correspond to the physical coordinates of those atoms must be removed. This intermediate matrix will be referred to as \mathbf{V}' . Finally, the number of columns must also be reduced to match the number of DOFs in the perturbed system. Therefore, the $3r$ highest modes are eliminated from the matrix \mathbf{V}' (i.e. the last $3r$ columns). The resulting matrix will be referred to as Ψ . It should be noted that while the matrix \mathbf{V} is of full rank, arbitrarily removing columns from \mathbf{V}' does not guarantee that Ψ will be of full rank. However, attempting to ensure that Ψ is of full rank is an additional computational burden which does not noticeably improve the accuracy of the results in the cases tested here.

A modal coefficient vector, \mathbf{y} , is defined such that

$$\mathbf{x}_v = \Psi \mathbf{y} \quad (5.2.6)$$

Substituting eq. 5.2.6 into eq. 5.2.3b and left-multiplying by Ψ^T results in

$$\mathbf{M}_m \ddot{\mathbf{y}} + \mathbf{K}_m \mathbf{y} = \mathbf{0} \quad (5.2.7)$$

where

$$\mathbf{K}_m = \Psi^T \mathbf{K}_v \Psi \quad (5.2.8a)$$

$$\mathbf{M}_m = \Psi^T \mathbf{M}_v \Psi \quad (5.2.8b)$$

The subscript m denotes the use of modal coordinates. Now that the transformation to modal

coordinates has been established, the order of the system can be reduced using dynamic condensation (full details of this method can be found in [119]). The modal coefficient vector is partitioned into primary and secondary modes, resulting in similar partitions of the \mathbf{K}_m and \mathbf{M}_m matrices. It can be assumed without any loss of generality that the primary modes appear first.

$$\mathbf{y} = \begin{bmatrix} \mathbf{y}_p \\ \mathbf{y}_s \end{bmatrix} \quad (5.2.9a)$$

$$\mathbf{K}_m = \begin{bmatrix} \mathbf{K}_{pp} & \mathbf{K}_{ps} \\ \mathbf{K}_{sp} & \mathbf{K}_{ss} \end{bmatrix} \quad (5.2.9b)$$

$$\mathbf{M}_m = \begin{bmatrix} \mathbf{M}_{pp} & \mathbf{M}_{ps} \\ \mathbf{M}_{sp} & \mathbf{M}_{ss} \end{bmatrix} \quad (5.2.9c)$$

In this chapter, s and p , in normal type, act as subscripts to denote the primary and secondary modes. s and p , italicized, are integers that indicate the number of primary and secondary modes, respectively. Note that calculating the frequencies and modes of \mathbf{K}_{pp} and \mathbf{K}_{pp} is equivalent to analyzing the system using MDA [14].

Rearranging the eigenproblem $(\mathbf{K}_m - \omega_i^2 \mathbf{M}_m) \mathbf{v}_i = \mathbf{0}$ to solve for the secondary modal coefficient vector \mathbf{y}_s produces

$$\mathbf{y}_s = -(\mathbf{K}_{ss} - \omega^2 \mathbf{M}_{ss})^{-1} (\mathbf{K}_{sp} - \omega^2 \mathbf{M}_{sp}) \mathbf{y}_p \quad (5.2.10)$$

Subsequently,

$$\mathbf{y} = \mathbf{T}(\omega) \mathbf{y}_p \quad (5.2.11)$$

where

$$\mathbf{T}(\omega) = \begin{bmatrix} \mathbf{I} \\ \mathbf{R}_D(\omega) \end{bmatrix} \quad (5.2.12a)$$

$$\mathbf{R}_D = -(\mathbf{K}_{ss} - \omega^2 \mathbf{M}_{ss})^{-1} (\mathbf{K}_{sp} - \omega^2 \mathbf{M}_{sp}) \quad (5.2.12b)$$

Substituting eq. 5.2.11 into eq. 5.2.7 and pre-multiplying by $\mathbf{T}(\omega)^T$,

$$\mathbf{M}_r \ddot{\mathbf{y}}_p + \mathbf{K}_r \mathbf{y}_p = \mathbf{0} \quad (5.2.13)$$

where

$$\mathbf{K}_r = \mathbf{T}(\omega)^T \mathbf{K}_m \mathbf{T}(\omega) \quad (5.2.14a)$$

$$\mathbf{M}_r = \mathbf{T}(\omega)^T \mathbf{M}_m \mathbf{T}(\omega) \quad (5.2.14b)$$

The reduced-order model in eq. 5.2.13 is the MDR method, which requires that a frequency, ω , be specified to account for inertial terms in the equations of motion. This reduced-order model will be most accurate in the neighborhood of chosen ω . If a wide range of natural frequencies are required, it may be necessary to generate several such models to ensure accuracy.

5.3 Estimation of Errors in MDA and MDR

5.3.1 Modal domain analysis (MDA)

Assuming that the transformation matrix Ψ is orthonormal,

$$\mathbf{M}_m = m\mathbf{I} \quad (5.3.1)$$

Therefore, eq. 5.2.7 can be written as

$$\ddot{\mathbf{y}} + \frac{1}{m} \mathbf{K}_m \mathbf{y} = \mathbf{0} \quad (5.3.2)$$

The eigenvalues of this system, λ , then satisfy the equation

$$\det \left(\frac{1}{m} \mathbf{K}_m - \lambda \mathbf{I} \right) = 0 \quad (5.3.3)$$

Alternately, eq. 5.3.3 can be written as

$$\det(\mathbf{A} + \mathbf{E} - \lambda\mathbf{I}) = 0 \quad (5.3.4)$$

where

$$\mathbf{A} = \frac{1}{m} \begin{bmatrix} \mathbf{K}_{pp} & \mathbf{0} \\ \mathbf{0} & \mathbf{K}_{ss} \end{bmatrix} \quad (5.3.5a)$$

$$\mathbf{E} = \frac{1}{m} \begin{bmatrix} \mathbf{0} & \mathbf{K}_{ps} \\ \mathbf{K}_{sp} & \mathbf{0} \end{bmatrix} \quad (5.3.5b)$$

using the partitions of \mathbf{K}_m defined in eq. 5.2.9b. Then, from theorem 2 of [125]

$$\left| \lambda \left(\frac{1}{m} \mathbf{K}_m \right)_i - \lambda(\mathbf{A})_i \right| \leq \frac{2 \|\mathbf{E}\|^2}{\eta_i + \sqrt{\eta_i^2 + 4 \|\mathbf{E}\|^2}} \leq \|\mathbf{E}\| \quad (5.3.6)$$

where $\|\mathbf{E}\|$ is the spectral norm of \mathbf{E} , $\lambda(\cdot)_i$ indicates the i^{th} eigenvalues of a matrix, and

$$\eta_i := \begin{cases} \min_{\mu_2 \in \lambda(\frac{1}{m} \mathbf{K}_{ss})} \left| \tilde{\lambda}_i - \mu_2 \right|, & \text{if } \tilde{\lambda}_i \in \lambda(\frac{1}{m} \mathbf{K}_{pp}) \\ \min_{\mu_1 \in \lambda(\frac{1}{m} \mathbf{K}_{pp})} \left| \tilde{\lambda}_i - \mu_1 \right|, & \text{if } \tilde{\lambda}_i \in \lambda(\frac{1}{m} \mathbf{K}_{ss}) \end{cases} \quad (5.3.7)$$

In other words, η_i is the gap between an eigenvalue of \mathbf{A} (which, from the definition of \mathbf{A} , must be an eigenvalue of either $\frac{1}{m} \mathbf{K}_{pp}$ or $\frac{1}{m} \mathbf{K}_{ss}$), and the closet eigenvalue of the other submatrix of \mathbf{A} ($\frac{1}{m} \mathbf{K}_{ss}$ or $\frac{1}{m} \mathbf{K}_{pp}$). Because reduced-order models from MDA are represented by \mathbf{K}_{pp} and \mathbf{M}_{pp} , a relatively loose upper bound on the eigenvalue error of the MDA approximation is given by $\|\mathbf{E}\|$.

5.3.2 Modal domain reduction (MDR)

Consider the reduced-order system in eq. 5.2.13. The eigenproblem resulting from this system is then

$$(\mathbf{K}_r - \bar{\omega}^2 \mathbf{M}_r) \mathbf{u} = \mathbf{0} \quad (5.3.8)$$

Using eq. 5.2.12, 5.2.14a and 5.2.14b,

$$\left[\mathbf{K}_{pp} + \mathbf{R}_D(\omega)^T \mathbf{K}_{sp} + \mathbf{K}_{ps} \mathbf{R}_D(\omega) + \mathbf{R}_D(\omega)^T \mathbf{K}_{ss} \mathbf{R}_D(\omega) - \bar{\omega}^2 \left(\mathbf{M}_{pp} + \mathbf{R}_D(\omega)^T \mathbf{M}_{sp} + \mathbf{M}_{ps} \mathbf{R}_D(\omega) + \mathbf{R}_D(\omega)^T \mathbf{M}_{ss} \mathbf{R}_D(\omega) \right) \right] \mathbf{u} = \mathbf{0} \quad (5.3.9)$$

Note that $\bar{\omega}$ indicates a natural frequency of the reduced-order system (in other words, a frequency predicted by the reduced-order system), while ω is a guessed frequency. Because of eq. 5.3.1, $\mathbf{M}_{ps} = \mathbf{0}$. Therefore,

$$\mathbf{R}_D(\omega) = -(\mathbf{K}_{ss} - \omega^2 \mathbf{M}_{ss})^{-1} \mathbf{K}_{sp} \quad (5.3.10)$$

Due to the assumptions made in the formulation of transformation matrix $\mathbf{T}(\omega)$, a natural frequency of the reduced-order system, $\bar{\omega}$, is guaranteed to be a natural frequency of the full-order system when $\omega = \bar{\omega}$. Subsequently, error is expected when $\omega \neq \bar{\omega}$.

It is established in [126] that

$$(\mathbf{K}_{ss} - \bar{\omega}^2 \mathbf{M}_{ss})^{-1} = \mathbf{K}_{ss}^{-1} + \sum_{\nu=1}^s \boldsymbol{\varphi}_\nu \boldsymbol{\varphi}_\nu^T \frac{\bar{\omega}^2}{\sigma_\nu (\sigma_\nu - \bar{\omega})} \quad (5.3.11)$$

where σ_ν and $\boldsymbol{\varphi}$ are eigenvalues and eigenvectors, respectively, of the system defined by \mathbf{K}_{ss} and \mathbf{M}_{ss} , such that $\boldsymbol{\varphi}_\nu \mathbf{M}_{ss} \boldsymbol{\varphi}_\nu^T = 1$. This will be referred to as the residual system. From eq. 5.3.11,

$$(\mathbf{K}_{ss} - \omega^2 \mathbf{M}_{ss})^{-1} = \mathbf{K}_{ss}^{-1} + \sum_{\nu=1}^s \boldsymbol{\varphi}_\nu \boldsymbol{\varphi}_\nu^T \frac{\omega^2}{\sigma_\nu (\sigma_\nu - \omega)} \quad (5.3.12)$$

Using eq. 5.3.10, 5.3.11, and 5.3.12,

$$\mathbf{R}_D(\omega) = -(\mathbf{K}_{ss} - \bar{\omega}^2 \mathbf{M}_{ss})^{-1} \mathbf{K}_{sp} + \sum_{\nu=1}^s \boldsymbol{\varphi}_\nu \boldsymbol{\varphi}_\nu^T q_\nu \mathbf{K}_{sp} \quad (5.3.13)$$

where

$$q_\nu = \frac{\bar{\omega}^2 - \omega^2}{(\sigma_\nu - \bar{\omega}^2)(\sigma_\nu - \omega^2)} \quad (5.3.14)$$

Eq. (11) is exact when ω is exactly equal to the natural frequency, $\bar{\omega}$. Otherwise,

$$\mathbf{y}_s \approx \mathbf{R}_D(\omega) \mathbf{y}_p \quad (5.3.15)$$

Substituting eq. 5.3.13 into eq. 5.3.15,

$$\mathbf{y}_s \approx -(\mathbf{K}_{ss} - \bar{\omega}^2 \mathbf{M}_{ss})^{-1} \mathbf{K}_{sp} \mathbf{y}_p + \sum_{\nu=1}^s \boldsymbol{\varphi}_\nu \boldsymbol{\varphi}_\nu^T q_\nu \mathbf{K}_{sp} \mathbf{y}_p \quad (5.3.16)$$

The first term on the right-hand side of eq. 5.3.16 is identically equal to the exact \mathbf{y}_s . Let the second term be called \mathbf{y}_{err} . A measure of the error is the ratio of the norms of \mathbf{y}_{err} and \mathbf{y}_p

$$\frac{\|\mathbf{y}_{\text{err}}\|}{\|\mathbf{y}_p\|} \leq \left\| \sum_{\nu=1}^s \boldsymbol{\varphi}_\nu \boldsymbol{\varphi}_\nu^T q_\nu \mathbf{K}_{sp} \right\| \leq \left\| \sum_{\nu=1}^s \boldsymbol{\varphi}_\nu \boldsymbol{\varphi}_\nu^T q_\nu \right\| \|\mathbf{K}_{sp}\| \quad (5.3.17)$$

Since \mathbf{K}_{ss} and \mathbf{M}_{ss} are Hermitian, it can be assumed the eigenvectors $\boldsymbol{\varphi}_\nu$ are orthogonal.

Due to eq. 5.2.12 and the definition of $\boldsymbol{\varphi}_\nu$, $\boldsymbol{\varphi}_\nu^T \boldsymbol{\varphi}_\nu = \frac{1}{m}$. Thus

$$\sum_{\nu=1}^s \boldsymbol{\varphi}_\nu \boldsymbol{\varphi}_\nu^T \boldsymbol{\varphi}_i = \frac{\boldsymbol{\varphi}_i}{m} \quad (5.3.18)$$

This shows that each $\boldsymbol{\varphi}_i$ is an eigenvector of $\sum_{\nu=1}^s \boldsymbol{\varphi}_\nu \boldsymbol{\varphi}_\nu^T$. As the set of all $\boldsymbol{\varphi}_\nu$ is orthogonal and of rank s , it forms a complete set of the eigenvectors of $\sum_{\nu=1}^s \boldsymbol{\varphi}_\nu \boldsymbol{\varphi}_\nu^T$. Furthermore,

$$\left(\sum_{\nu=1}^s \boldsymbol{\varphi}_\nu \boldsymbol{\varphi}_\nu^T q_\nu \right) \boldsymbol{\varphi}_i = \frac{q_i}{m} \boldsymbol{\varphi}_i \quad (5.3.19)$$

Therefore, the values $\frac{q_i}{m}$ are the eigenvalues of $\sum_{\nu=1}^s \boldsymbol{\varphi}_\nu \boldsymbol{\varphi}_\nu^T q_\nu$. Since spectral norm of a matrix is its largest singular value, and the singular values of a Hermitian matrix are the absolute values of its eigenvalues,

$$\left\| \sum_{\nu=1}^s \boldsymbol{\varphi}_\nu \boldsymbol{\varphi}_\nu^T q_\nu \right\| = \max_{1 \leq i \leq s} \left| \frac{q_i}{m} \right| \quad (5.3.20)$$

From eq. 5.3.17,

$$\frac{\|\mathbf{y}_{\text{err}}\|}{\|\mathbf{y}_p\|} \leq \max_{1 \leq i \leq s} \left| \frac{q_i}{m} \right| \|\mathbf{K}_{\text{sp}}\| \quad (5.3.21)$$

Note that $\|\mathbf{K}_{\text{sp}}\| = m\|\mathbf{E}\|$ using eq. 5.3.5b

Using eq. 5.3.14, eq. 5.3.21 is rewritten as

$$\frac{\|\mathbf{y}_{\text{err}}\|}{\|\mathbf{y}_p\|} \leq \max_{1 \leq i \leq s} \left| \frac{\|\mathbf{E}\|}{(\sigma_\nu - \omega^2)} - \frac{\|\mathbf{E}\|}{(\sigma_\nu - \bar{\omega}^2)} \right| \quad (5.3.22)$$

The advantage of MDR over MDA is now clear: for $\bar{\omega}$ close to ω , the right-hand side of eq. 5.3.22 is almost zero. Therefore, the impact of eigenvalues of the residual system on the error of MDA is greatly diminished. This demonstrates the well-known property of dynamic reduction that error is minimized in the neighborhood of the input frequency ω .

5.4 Numerical Results and Discussions

The investigation into the impact of MVDs on the vibrational properties of SWCNTs involves analyses of many models of SWCNTs with varying length, chirality, and size of defect. For the sake of brevity, two representative examples are presented here. Further examples are provided as supplemental data, available online. The examples shown here were selected to illustrate the most extreme cases, in which the MDR and MDA results were the least similar. The first example is a (10,0) SWCNT, approximately 200Å in length, containing a four atom multi- vacancy (see Fig. 5.1). The chiral vector indicates that this is a ‘zigzag’ CNT with a diameter of 7.83Å. The second example is a (10,10) SWCNT, also with a length of 200Å, containing a two atom multi-vacancy (see Fig. 5.2). This ‘armchair’ CNT

has a diameter of 13.56\AA . The (10,0) CNT system contains 1916 atoms (5748 DOFs), while the (10,10) CNT system contains 3358 atoms (10074 DOFs). Each CNT model is subjected to simulated annealing and quenching to achieve the static equilibrium configuration around which the system is linearized to obtain mass and stiffness matrices. The two CNT models illustrate two distinct classes of defect. In the (10,0) case, the defect is large relative to the circumference of the nanotube and so is not able to fully ‘heal’, as illustrated in Fig. 5.1. In contrast, the vacancy in the (10,10) case ‘heals’ during annealing into an octagonal arrangement of carbon atoms, bounded by hexagonal and pentagonal rings.

To provide a comparison to an existing order reduction method, the MDR results presented here are compared to results of a reduced-order model of the same size generated using MDA. The natural frequencies and normal modes of the pristine and perturbed (10,0) CNT are calculated directly, and the first 100 frequencies are plotted in Fig. 5.3. Additionally, MDA and MDR are used to reduce the order of the model to 400 modes, and the first 100 frequencies of each of those reduced-order models are also plotted in Fig. 5.3. The frequency, ω , used for the MDR model, eq. 5.2.12, is 0. The errors in the predicted frequencies from both reduced-order models, relative to the frequencies of the full-order system with defects, are shown in Fig. 5.4. Note that the rigid body modes, which correspond to frequencies of zero, are excluded from these results as there are no errors in them (results for additional systems, not discussed here, are provided in Appendix D).

For the (10,10) CNT with defect, two frequencies (ω) are considered for the MDR model, eq. 5.2.12: 0 and 1.8 THz. 1.8 THz corresponds roughly to the frequency of the 50th mode of the perturbed system. As before, the size of the reduced-order model is 400 modes. The predicted natural frequencies for these two MDR models are shown in Fig. 5.5, along with the frequencies of the pristine, full-order perturbed, and MDA systems. The errors in frequencies by both MDR models, relative to those of the full-order perturbed model, are shown in Fig. 5.6.

The first point illustrated by Figs. 5.3-5.6 is that MDR is capable of accurately approx-

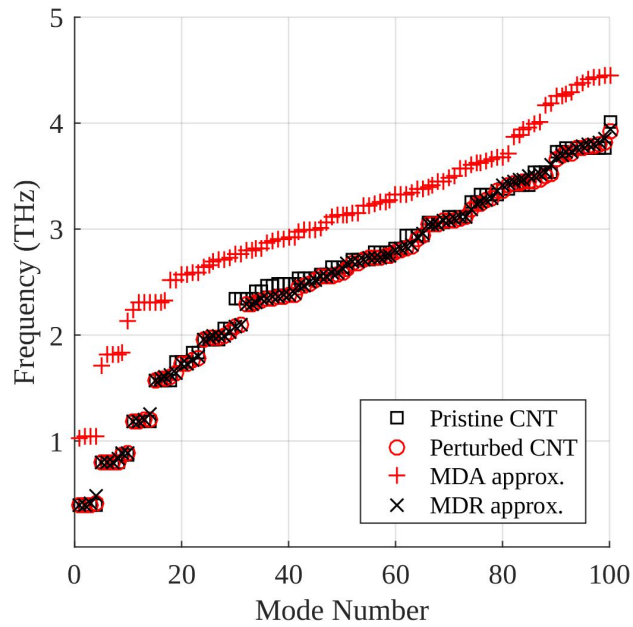


Figure 5.3: Natural frequencies of the pristine and perturbed (10, 0) CNT, with predicted frequencies found using MDA and MDR

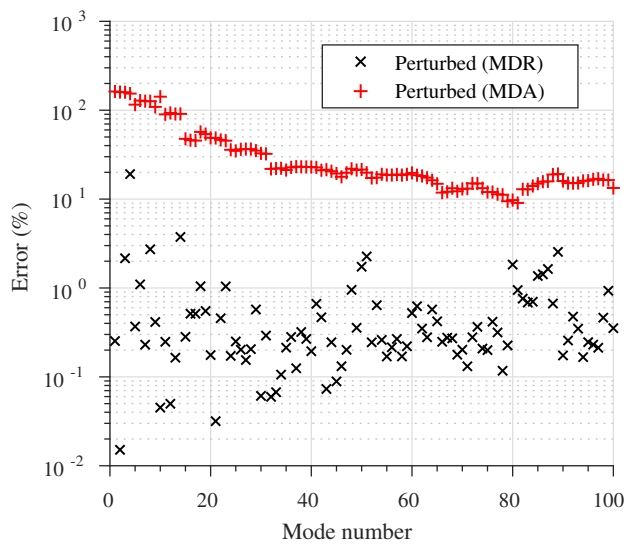


Figure 5.4: Errors in predicted natural frequencies of the (10,0) CNT

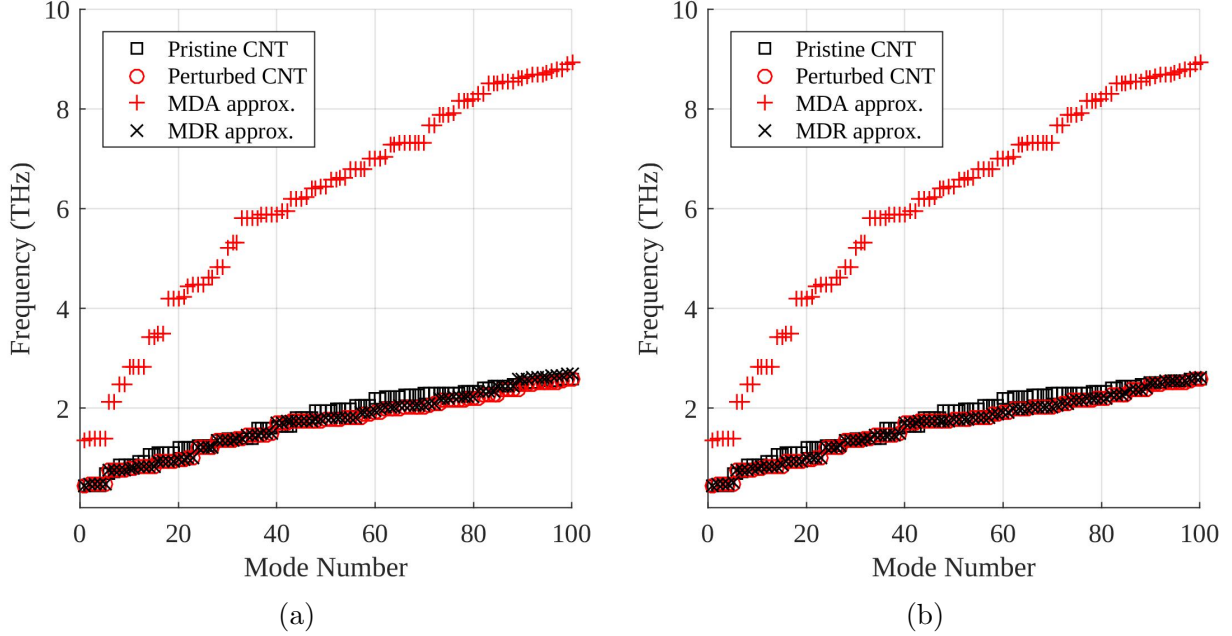


Figure 5.5: Natural frequencies of the pristine and perturbed (10,10) CNTs, with the frequencies predicted by MDA and a) MDR with $\omega = 0$ and b) MDR with $\omega = 1.8\text{THz}$

iminating the natural frequencies of both the (10,0) and (10,10) CNTs with vacancy defects. Also illustrated in these figures is the inability of MDA to match the results of the full-order perturbed system. For both CNTs, the frequencies predicted by MDA were greater than those of both the pristine and perturbed systems. However, for the (10,0) CNT, this deviation is slightly less pronounced. For the (10,10) CNT, which contains the ‘healed’ defect, the MDA frequency results differ wildly from calculated frequencies for the full-order system. In addition to further demonstrating the unsuitability of MDA for this type of problem, the results of the analysis of the (10,10) CNT show that, despite a smaller number of atoms removed, the ‘self-healed’ defect seems to provoke greater changes in the linearized system than the ‘unhealed’ defect.

The errors in the frequencies predicted by MDR for the (10,0) case (Fig. 5.4), show that, while not perfect, the reduced-order system is a close approximation of the full-order system. The highest error in the first 100 frequencies is on the order of 4%, with the majority of predicted frequencies within 1% of the true values. There is a clear trend of decreasing accuracy as the mode number increases, which is to be expected due to the dependence of

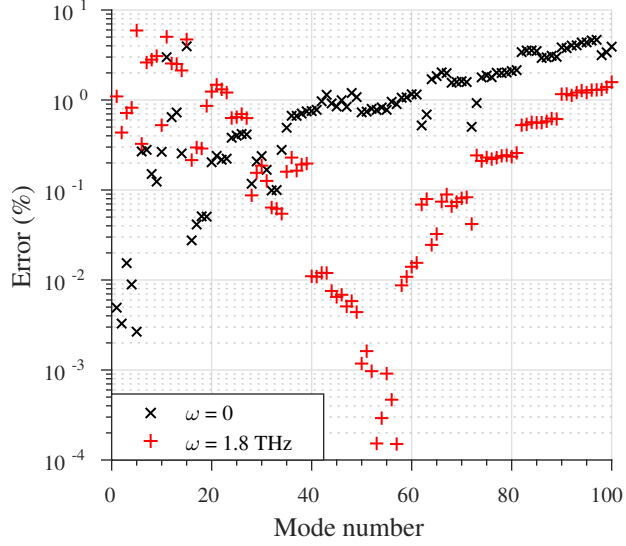


Figure 5.6: Errors in the natural frequencies of the (10,10) CNT predicted by MDR

the dynamic condensation technique on its input frequency, which in this case is 0. Similar trends are visible for the (10,10) case, Fig. 5.6, but are even more pronounced when the input frequency is shifted to 1.8 THz. As previously mentioned, the perturbed (10,10) CNT seems more significantly different from its pristine form than the (10,0) CNT due to the ‘self-healing’, which would naturally decrease the accuracy of an order reduction method based on the modes of the pristine system. This can be observed in Fig. 5.6, where some of the frequency errors can be seen to exceed 5% when the predicted frequency is sufficiently far from the input frequency. Close to the input frequencies, the error drops significantly, with errors below 0.1% observed for modes 40 to 70 when $\omega = 1.8$ THz.

In addition to the natural frequencies, the mode shapes predicted by the reduced-order model must be considered. In Fig. 5.7, the modal assurance criterion (MAC) values of the first 100 modes of the (10,0) defective CNT from MDR system relative to the first 100 modes of the full-order perturbed system are shown. The MAC of two modes is a measure of their similarity, with values ranging from 0, indicating that the two modes are orthogonal, to 1, meaning that the modes are identical [113]. Further details of the MAC calculation are given in Appendix C. Fig. 5.8 shows the MAC values of first 100 modes of the MDR reduced-order systems ($\omega = 0$ in Fig. 5.8a and $\omega = 1.8$ THz in Fig. 5.8b) relative to the full-order system



Figure 5.7: MAC values of the MDR reduced-order system versus the full-order perturbed system for the (10, 0) CNT

for the (10,10) CNT.

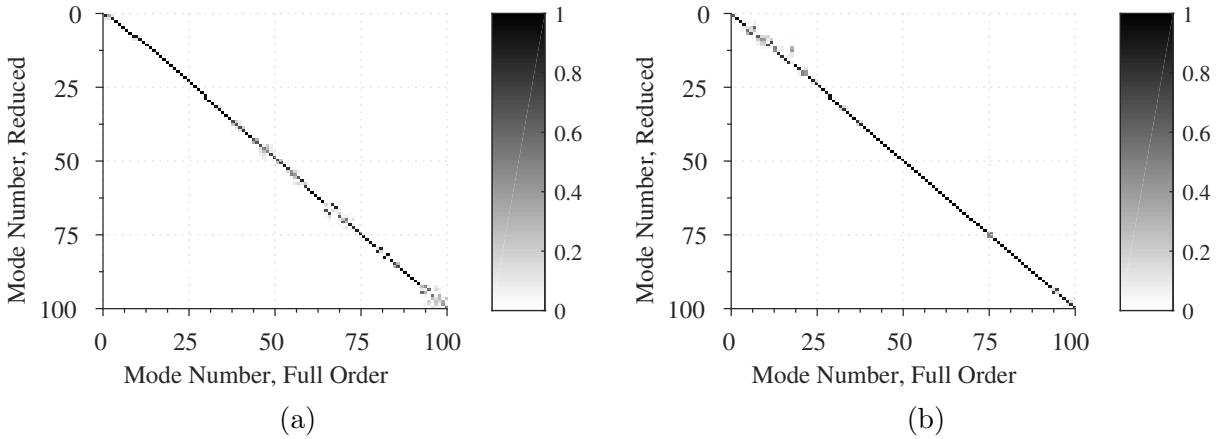


Figure 5.8: MAC values of the MDR reduced-order system versus the full-order perturbed system for the (10, 10) CNT, with a) an input frequency of 0 Hz b) an input frequency of 1.8 THz

The MAC plots, Figs. 5.7 and 5.8, indicate the quality of the MDR approximations. The MAC values of the first 100 modes of the reduced-order systems generated using MDR relative to the first 100 modes of the full-order pristine systems show that the MDR mode shapes are very similar to the full-order results. The majority of MDR modes shown match exactly one mode of the full-order system.

In addition to allowing the mode shape predicted by reduced-order models to be compared to the mode shapes of the full-order perturbed system, the MAC of the modes of the pristine

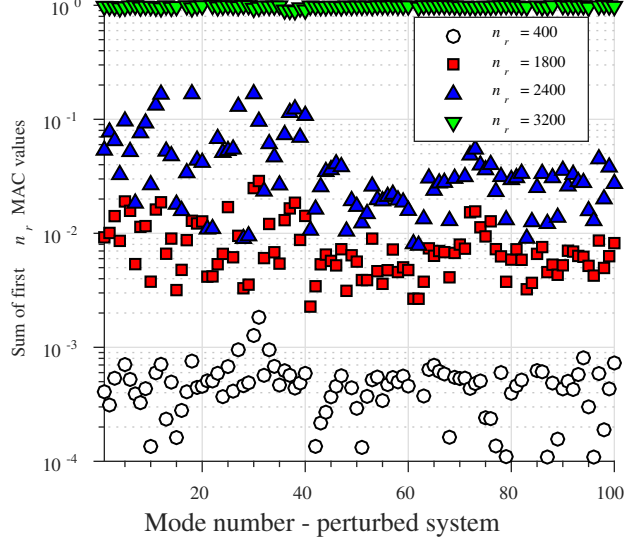


Figure 5.9: Sum of MAC values of the pristine system versus the full-order perturbed system for the (10, 0) CNT

system relative to the modes of the perturbed systems provide insight into the inability of MDA to accurately reduced the order of the perturbed systems. For MDA to successfully approximate a given mode of the perturbed system, that mode must be a linear combination of the modes used to construct Ψ in eq. 5.2.6. In other words, Ψ must be a basis for that mode. If this is the case, then the sum of the MAC values for that mode relative to each of the modes in Ψ will be 1 (see Appendix C). Consequently, the further that sum is from 1, the less accurate the MDA approximation of the mode will be. In Fig. 5.9, the sum of the MAC values of the first n_r modes of the (10,0) pristine system relative to the first 100 modes of the corresponding perturbed system are shown, with n_r varying from 400 (7% of the total number of modes of the system) to 3200 (55% of the total number of modes of the system). Note that the scale on the y-axis is logarithmic. Only for the $n_r = 3200$ case do the sum of the MAC values approach 1, showing that the modes of the perturbed system are not well approximated by a small number of modes of the pristine system.

To compare the efficiencies of MDR and MDA methods, both algorithms are implemented in MATLAB, and computational times are estimated as they reduce the order of the (10,10) CNT system to n_r modes and calculate the eigenvalues. The dimension of the reduced-

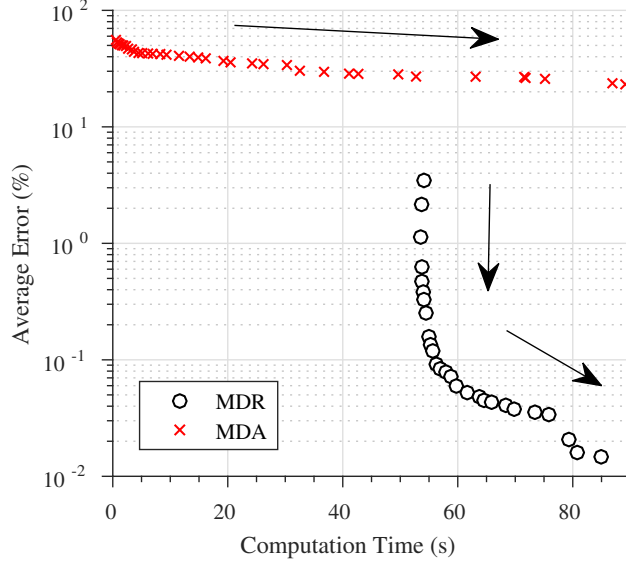


Figure 5.10: Average error of the first 100 natural frequencies of the (10,10) CNT versus computational times as the size of the reduced-order model is varied. Arrows indicate direction of increasing n_r

order model, n_r , is varied from 100 to 1500 for MDR, and from 100 to 2500 for MDA. The algorithms are run on a single core of an Intel Xenon E5-2650 v4 processor, with a clock speed of 2.2 GHz and 16GB of RAM. A single core is used to eliminate the effect of MATLAB's built-in multithreading capabilities on the results. The time to complete the calculation for each algorithm is plotted in Fig. 5.10, against the average error of the first 100 predicted modes. The results shown are an average of 15 trials for each algorithm and each reduced-order model.

The results of this efficiency test, illustrated in Fig. 5.10, show a clear advantage to using MDR. Even for a relatively large n_r , MDA struggles to approximate the frequencies of the (10,10) CNT system. MDR, on the other hand, though slower for a given reduced-order system size, n_r , can produce results that are up to three orders of magnitude more accurate. It should be noted from Fig. 5.10 that MDR has a minimum completion time because of matrix inversion required for computing $\mathbf{R}_D(\omega)$ – eq. 5.2.12b. As the order of reduced-order model, n_r , increases, the time required to compute the $\mathbf{R}_D(\omega)$ decreases since the size of the matrix to be inverted is smaller. At the same time, the solution of

the final eigenproblem becomes costlier. The reverse of this is also true — as n_r decreases, the time needed to perform the order reduction increases and the time required to solve the eigenproblem decreases. Therefore, unlike MDA, the computational time required for MDR does not approach zero as the number of modes decreases. The time required to compute the modes of the pristine system is not considered for these results, as it is small compared to the time required to complete the other steps and this computation can be completed once as a pre-processing step if several similar systems are to be considered.

5.5 Conclusion

Two SWCNT models are constructed, each with a different size of vacancy defect, and their equations of motion are linearized using a finite differences method, resulting in stiffness and mass matrices. To efficiently find a subset of their natural frequencies and normal modes, a new model order reduction technique (MDR) – a combination of modal domain analysis and dynamic condensation – is developed. Using this technique, these systems are analyzed and the results are compared to the full-order results and to the results found using the existing MDA order reduction technique. It is found that the new method, MDR, is capable of predicting the natural frequencies and normal modes of both linearized defect-bearing SWCNT systems with a high degree of accuracy. Furthermore, it is shown that these results cannot be duplicated with the use of MDA alone in a similar amount of time.

Chapter 6

Reduced-Order Modeling of Damping in Aluminum/Carbon Nanotube Composites

6.1 Introduction

It is mentioned in Chapter 3 that fiber-reinforced composites have the potential to supply the damping properties required for constructing, among other things, safe and reliable rotor blades. CNT reinforced composites are particularly promising for this type of application, as they show increased strength, stiffness, and resistance to softening at elevated temperature [43, 48], in addition to increased increased vibrational damping [49, 52, 127].

If CNT composites are to be used for structural and vibration damping components, considerable study will required to optimize the many parameters that go into developing the correct alloy and incorporating the appropriate CNTs in the right proportions to optimize the properties of these composites. From an experimental standpoint, this optimization process threatens to be unreasonably time consuming and expensive. In an effort to remove much of this expense, this chapter details and validates an accurate and efficient computational method of modeling the interaction between a defect-bearing CNT and a metallic matrix. Using this method, it will be possible to predict the impact of material choice and treatment of the CNT on the interfacial damping of the resulting composite.

Extensive work has been done on experimentally measuring the properties of CNTs embedded in resins [1, 3, 43, 54, 128], including their damping properties. However, resin based composites are limited by the nature of the polymers from which they are formed. A less well studied but nevertheless promising approach is to embed CNTs in metallic matrices [1, 46, 48, 49]. Specifically, aluminum is well-suited as a matrix material for CNT composites. These composites have demonstrated increased strength and an insensitivity to the annealing effects of extended exposure to high temperatures [48]. Experimental results regarding the damping properties of Al/CNT composites are limited, with the majority of studies on the subject focusing on the improvements in stiffness and yield strength that the addition of CNTs can produce [48, 129]. Those studies of damping in Al/CNT composites, much like similar studies for polymer/CNT composites, examine damping in terms of viscoelasticity [49, 54] — that is to say they are primarily concerned with storage and loss moduli. Though not inherently problematic, these measures of the mechanical response do not provide any information concerning the energy loss of the system as a function of displacement if the system is non-linear.

Computational studies of the damping of Al/CNT are similarly rare in comparison to those that examine damping in polymer/CNT composites. However, when the complex structure of the polymers is simplified and treated as a continuum, the methods and results of these studies can be used as points of comparison for Al/CNT simulations [57, 58]. Furthermore, the results of many studies of Al/CNT composites that do not specifically deal with damping reveal much about interfacial slip in these composites [130–132]. The insight that is provided by existing studies into the interfacial behavior of CNT composites is limited, however, as they exclusively consider pristine carbon nanotubes — that is to say carbon nanotubes that are free from defects. The assumption is particularly limiting as it is well known that disorder is inevitable and contributes to lubricity at the atomic level [133, 134].

The following sections detail two order reduction methods that permit large Al/CNT systems with Stone-Wales or multi-vacancy defects to be simulated accurately and efficiently.

The first method is the application of Guyan, or static, reduction to the aluminum matrix. Guyan reduction permits those atoms which do not interact with the CNT and are not subject to outside forces to be removed from the simulation without any loss of accuracy. The second method models the behavior of the defect-bearing CNT using a subset of its normal modes, which can be found using the methods discussed in the preceding chapters. Combined, these methods greatly decrease the number of degrees of freedom to be considered when simulating the Al/CNT system, resulting in a considerable increase in computational efficiency. These methods are then employed to examine the damping of blocks of Al/CNT composite with various defects subjected to a periodic displacement field as a function of displacement amplitude.

6.2 Methods

6.2.1 Overview

Molecular dynamics simulations are generally unsuitable for analyzing the behavior of systems subjected to low-frequency excitation. This limitation is due to the short time steps (on the order of 1 fs) that are required to ensure that the numerical integration to determine an atom's position and momentum is numerically stable and can accurately describe the thermal vibrations of individual atoms [95]. These short time steps mean that the number of calculations, and therefore the computational resources, required to simulate the behavior of a system even on a microsecond timescale can often be prohibitive. To investigate the damping in Al/CNT composites it is necessary to simulate several cycles of a low-frequency excitation, which would require a timescale on the order of milliseconds or even seconds. This is achieved by treating the system as quasi-static — that is to say, assuming that the thermal vibration of individual atoms will not have a measurable impact on the macroscale dynamics of the system. The assumption is experimentally confirmed by [49], where it is shown that the elastic and damping properties of an Al/CNT composite remain constant

while temperature is varied from 25°C to 200°C. In practice this means taking the total time that is to be simulated, dividing it into relatively large time steps, and treating the behavior of the system at each time step as a molecular statics problem. In addition to neglecting thermal effects, this quasi-static approach assumes that the frequency of excitation does not alter the elastic and damping properties of the composite. This assumption is supported by [49] and [135]. Both these studies show that varying the frequency at which a CNT composite is excited (over a range of frequencies that spanned from 0.5 Hz to 30 Hz) does not change its measured elastic or damping properties. Therefore, a quasi-static simulation can be expected to accurately predict the damping and elastic properties of an Al/CNT composite experiencing low frequency excitation.

The method used here to simulate the behavior of a metallic composite containing single-walled carbon nanotubes requires a number of separate processes. To clarify the purpose of each process and illustrate how they work together to form the simulation, they will be described briefly here before being detailed in full. In broad terms, the purpose of this simulation is to take a CNT embedded in a block of aluminum, apply a known force to certain atoms in the aluminum matrix, and determine the positions of the atoms in the system that minimize the net force on each atom. From this, the displacements of the atoms subjected to external forces can be extracted. The resulting data is analogous to the force-displacement data typically measured for macroscale dampers.

The simulation can be broken down into four parts: the geometry of the system, the elastic interactions, the Lennard-Jones interactions, and what will be referred to here as the simulation ‘solver’ (see Fig. 6.1). The geometry of the system refers to the initial position of the atoms in both the CNT and the matrix, and to the order reduction methods that permit the full-order system to be converted into reduced-order coordinates. The elastic interaction refers to the interatomic interactions between atoms in the same part of the system (between atoms in the CNT, for example). A critical assumption used in the order-reduction methods is that the displacement of atoms in a given part of the system is sufficiently small that

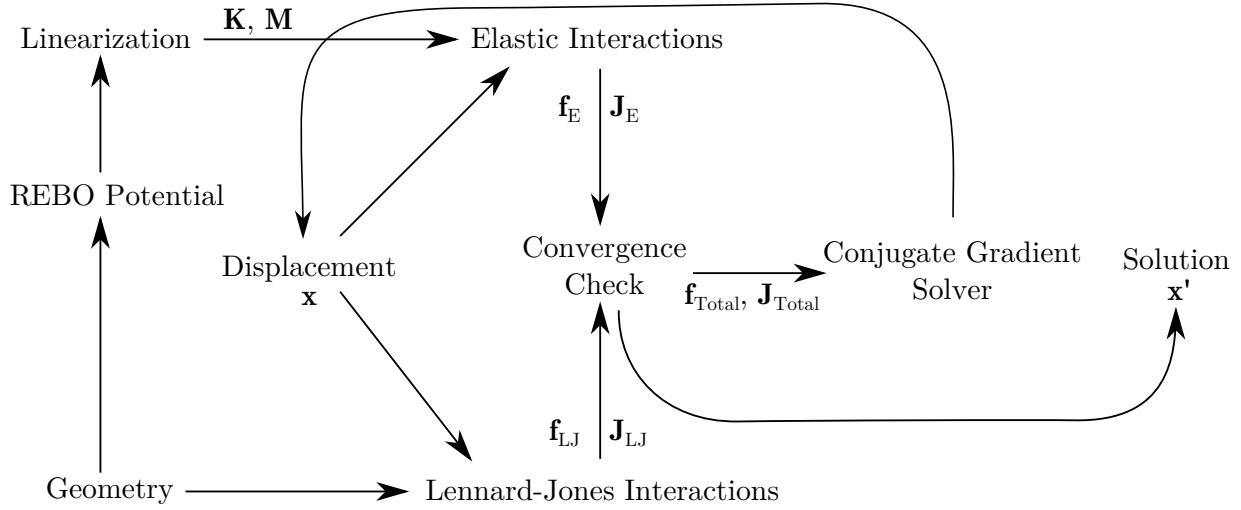


Figure 6.1: Flowchart of the solution procedure

the internal forces on those atoms are linearly proportional to displacement. That allows the interatomic interactions within a given part to be condensed into a stiffness matrix. The interaction between atoms in the CNT and the aluminum matrix is modeled using the Lennard-Jones potential. As the CNT is permitted to slip relative to the matrix, it is crucial to the accuracy of this simulation that the force between an atom in the CNT and an atom in the matrix be modeled using a more comprehensive, nonlinear relationship.

In order to simulate the response of the composite to cyclic loading, a force is applied to the model and the resulting displacement must be calculated. This process is referred to here as ‘solving’ the simulation, though more generally it is an extension of the energy minimization process. This solution is achieved using the conjugate gradient method. A flowchart depicting the interactions among these various processes is provided in Fig. 6.1.

6.2.2 Simulation Geometry

The simulation consists of two parts, the CNT and the aluminum matrix. The aluminum matrix fills the majority of the simulation box, with a void running parallel to the z-direction to accommodate the CNT (see Fig. 6.2). Elemental aluminum forms a face-centered cubic

lattice, and its unit cell has an edge length of approximately 4.05\AA [111]. These parameters are used to generate a block of aluminum the size of the simulation box ($39.14\text{\AA} \times 39.14\text{\AA} \times 204.48\text{\AA}$) using LAMMPS. To allow the CNT to be embedded in this block, a cylindrical void is created in the center, aligned with the z-axis. Calculating the radius of this void that minimizes residual stress when the CNT is added to the simulation is not trivial. While it is relatively simple to find the equilibrium distance between an isolated pair of carbon and aluminum atoms, each carbon atom in the simulation interacts with many aluminum atoms, and vice-versa. To find the optimum radius of the void, the size of the void is first set equal to the diameter of the CNT. The aluminum block and the CNT are both imported into the simulation, and the potential energy is calculated. Then, the radius of the void is increased, and the process is repeated until a local minimum of potential energy is found. Note that, because the aluminum matrix is highly ordered and the positions of the atoms in it are inherently discrete, the number of possible void diameters is both discrete and relatively small.

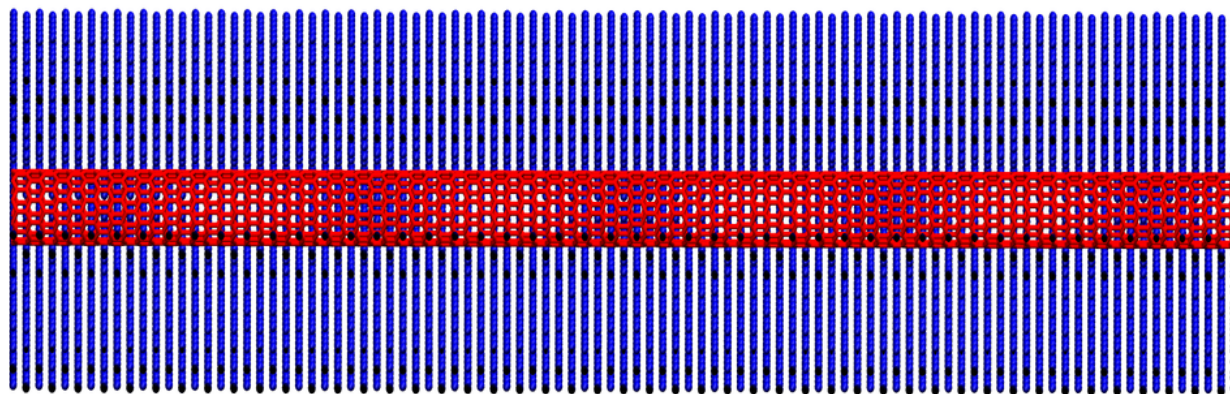


Figure 6.2: Example of the composite geometry, rendered in VMD [112]. Carbon-carbon bonds are red and aluminum atoms are shown in blue.

With the void in place, the aluminum block undergoes simulated annealing and energy minimization as described in Chapter 4. It is critical that the CNT and the aluminum

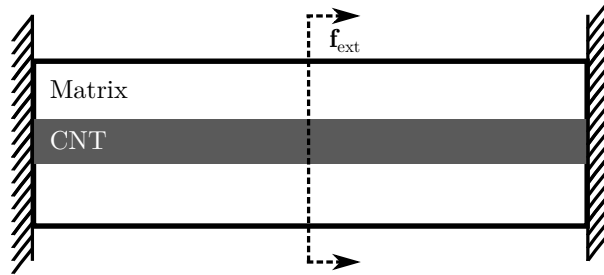


Figure 6.3: A schematic representation of the loading applied to a unit cell of the composite simulation. The hatching at the ends of the block of composite material indicate that the atoms on those planes are prevented from moving parallel to the CNT.

matrix are energy minimized independently, as they will be linearized independently and linearization must take place about an equilibrium position. The same process that is used to linearize the CNT model is used to linearize the model of the aluminum block.

To observe the dynamic response of the system, external forces are applied to it at a given frequency. The simulation box used here has periodic boundary conditions, and so the material inside the simulation box acts as if it is part of an infinitely large solid comprised only of blocks of atoms arranged and moving in precisely the same way as those in the simulation box. This requires that care be taken when applying external forces to the system to ensure that the resulting movement of the system is both mathematically admissible and has physical meaning. To satisfy both these stipulations, the following conditions were applied to the aluminum matrix: first, the aluminum atoms lying on a plane orthonormal to the longitudinal axis of the CNT have their displacement constrained (i.e. removed from the subsequent calculations) in the z -direction (parallel to the longitudinal axis of the CNT); then aluminum atoms on a parallel plane, half the length of the unit cell away from the first plane in the z -direction (104.24\AA) have an external force applied to them in the z -direction. The first plane (corresponding to the constrained atoms) is necessary to ensure that the system does not merely slide an arbitrary distance in the z -direction when a force is applied. This is illustrated in Fig. 6.3.

The CNTs used in this analysis have a chiral vector of $(10, 0)$ and span the simulation

box in the z-direction. The arrangement of atoms in a CNT with and without defects has been dealt with at length in preceding chapters of this thesis, and so will not be repeated here. However, comment must be made on the reduced-order models used. In previous chapters, the aim of order reduction has been to permit the efficient calculation of the free vibrational response of defect-bearing CNTs. However, because an external force is applied, it is the forced response of the CNT that is of interest. It is a well-known property of linear elastic systems that the spatial component of their forced response can be constructed from a linear combination of their mode shapes (the spatial component of their free response) [68]. Furthermore, if the forced response can be accurately represented by a small subset of the modes of a system, that subset can be used to construct a reduced-order model that is capable of accurately predicting the response of that system to a particular forcing function [119].

Finding the modes of the CNT system that correspond to the behavior of a CNT embedded in an aluminum matrix subject to an external load requires the behavior of the full-order system under similar loading conditions to be calculated. Then the most active modes are extracted. The degree of involvement of each mode is here determined using the modal assurance criterion (MAC). The modes with the highest involvement (defined here as having a MAC values that sum to at least 0.9) are retained in the reduced-order model, while the remaining modes are neglected.

The model of the aluminum matrix must be considered differently from the model of the CNT, because unlike the CNT there are atoms in the aluminum matrix that experience neither an external force (from the loading on the system) nor an interaction force from the CNT (due to the Lennard-Jones forces). As the simulation is quasi-static, it can be assumed that all the time derivatives of the displacement vector are zero. The result of this is that the atoms comprising the matrix (and by extension the degrees of freedom associated with them) can be subdivided into two groups: the primary atoms (and degrees of freedom) — those which experience forces other than internal interactions within the matrix, and secondary atoms (degrees of freedom) that do not experience outside forces. When divided in this way,

the static response of the matrix can be determined without loss of accuracy by considering only the primary degrees of freedom. This method, outlined below, is referred to in the literature as Guyan or static reduction [119, 136].

Guyan Reduction

Consider the following linear system

$$\mathbf{f} = \mathbf{K}\mathbf{x} \quad (6.2.1)$$

where \mathbf{f} is the force vector acting on the system, \mathbf{K} is the stiffness matrix, and \mathbf{x} is the displacement vector. Let \mathbf{x} be divided into primary and secondary degrees of freedom, such that the degrees of freedom not subjected to outside forces are classified as secondary degrees of freedom, and all the rest are primary degrees of freedom. Without any loss of generality, let the primary degrees of freedom appear first in the force vector. This allows \mathbf{f} to be written

$$\mathbf{f} = \begin{bmatrix} \mathbf{f}_p \\ \mathbf{0} \end{bmatrix} \quad (6.2.2)$$

If this method of partitioning is extended to the rest of the system, eq. 6.2.1 can be rewritten as

$$\begin{bmatrix} \mathbf{f}_p \\ \mathbf{0} \end{bmatrix} = \begin{bmatrix} \mathbf{K}_{pp} & \mathbf{K}_{ps} \\ \mathbf{K}_{ps} & \mathbf{K}_{ss} \end{bmatrix} \begin{bmatrix} \mathbf{x}_p \\ \mathbf{x}_s \end{bmatrix} \quad (6.2.3)$$

Separating the above into equations for the force on the primary degrees of freedom and the secondary degrees of freedom results in

$$\mathbf{f}_p = \mathbf{K}_{pp}\mathbf{x}_p + \mathbf{K}_{ps}\mathbf{x}_s \quad (6.2.4a)$$

$$\mathbf{0} = \mathbf{K}_{sp}\mathbf{x}_p + \mathbf{K}_{ss}\mathbf{x}_s \quad (6.2.4b)$$

This allows the displacement of the secondary degrees of freedom to be written in terms of the displacement of the primary degrees of freedom, thus

$$\mathbf{x}_s = -\mathbf{K}_{ss}^{-1}\mathbf{K}_{sp}\mathbf{x}_p \quad (6.2.5)$$

Substituting eq. 6.2.5 into eq. 6.2.4a allows the relationship between the external forces on the primary degrees of freedom and their corresponding displacements to be expressed without requiring the explicit calculation of the displacements of the secondary degrees of freedom, as follows

$$\mathbf{f}_p = (\mathbf{K}_{pp} - \mathbf{K}_{ps}\mathbf{K}_{ss}^{-1}\mathbf{K}_{sp}) \mathbf{x}_p \quad (6.2.6)$$

Unless it can be guaranteed that there is no external force on the secondary degrees of freedom and the system is at rest, Guyan reduction is an approximation. However, as this is a quasi-static simulation and the secondary degrees of freedom are chosen specifically because they are not subject to outside forces, Guyan reduction on the aluminum matrix results in no loss of accuracy.

6.2.3 Elastic Interactions

The elastic interactions between atoms in a given part of the simulation (either the CNT or the matrix) are determined by linearizing the interaction forces for that part. As before, this is done by calculating the second partial derivatives of the interaction potential and assembling them into a stiffness matrix. Then, the interatomic forces within that part of the system can be calculated by right-multiplying the stiffness matrix by the displacement vector. Additionally, the Jacobian of the force vector is simply the stiffness matrix. For the CNTs, the REBO potential [101] using the parameters derived by Lindsay and Broido [98]

are used. For the aluminum matrix, the potential is defined using the embedded atom method (EAM) [137], after Silvestre *et al.* [131], with the parameters developed by Mishin *et al.* [138].

6.2.4 Lennard-Jones Interactions

As previously mentioned, the interaction between the CNT and the aluminum matrix cannot be modeled using a linearized interaction because of the possibility that the CNT will slip relative to the matrix, and slipping violates the small displacements assumption that is vital to linearized models. Instead, the Lennard-Jones potential is used to model this interaction. This is implemented using an extended version of the LAMMPS software package, which permitted the calculation of not only the forces involved, but also the Jacobian of the forces.

Defining the Lennard-Jones Potential

Consider a system of n unbonded and uncharged atoms, acted upon only by van der Waals forces ¹. In such a system, two atoms at a sufficient distance from each other will experience an attractive interatomic force, due to transient spontaneous polarization (London forces). Though the magnitude of the London forces increases as interatomic distance decreases, at a certain distance a repulsive force, a result of the Pauli exclusion principle, begins to dominate. The Lennard-Jones potential is a simple function of interatomic distance that seeks to model this behavior [139]. For two atoms, separated by a distance r , the Lennard-Jones potential energy can be expressed

$$T_{LJ} = 4\epsilon \left[\left(\frac{\sigma}{r} \right)^{12} - \left(\frac{\sigma}{r} \right)^6 \right] \quad (6.2.7)$$

¹This is the classic system for which the Lennard-Jones potential was derived. The Lennard-Jones potential is, however, frequently used to approximate the long-range interactions of unbonded atoms in more complex systems. In such cases, it appears in conjunction with additional terms to describe the potential energy of the system due to short-range interactions, eg. [102].

where ϵ and σ are constants — specific to the elements involved — with units of energy and distance, respectively. The magnitude of the interatomic force due to this potential is

$$f_{LJ} = 24\epsilon \left(\frac{-2\sigma^{12}}{r^{13}} + \frac{\sigma^6}{r^7} \right) \quad (6.2.8)$$

The force predicted by the Lennard-Jones potential will here on be referred to as the Lennard-Jones force.

Though the definition is not overtly cumbersome, the summation of the Lennard-Jones potential over a system of n atoms, with positions expressed as a single column vector, \mathbf{u} , quickly becomes unwieldy. To mitigate this, the notation $\mathbf{z}^{(a)}$ is used to indicate the 3×1 vector composed of those values of \mathbf{z} which relate to the atom a — e.g. $\mathbf{u}^{(a)}$ denotes the position vector of atom a . Similarly, $z_i^{(a)}$ is used to indicate the i^{th} component of vector $\mathbf{z}^{(a)}$.

The net force on atom a of this n -atom system is

$$\mathbf{f}^{(a)} = \sum_{b=1, b \neq a}^n \left[24\epsilon \left(\frac{-2\sigma^{12}}{|\mathbf{u}^{(a)} - \mathbf{u}^{(b)}|^{13}} + \frac{\sigma^6}{|\mathbf{u}^{(a)} - \mathbf{u}^{(b)}|^7} \right) \right] \frac{\mathbf{u}^{(a)} - \mathbf{u}^{(b)}}{|\mathbf{u}^{(a)} - \mathbf{u}^{(b)}|} \quad (6.2.9)$$

Written out in full, the i^{th} component of $\mathbf{f}^{(a)}$ is

$$f_i^{(a)} = \sum_{b=1, b \neq a}^n \alpha^{(a,b)} \left(u_i^{(a)} - u_i^{(b)} \right) \quad (6.2.10)$$

where

$$\alpha^{(a,b)} = 24\epsilon \left(\frac{-2\sigma^{12}}{\left[\sum_{k=1}^3 \left(u_k^{(a)} - u_k^{(b)} \right)^2 \right]^{\frac{7}{2}}} + \frac{\sigma^6}{\left[\sum_{k=1}^3 \left(u_k^{(a)} - u_k^{(b)} \right)^2 \right]^{\frac{4}{2}}} \right) \quad (6.2.11)$$

The Jacobian of the Lennard-Jones Force

For the purposes of dynamic simulations, the expression for the Lennard-Jones force given in eq. 6.2.9 can be used as it stands. However, if an equilibrium position of the atoms in the system is required², it is beneficial to derive an expression for the Jacobian of the force vector, \mathbf{f} , relative to the position vector, \mathbf{u} , of this system. Note that this is equivalent to the Jacobian of force relative to displacement, as a change in position implies the same change in displacement.

In keeping with the notation introduced in the previous section, the components of the Jacobian, \mathbf{J} will be written as

$$J_{i,j}^{(a,b)} = \frac{\partial f_i^{(a)}}{\partial u_j^{(b)}} \quad (6.2.12)$$

Substituting eq. 6.2.10 into eq. 6.2.12

$$J_{i,j}^{(a,b)} = \frac{\partial \alpha^{(a,b)}}{\partial u_j^{(b)}} \left(u_i^{(a)} - u_i^{(b)} \right) - \alpha^{(a,b)} \delta_{ij}, \quad (a \neq b) \quad (6.2.13a)$$

$$J_{i,j}^{(a,a)} = \sum_{b=1, b \neq a}^n \left[-\frac{\partial \alpha^{(a,b)}}{\partial u_j^{(b)}} \left(u_i^{(a)} - u_i^{(b)} \right) + \alpha^{(a,b)} \delta_{ij} \right] \quad (6.2.13b)$$

where

$$\frac{\partial \alpha^{(a,b)}}{\partial u_j^{(b)}} = 24\epsilon \left(\frac{28\sigma^{12} \left(u_j^{(a)} - u_j^{(b)} \right)}{\left[\sum_{k=1}^3 \left(u_k^{(a)} - u_k^{(b)} \right)^2 \right]^8} - \frac{8\sigma^6 \left(u_j^{(a)} - u_j^{(b)} \right)}{\left[\sum_{k=1}^3 \left(u_k^{(a)} - u_k^{(b)} \right)^2 \right]^5} \right) \quad (6.2.14)$$

²For the system described in §6.2.4 — which most closely corresponds to a noble gas at relatively low pressure — an equilibrium position of the atoms has no physical relevance other than to act as a low energy starting point for a molecular dynamics simulation. When the Lennard-Jones potential is used in conjunction with other force fields to describe the behavior of a solid or system of solids, equilibria become both more significant and more challenging to compute.

6.2.5 Solving Constrained Equations of Motion Using the Conjugate Gradient Method

The problem which must be solved at every force step of the quasi-static simulation is, in full-order coordinates

$$\mathbf{f}_{LJ}(\mathbf{x}) + \mathbf{K}\mathbf{x} + \mathbf{f}_{\text{ext}} = \mathbf{0} \quad (6.2.15)$$

where \mathbf{x} is the position vector, $\mathbf{f}_{LJ}(\mathbf{x})$ is the force on each atom due to the Lennard-Jones potential, \mathbf{K} is the stiffness matrix of the system³, and \mathbf{f}_{ext} is the external force on the system. In reduced-order coordinates, this is

$$\mathbf{T}^T \mathbf{f}_{LJ}(\mathbf{T}\mathbf{y}) + \mathbf{T}^T \mathbf{K} \mathbf{T} \mathbf{y} + \mathbf{T}^T \mathbf{f}_{\text{ext}} = \mathbf{0} \quad (6.2.16)$$

where \mathbf{T} is the order reduction matrix. Let \mathbf{f}_{NET} equal the left-hand side of eq. 6.2.16. Then, the condition in eq. 6.2.16 is also satisfied by

$$\|\mathbf{f}_{\text{NET}}\|^2 = 0 \quad (6.2.17)$$

where $\|\cdot\|$ indicates the 2-norm of a vector. Solving eq. 6.2.17 is simpler than solving eq. 6.2.16 for two reasons: first, it is a scalar valued equation, so solving it requires only one algebraic equation to be solved, regardless of how many degrees of freedom are present in the system; second, the expression $\|\mathbf{f}_{\text{NET}}\|^2$ is greater than or equal to zero for any physically admissible forces (complex-valued forces having no meaning in this context), and so the solving eq. 6.2.16 is equivalent to minimizing the left-hand side of eq. 6.2.17.

Minimizing $\|\mathbf{f}_{\text{NET}}\|^2$ is here achieved using the conjugate gradient method. The conjugate

³Previously the stiffness matrices of the individual parts of the system have been used. If the displacement vector is defined such that $\mathbf{x} = [\mathbf{x}_{\text{CNT}}^T \ \mathbf{x}_{\text{M}}^T]^T$, then the stiffness matrix of the system can be written

$$\mathbf{K} = \begin{bmatrix} \mathbf{K}_{\text{CNT}} & \mathbf{0} \\ \mathbf{0} & \mathbf{K}_{\text{M}} \end{bmatrix}$$

gradient method is an iterative process for determining a local minimum of some objective function. [140] Each iteration begins with an initial point at which the function and its derivative (or, in the multi-dimensional case, its Jacobian) is evaluated. Then, using the derivative and information concerning the direction of the previous step, a new direction is found in which the function is believed to be decreasing. A line search algorithm is used to find a point in the given direction that decreases the value of the objective function sufficiently (what constitutes a sufficient decrease will be discussed later). This process is repeated until a convergence condition is satisfied (typically defined by a minimum value of the objective function or a minimum slope) [141]. In this case, the convergence condition is that $\|\mathbf{f}_{\text{NET}}\|^2 \leq 0.25 \text{ eV}^2/\text{\AA}^2$.

As the first step of the conjugate gradient method has no previous step for reference, it uses only the Jacobian to determine in which direction the next point to be evaluated will lie. Therefore, this step is identical to a step in the method of steepest decent. An initial point is specified by the user and the Jacobian of the function to be minimized is evaluated. Here, the Jacobian \mathbf{J}_{NET} is

$$\mathbf{J}_{\text{NET}} = \nabla (\|\mathbf{f}_{\text{NET}}\|^2) = \left[\frac{\partial}{\partial \mathbf{y}_1} \|\mathbf{f}_{\text{NET}}\|^2 \quad \dots \quad \frac{\partial}{\partial \mathbf{y}_n} \|\mathbf{f}_{\text{NET}}\|^2 \right] \quad (6.2.18a)$$

$$\frac{\partial}{\partial \mathbf{y}_i} \|\mathbf{f}_{\text{NET}}\|^2 = 2 \sum_{j=1}^n \mathbf{f}_{\text{NET}j} \frac{\partial \mathbf{f}_{\text{NET}j}}{\partial \mathbf{y}_i} \quad (6.2.18b)$$

The Jacobian indicates the direction in which the function is increasing at the largest rate (at the given point), therefore a new point displaced from the initial point by an infinitesimal distance in the direction of the negative of the Jacobian will have a lower net force on it than in its previous position. This assumes, of course, that the net force and its derivatives are continuous with respect to position. The specific point that will be chosen using a line search, a process that will be detailed later. For each subsequent step, the direction that is

searched for the next point is found using the general formula

$$\mathbf{d}_n = -\nabla f(\mathbf{y}_n) + \beta_n \mathbf{d}_{n-1} \quad (6.2.19)$$

where \mathbf{d}_n is the direction that is to be searched in the n^{th} step, \mathbf{y}_n is the point evaluated in the n^{th} step, and β_n is defined (after Fletcher and Reeves [141])

$$\beta_n := \frac{\nabla f(\mathbf{y}_n)^{\text{T}} \nabla f(\mathbf{y}_n)}{\nabla f(\mathbf{y}_{n-1})^{\text{T}} \nabla f(\mathbf{y}_{n-1})} \quad (6.2.20)$$

In this particular case, $f(\mathbf{y}_n) = \|\mathbf{f}_{\text{NET}}\|^2$.

Line Search

For each step, the conjugate gradient method provides a direction in which the function is decreasing. However, to find the next point at which the algorithm is to be applied, a line search must be conducted in the direction specified to determine the location of a point that decreases the objective function. Ideally, this search would find the point that minimizes the objective function in the given direction. However, such a search would be extremely time consuming and is not necessary for the conjugate gradient method. [140] An alternative approach is to employ the Armijo rule to specify the maximum acceptable value of the objective function in the given direction. If $f(\mathbf{y})$ is the objective function, \mathbf{d} is the direction which is being searched, and α is the distance from the current point to the proposed next point in the direction \mathbf{d} , the Armijo rule can be written [142]

$$f(\mathbf{y} + \alpha \mathbf{d}) \leq f(\mathbf{y}) + c\alpha \mathbf{d}^{\text{T}} \nabla f(\mathbf{y}) \quad (6.2.21)$$

where c is a parameter chosen by the user to control how much weight is given to the derivative of the objective function at a proposed point. For the simulation described here, a value $c = 10^{-4}$ is chosen. Stricter criteria exist for assessing the validity of a proposed

point in a line search, including the curvature rule and the Wolfe search condition [143,144], however in this case these proved to be superfluous.

To determine the values of α that are to be tested using the above condition, a simple algorithm is employed. Let m be the maximum step distance (the distance used in this simulation is 0.01\AA — it was determined that excessively large steps ultimately hindered the convergence of the algorithm). Then, a trial step distance α_i can be found

$$\alpha_i = a^{-(b+i)} \quad i = 0, 1, \dots \quad (6.2.22a)$$

$$b = -\frac{1}{2} \log_a \left(\frac{m^2}{|\mathbf{d}|^2} \right) \quad (6.2.22b)$$

For this simulation, a is chosen to be 10. i is increased until eq. 6.2.21 is satisfied. The resulting point is used for the next step of the conjugate gradient solver.

Improving Solver Efficiency

The conjugate gradient method requires that the Jacobian of the objective function be evaluated at every step. In the simulation of a CNT embedded in a metallic matrix, the objective function, $|\mathbf{f}_{\text{NET}}|^2$ can be broken down as follows (noting that the external force on the system is constant with respect to displacement)

$$\frac{\partial}{\partial \mathbf{y}_i} \|\mathbf{f}_{\text{NET}}\|^2 = \frac{\partial}{\partial \mathbf{y}_i} (\mathbf{f}_{\text{NET}}^T \mathbf{f}_{\text{NET}}) = 2\mathbf{f}_{\text{NET}}^T \frac{\partial}{\partial \mathbf{y}_i} \mathbf{f}_{\text{NET}} \quad (6.2.23a)$$

$$\frac{\partial}{\partial \mathbf{y}_i} \mathbf{f}_{\text{NET}} = \nabla_{\mathbf{x}} \mathbf{f}_{\text{NET}} \frac{\partial \mathbf{x}}{\partial \mathbf{y}_i} = \nabla_{\mathbf{x}} \mathbf{f}_{\text{NET}} \mathbf{T}_i \quad (6.2.23b)$$

where \mathbf{T}_i indicates the i^{th} column of \mathbf{T}

$$\frac{\partial}{\partial \mathbf{y}_i} \|\mathbf{f}_{\text{NET}}\|^2 = 2\mathbf{f}_{\text{NET}}^T \nabla_{\mathbf{x}} \mathbf{f}_{\text{NET}} \mathbf{T}_i \quad (6.2.23c)$$

$$\frac{\partial}{\partial \mathbf{y}_i} \|\mathbf{f}_{\text{NET}}\|^2 = 2(\mathbf{f}_{\text{E}} + \mathbf{f}_{\text{LJ}} + \mathbf{f}_{\text{ext}})^T \mathbf{T} \mathbf{T}^T (\nabla_{\mathbf{x}} \mathbf{f}_{\text{E}} + \nabla_{\mathbf{x}} \mathbf{f}_{\text{LJ}}) \mathbf{T}_i \quad (6.2.23d)$$

The gradient of the elastic force ($\nabla_{\mathbf{x}}\mathbf{f}_E$) is simply the stiffness matrix, and so poses no difficulties. Evaluating the gradient of the Lennard-Jones force, on the other hand, requires significant computational time. In an effort to increase the speed at which the solver converges to a solution, the gradient of the Lennard-Jones force is only evaluated every 20 steps. For the steps between evaluations of $\nabla_{\mathbf{x}}\mathbf{f}_{LJ}$, the Jacobian of the objective function is approximated as constant. In doing this, the Lennard-Jones interactions are briefly treated as being linearly elastic. This approximation is only valid for small displacements, a stipulation that further motivates the maximum step size included in the line search algorithm.

6.3 Results

The results presented here have two purposes: firstly, they are shown to illustrate the validity of the novel computational method of simulating the dynamics of atomic systems described in the preceding section; secondly, as this technique allows the impact of atomic-scale defects on the damping of nanocomposite materials to be predicted numerically, these results help elucidate the significance of defects on interfacial slip. A model, such as the one presented here, is only meaningful if it is able to match experimentally observed results. To that end, it is crucial that the numerical results are validated with respect to experimental results. The model used here, while incorporating certain aspects of the atomic-scale complexity of nanocomposites, relies on two assumptions concerning the geometry of the system and the manner in which forces are applied to it which must be addressed before the results themselves can be understood in the proper context.

The first assumption that must be considered is that the simulation assumes that each nanotube is aligned with the direction of loading. As the bending stiffness of a CNT is small compared to its tensile stiffness [2], this alignment maximizes the impact of the nanotubes on the response of the system. The model used here contains 1800 carbon atoms (vacancy defects notwithstanding) and 15936 aluminum atoms. Based on molar masses of 12.0107 g/mol

and 26.9815 g/mol respectively [111], this suggests that the simulated composite comprises 4.78% carbon (and so CNTs) by weight. However, the alignment of these nanotubes suggests that it will exhibit properties more closely resembling those of actual composites with a higher weight percentage of CNTs.

The next assumption that must be addressed is the periodic nature of the loading on the system. Because of the periodic boundary conditions, the results presented here are for an infinitely long composite block, to which a force is applied every 204\AA along the length of the CNT. In contrast, most experimental studies apply a force to a macroscale block of composite. Subsequently, a small strain on the block of composite can result in a large displacement along the length of a nanotube. For example, the composite used by Zhou *et al.* [54] contained CNTs with lengths approaching $1\mu\text{m}$. Over that distance, a strain of 0.001 produces a displacement of 10\AA . By contrast, the same displacement in the simulated composite used here would require a strain of 0.206. If, as is hypothesized, damping in CNT composites is driven by interfacial slip, it is the displacement of the composite matrix relative to a CNT, not the strain, that dictates the magnitude of the damping. For that reason, conversions will be required when directly comparing computational results for damping as a function of strain to equivalent experiments.

6.3.1 Stiffness

Before damping is considered, it is instructive to examine the impact of defects on the stiffness of an Al/CNT composite both to aid in understanding the relevance of these defects, and to provide a benchmark with which to compare these simulations to experimental results. As the composite models may have a non-linear response, it is more accurate to say that their effective stiffness will be considered, at a given amplitude. However, experimental studies on CNT composites, such as [128], suggest that the response of CNT composite is weakly non-linear in the elastic region of the matrix's stress-strain curve, making the effective stiffness at one point within that region a good estimate of the stiffness of the composite throughout

the range of typical operating strains. Composite models containing a pristine CNT, a CNT with a single Stone-Wales defect, and a CNT with a single two-atom multi-vacancy defect are compared to a sample of aluminum with no CNT reinforcement. Each model is subjected to a loading force of $0.2 \text{ eV}/\text{\AA}$ on the loaded atoms (as described in the previous section). The displacements of the loaded atoms are found using the previously described conjugate gradient method, and the average displacement of these atoms in the direction of loading is used as the maximum displacement of the model. The stiffness is then found by dividing the applied load ($0.2 \text{ eV}/\text{\AA}$) by the maximum displacement. The resulting stiffnesses are shown in Table 6.1.

Table 6.1: Relative stiffnesses of Al/CNT composites with various defects

Test Case:	Stiffness ($\text{eV}/\text{\AA}^2$)	Stiffness Increase
No CNT	0.12713	-
Pristine	0.13055	2.693%
Stone-Wales	0.12898	1.401%
Multi-Vacancy	0.12893	1.443%

6.3.2 Damping as a Function of Vibration Amplitude

As before, three cases of CNT reinforcement of the aluminum matrix are considered: reinforcement with a pristine CNT, with a CNT containing a single Stone-Wales defect, and with a CNT containing a single two-atom multi-vacancy defect. To ensure that the solution procedure does not incur any spurious damping, a control case is also considered, which consists simply of the aluminum matrix without a CNT embedded in it. Each model undergoes the following loading conditions: the model is equilibrated with the boundary conditions applied but no external force on the loaded atoms; then, the force on the loaded atoms is increased in steps of $0.001 \text{ eV}/\text{\AA}$ and the average displacement of the loaded atoms is found for each step; when the maximum force is reached, the applied force is then decreased by steps of $0.001 \text{ eV}/\text{\AA}$, until the negative maximum force is reached; this process is repeated

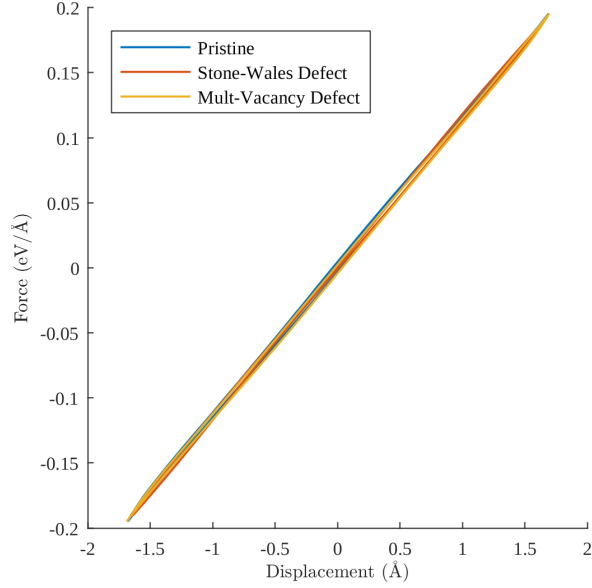


Figure 6.4: Representative hysteresis curves for Al/CNT composites with various defects undergoing a cyclic load with amplitude 0.21 eV/\AA

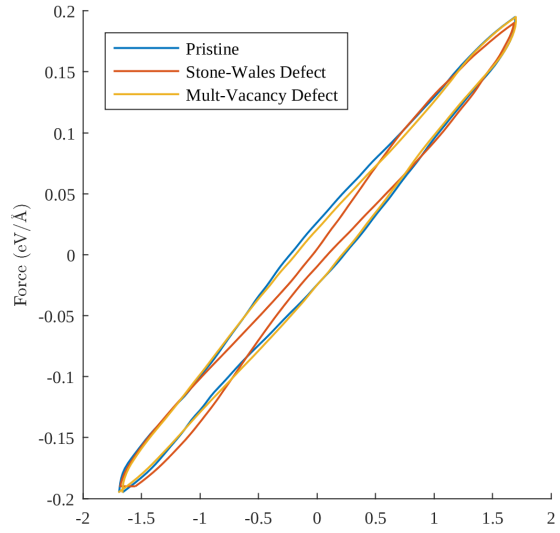


Figure 6.5: Representative hysteresis curves for Al/CNT composites with the distance between loading and unloading curves exaggerated by a factor of six

for four full cycles to ensure that the system is stable and the results are representative of the steady-state behavior of the system. For each case, the maximum loading was varied from 0.08 eV/\AA to 0.2 eV/\AA in increments of 0.01 eV/\AA .

Representative hysteresis loops for a maximum load of 0.2 eV/\AA are displayed in Fig. 6.4. The separation between loading and unloading curves is too small to be clearly distinguished, so in Fig. 6.5 the same data is shown, but the displacement of each point has been adjusted so that the distance between loading and unloading curves is six times greater. This is purely to better illustrate the nature of the interaction between the CNT and the aluminum matrix, and for that reason the scale on the x-axis of this plot has been omitted.

To ensure that the results presented here represent the impact of a specific type of defect, rather than an anomaly due to the placement of the defect in a particular case, five distinct systems are tested for each type of defect, each with its defect in a randomly chosen different location. Consequently, the raw data is too extensive to reproduce here. Instead, calculated quantities that have been averaged over the five systems for each defect are presented to

illustrate the impact of these defects.

A measure of damping that is equally valid for both linear and non-linear systems is the energy dissipation per cycle. Energy dissipation can be measured by finding the area enclosed by the force-displacement hysteresis curve for a complete loading cycle of the system. This value is calculated for each of the previously mentioned systems and is displayed in Fig. 6.6 (note that the energy loss for the control system is omitted, as it uniformly several orders of magnitude lower than that of the composite systems, and fluctuates in sign — indicating that it is simply an expression of numerical error). In this figure, error bars indicate standard error based on five repetitions with randomly placed defects. There is exactly one pristine system, therefore replication was not possible for those results.

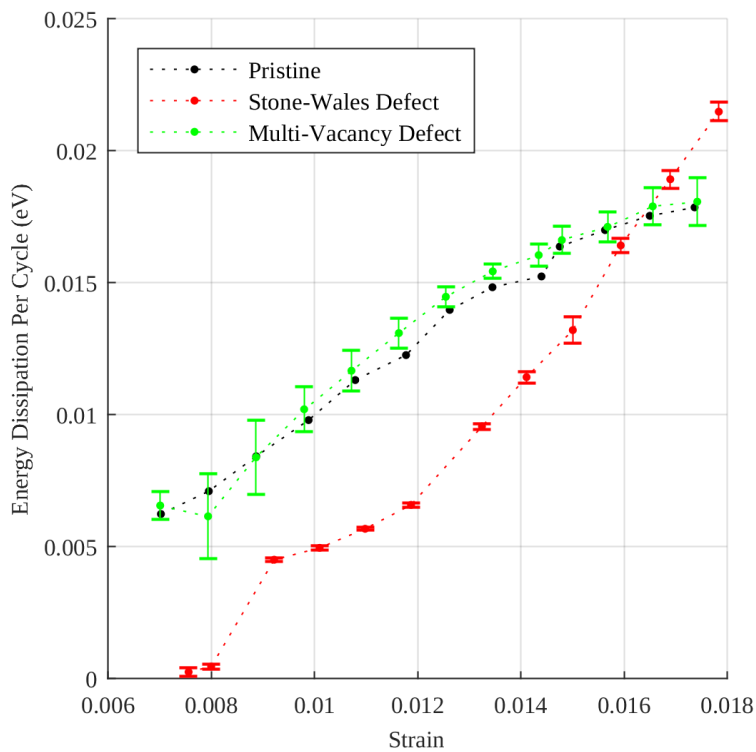


Figure 6.6: Energy dissipation per cycle for Al/CNT composites as a function of maximum strain

6.4 Discussion

Before a detailed analysis of the data gathered from these simulations can be performed, it is first necessary to check the validity of the data through comparison to experimental results available in the literature. Relatively little data has been gathered on the dynamics of Al/CNT composites, and that which is available comes in such a condensed and processed form that it is of little use for this type of comparison⁴. Instead, a static property of the composite, namely its stiffness, is used to validate these models. George *et al.* [48] provide detailed experimental and theoretical results for the stiffness of a Al/CNT composite containing only SWCNTs. They find that SWCNT that had not been subjected to treatments to functionalize their surface produce a minimal change in the stiffness of the composite. Similarly, Stein *et al.* found that the inclusion of CNT in an aluminum composite (1.5% by weight) increased its stiffness by only a maximum of 3% [145]. Not only do the numerical results here bear that out, but illustrate that the presence of Stone-Wales or multi-vacancy defects are potentially responsible for the observed variation in strengthening, as the models which contained these defects saw increases in stiffness that were roughly half the increase experienced by the pristine system.

The hysteresis curves provided by these simulations provide insight both into the mechanisms that control the interfacial interaction between CNTs and aluminum, and also into the role of defects in these interactions. Fig. 6.5 illustrates that the loading/unloading curves of these models do not follow the typical pattern of macroslip dampers (see chapter 3). Rather than experiencing a high initial stiffness which then decreases as the loading increases, these composites appear to experience sinusoidal variations in stiffness. This matches the theoretical results for interactions between nano-scale surfaces proposed by Cahangirov *et al.* [146], as well as the work on CNT/CNT interaction by Buldum and Lu [59]. Both these studies are

⁴An example of this is found in [49], where a sample of an Al/CNT composite is dynamically tested and the $\tan \delta$ curve — a measure of energy dissipation — is provided, but the amplitude of the vibration of the sample is not specified, preventing any meaningful comparison from being drawn.

concerned with the interaction of groups of bonded atoms that interact weakly with neighboring groups. They show that, when two groups move relative to each other, the net force between them as a function of displacement forms a series of peaks and troughs. The troughs correspond to those displacements that allow the atoms in the two groups to be staggered, while the peaks occur when atoms from different groups are forced together [59, 146]. In these studies, as in the results presented here, these weak interactions provide a source of energy dissipation.

An alternative way to understand the hysteresis curves of this composite is to note that atomic interactions can be both attractive and repulsive. When the system is perturbed a small amount from equilibrium, the interatomic forces will have a net repulsive effect — pushing the system back to equilibrium. If these forces are combined with a system that has a linear stiffness, the observed effect is an increase in stiffness. If, however, the system is displaced far enough from equilibrium, it is possible that it will approach a new equilibrium position⁵. As it approaches the new equilibrium, the net interatomic force will push the system towards the new equilibrium, and will so be an attractive force. The observed effect of this, when coupled with a linear stiffness, is a decrease in stiffness once a certain displacement is reached. Multiple fluctuations in stiffness, as observed in fig 6.5, indicate that multiple equilibria are reached over the course of one cycle.

Both the pristine and the multi-vacancy hysteresis curves follow roughly the same path, which accounts for the similarities in their energy dissipation (see Fig. 6.6), the systems with Stone-Wales defects follow a markedly different trajectory. The regions in the hysteresis curves where the loading and unloading trajectories become closer are indicative of regions where the stiffness of the interface between the CNT and the aluminum matrix reached a local minimum, and so are analogous to the troughs in interaction force shown in [59, 146]. The decrease in stiffness, followed by an increase in stiffness shows that the points where the distance between loading and unloading curves is locally minimized are the points where the

⁵A key difference between linear and non-linear systems is that a linear system has exactly one equilibrium point, while a non-linear system may have many equilibrium points or even equilibrium regions [104]

net interatomic force switches from being attractive to being repulsive. Put another way, these minima are ‘sticking points’ between the CNT and the aluminum. The pristine and multi-vacancy defect cases experience two such minima in the representative hysteresis curve shown, while the Stone-Wales defect case experiences only one. This decrease in the number of ‘sticking points’ between the CNT and the aluminum is minimized corresponds to the experimental observations of Bylinskii *et al.*, who examined the interaction between chains of ytterbium ions confined by optical lattices [134]. They find that, as the interatomic spacing in the chains is adjusted and the number of positions at which these chains can minimize their interaction forces, they are able to slip more readily. At its limit (when no force minima exist), this results in the so-called Aubry transition and the chains of atoms become superlubricious relative to each other [134, 147].

The energy dissipation of the composite systems shown in fig 6.6 reveals several significant findings concerning the behavior of CNT composites. Both the pristine and multi-vacancy systems display energy dissipation that increases at a decreasing rate as a function of amplitude. In combination with its higher stiffness, this shows that the pristine CNT is more strongly connected to matrix, and that after an initial slip, that connection does not significantly diminish. The similar damping behavior of the multi-vacancy systems, coupled with their lower stiffness, demonstrates that their behavior is similar, but the strength of the interaction between the CNTs with multi-vacancies and the aluminum matrix is weaker. The CNTs with Stone-Wales defects behave significantly differently. An energy dissipation curve that initially curves upwards, then becomes linear, is characteristic of a transition from microslip to macroslip.

Fig. 6.6 clearly shows that the Stone-Wales defect cases do not begin to slip (and therefore dissipate energy) until a strain of approximately 8×10^{-3} is reached⁶. At the same strain, both the pristine and multi-vacancy systems are already slipping. Typically this behavior would

⁶As previously mentioned, it is not the strain but the displacement at the interface that is responsible for slipping and energy loss. Provided that the aluminum atoms at the interface experience the average strain of all the atoms in the matrix, a strain of 8×10^{-3} corresponds here to an interfacial displacement of 1.63Å

suggest that a Stone-Wales defect should decrease the total amount of energy dissipated per cycle for any amplitude. However, the slope of the energy dissipation curve shows that, once slip has occurred, the increase in energy dissipation due to an increase in strain is significantly greater for the systems containing Stone-Wales defects. This can be explained by observing in Fig. 6.5 that, though the Stone-Wales defect decreases the number of ‘sticking points’ between the CNT and the matrix, the change in slope at these points is more pronounced — indicating a stronger interaction.

An alternative method of examining the amount of damping provided by these systems, and one that aligns with the way in which damping is reported by Zhou *et al.* [54], is in terms of the loss factor. The loss factor for a system undergoing cyclic loading is simply the average energy dissipation per radian divided by the maximum potential energy of the system during one cycle. There are numerous methods of computing the maximum potential energy for a non-linear system [148]. However, as the system is weakly nonlinear (as demonstrated in Fig. 6.4), the maximum potential energy of the system can be approximated using the equivalent stiffness of the system, thus

$$T_{\max} \approx \frac{1}{2} k_{\text{eq}} d_{\max}^2 \quad (6.4.1)$$

The loss factors of the composite systems as a function of strain are shown in Fig. 6.7. In this figure, the variation in loss factor for low amplitude the multi-vacancy cases appears very high. While there is noticeable variation in the energy dissipation of these systems (see Fig. 6.6), the loss factor exaggerates this by dividing it by the amplitude squared.

As the behavior of the systems with Stone-Wales defects can be observed from the point at which slipping starts, it is easy to compare their behavior to published result for other CNT composites⁷. Though Zhou *et al.* examine the impact of CNTs on polymer composites, their is a distinct similarity in the response of loss factor to strain in the results found here [54].

⁷Results for lower strains are not reported, as the numerical method used to solve these systems requires a certain magnitude of initial displacement to ensure accurate results. This limitation will be addressed in future studies

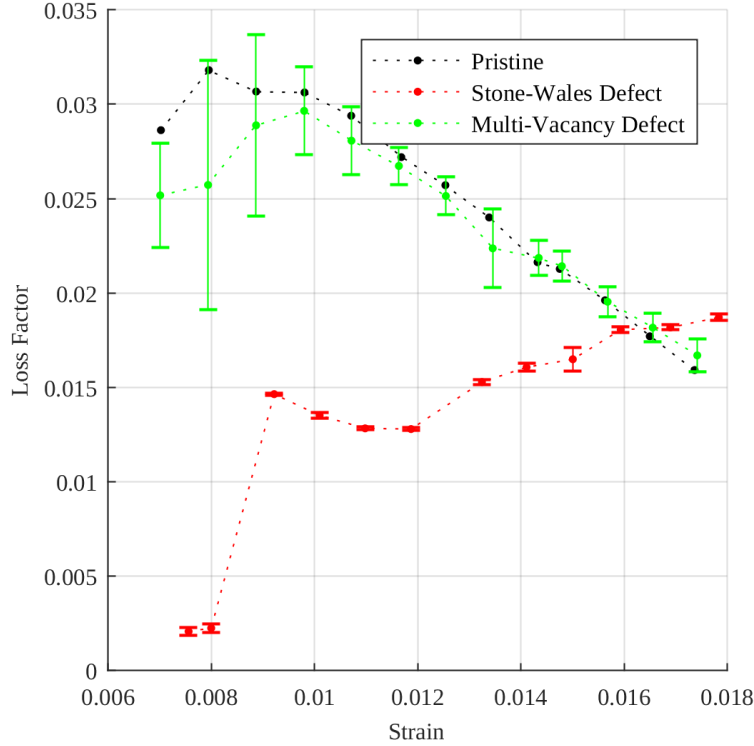


Figure 6.7: Loss factors for the Al/CNT composites as a function of maximum strain. Error bars indicate standard error based on five trials.

In both cases, the loss factor is initially close to zero — when no slip is occurring — rises sharply, dips, and rises more gradually. The initial rise and then dip correspond to the loss factor for a macroslip damper in parallel with a spring (see Appendix E), while the gradual rise that follows is a result of the system’s geometry (as the strain increase, the Poisson effect causes the inclusion in which the CNT is embedded to decrease in radius, increasing the magnitude of the Al/CNT interaction — this is derived in [54]). This same behavior was found by [128, 135] (note that these two papers do not report loss factor directly, but it can be calculated by dividing the loss modulus by the storage modulus [148]). The systems with a pristine CNT and with CNTs containing multi-vacancy defects, due to their lower rate of energy dissipation, have loss factors that decrease with increasing strain in the range of strains under consideration. However, this is not an indication that a different type of damping is occurring. Numerical results by Latibari *et al.* and theoretical work by Zhou *et al.* both show that this behavior indicates macroslip damping between to materials that

are very weakly bonded [54,57]. Given a sufficient range of strains, the loss factor curve for weak macroslip interactions is visually similar to that for strong interactions, but instead of a short dip then a rise after the initial peak, the loss factor decreases and asymptotically approaches a minimum value.

The relative insignificance of a multi-vacancy defect on damping when compared to the impact of a Stone-Wales defect requires some explanation. While the multi-vacancy defect is a major structural perturbation of a CNT, it is observed that the presence of a stable multi-vacancy causes the radius of the CNT to decrease in the vicinity of the defect [120]. This decrease in radius not only causes a weakened overall interaction between the CNT and the matrix, as witnessed by the decreased stiffness of the systems with multi-vacancy defects, but limits the extent to which the defect itself interacts with the matrix, preventing the disorder surrounding the defect from reducing the number of stable configurations of the composite. It is important to note, however, that the multi-vacancy bearing CNTs used here were allowed to reach an equilibrium state in vacuum — that is to say that the multi-vacancies were not introduced into the system while the CNTs were in contact with the aluminum. It is possible that the processes involved in fabricating Al/CNT composites could produce multi-vacancy defects while the CNTs are in contact with the matrix, which could result in a different reconfiguration of the CNTs.

6.5 Conclusion

Models are constructed of CNTs embedded in aluminum matrices. Pristine CNTs, and CNTs with single Stone-Wales or multi-vacancy defects are considered. The order of these models is reduced using Guyan reduction to eliminate unnecessary degrees of freedom from the aluminum matrix and MDA, MMDA, and MDR for the pristine CNT, the CNTs with Stone-Wales defects, and the CNTs with multi-vacancy defects, respectively. Using these models the quasi-static response of these composites under cyclic loading is calculated using

the conjugate gradient method to solve the resulting systems of nonlinear equations. These results reveal that both Stone-Wales and multi-vacancy defects reduce the ability of a CNT to increase the stiffness of an aluminum composite. The presence of a Stone-Wales defect permits the system to dissipate more energy per cycle (at a sufficiently high strain) than either a pristine CNT or a CNT with a multi-vacancy defect. A multi-vacancy defect did not have a significant impact on the damping of the composite.

Chapter 7

Conclusion and Future Work

Inevitable defects in carbon nanotubes (CNTs) are shown here to result in significant changes both in the free vibration of CNTs and in the dynamics of CNT composites. Not only do these results demonstrate the importance of considering defects when simulating CNTs and their composites, they also provide evidence that the properties of CNT composites can be tuned by intentionally inducing certain defects in the embedded CNTs.

To facilitate the study of damping in CNT composites, microslip and macroslip damping models are examined in detail. Using the method of harmonic balance, it is determined that a microslip damper is capable of stabilizing a system subjected to negative damping. Subsequently, a material that acts as a microslip damper can be used to stabilize structures such as turbine rotors that experience self-exciting aeroelastic oscillations (flutter). In addition, it is shown that a macroslip damper is capable of dissipating more energy per cycle than an equivalent microslip damper.

Three defects are considered in this dissertation: isotope defects, Stone-Wales defects, and multi-vacancy defects. Isotope defects, the presence of multiple carbon isotopes within a single CNT, are shown to have little impact on the natural frequencies of the CNT, but nevertheless cause significant changes in the corresponding normal modes. Using modal domain analysis (MDA), it is shown that a reduced-order system that preserves the natural frequencies and normal modes of the defect-bearing carbon nanotube (over a a chosen range of

frequencies) can be produced. The process of reducing the order of the system and evaluating its vibrational properties is significantly more efficient than solving the same eigenproblem on the full-order system. Additionally, an alternative order reduction method, modified modal domain analysis (MMDA), is applied to CNTs with isotope defects. It is shown that MMDA can produce a reduced order model that accurately predicts the vibrational properties of these systems.

MMDA is also adapted for use with CNTs containing Stone-Wales defects. A structural defect caused by the rotation of a pair of carbon atom in the plane tangent to the surface of the CNT, a Stone-Wales defect is shown to produce large changes in both the normal modes and natural frequencies of a CNT. These modes and frequencies (once again, within a given range) are retained in the reduced-order model, greatly reducing the computational cost of these calculations. In contrast, it is shown that MDA could not produce an accurate reduced-order model for this type of defect.

To more efficiently analyze CNTs containing multi-vacancy defects, a novel order reduction method called modal domain reduction (MDR) is developed. Like MDA and MMDA, MDR uses information from the easily calculated vibrational properties of a pristine CNT (one without defects) to reduce the order of the defect-bearing CNT. However, MDR is possibly unique among modal order reduction methods as it does not require the pristine and perturbed system to contain the same number of degrees of freedom. Using MDR, the order of CNTs containing a variety of multi-vacancy defects is reduced without significantly altering the natural frequencies and normal modes over a specified frequency range.

The order reduction methods that are developed here are used to construct a model of a CNT composite, in which a defect-bearing CNT is embedded in an aluminum matrix. The order of the aluminum matrix is reduced using Guyan reduction. Five cases are considered: a control in which no CNT is embedded in the matrix¹, a pristine case with no defect in the

¹For the control case, the inclusion that is filled by a CNT in the other cases is left empty. This choice is motivated by the results of [145], which demonstrate that the addition of 1.5% CNTs does not impact the density of the composite when compared to similarly prepared and sintered aluminum powder. Furthermore, micrography of the structure of the composite reveals significant porosity even in the absence of CNT, making

CNT, a model in which the CNT contains a Stone-Wales defect, and a model in which the CNT contains a multi-vacancy defect. There is only one possible control case and pristine case, so only one trial of each was necessary. Five trials of each defect-bearing case are used to ensure that the results are consistent. These simulations demonstrate that, while a pristine CNT produces only a slight increase in the stiffness of the composite, that increase in stiffness due to a defect-bearing CNT is even less. The presence of a multi-vacancy defect is found to have little impact on the damping of the composite, but a single Stone-Wales defect increases the strain on the composite required to cause the CNT to slip. Furthermore, beyond a certain strain the energy dissipation per cycle of the Stone-Wales cases are greater than the that of either the pristine or multi-vacancy cases. The energy dissipation and loss factor of these composites point to CNT composites acting as macroslip dampers.

Order reduction for atomic systems is a very new area of investigation, therefore there is significant room to expand on the work that is presented here. Other defects in CNTs and similar periodic structures could be analyzed using the same or related methods. Additionally, the results of the simulations of CNT composites highlight additional avenues that can be explored that might lead to a better understanding of the behavior of these materials. Variability was observed in the energy dissipation of the multi-vacancy cases at low strains, suggesting that attributes of the CNT other than the type of defect might be influencing its behavior. An investigation of the impact of the local strain in the neighborhood of the defect on the damping of the system might shed light on the overall response of the system.

a comparison of an Al/CNT composite to an uninterrupted sample of single-crystal aluminum less meaningful than a comparison to a porous sample of aluminum.

Appendix A

Derivation of the Nondimensionalized Single Degree of Freedom Equations of Motion

Using equations 3.3.2a - 3.3.2h, eq. ?? reduces to

$$\ddot{x}(t) - 2\zeta_+\dot{x}(t) + (1 - \epsilon)x(t) + p(x) = 0 \quad (\text{A.1})$$

where:

$$p(x) := p^*(x(t) x_0) / [x_0 (k + k_d)] \quad (\text{A.2})$$

Note that non-dimensional damper force p remains dependent on the dimensional parameters p_{fs}^* , k_d , Δ_s , and Δ_{fs} . To fully nondimensionalize the system, the parameters on which p depends must also be nondimensionalized. This will be done separately for the no slip, partial slip, and full slip cases.

No slip

$$p^*(x^*) = k_d x^* \quad (\text{A.3})$$

From eq. A.2 and eq. 3.3.2,

$$p(x) = \epsilon x \quad (\text{A.4})$$

Partial slip

$$x^*(a) = \frac{\tau_m}{k_s} \{1 + \lambda^2 a [(a/2) + \tanh \lambda (1 - a)/\lambda]\} \quad (\text{A.5})$$

$$p^*(a) = (\tau_m L) [a + \tanh \lambda (1 - a)/\lambda] \quad (\text{A.6})$$

From eq. 3.3.2,

$$x(a) = x_s \{1 + \lambda^2 a [(a/2) + \tanh \lambda (1 - a)/\lambda]\} \quad (\text{A.7})$$

where

$$x_s := \Delta_s/x_0 \text{ and } x_{fs} := \Delta/x_0 \quad (\text{A.8})$$

From eq. A.2 and eq. 3.2.8,

$$p(a) = \epsilon [a + \tanh \lambda (1 - a)/\lambda] \quad (\text{A.9})$$

Full slip:

$$p_{fs}^* = \tau_m L \quad (\text{A.10})$$

From eq. A.2 and eq. 3.2.8,

$$p_{fs} = \epsilon \quad (\text{A.11})$$

Furthermore, from equations 3.3.2 and A.8

$$x_s = \frac{\tanh \lambda}{\lambda} \quad (\text{A.12})$$

$$x_{fs} = \frac{\tanh \lambda}{\lambda} \left(1 + \frac{\lambda^2}{2}\right) \quad (\text{A.13})$$

Equations A.12 and A.13 demonstrate that x_s and x_{fs} are only functions of nondimensional parameter λ , and therefore x_{fs} depends only on x_s . Hence, the only parameters needed to

uniquely define the nondimensionalized microslip damper are ϵ and x_s .

Appendix B

Energy Dissipation by Macroslip and Microslip Dampers in Full Slip Conditions

Comparison between macroslip and microslip dampers

It will be shown here that when both dampers are slipping fully, the macroslip damper provides greater amount of damping. The energy dissipated by a damper is equal to the area inside its hysteresis curve, so to prove that the macroslip damper provides more damping (dissipates more energy), it is sufficient to prove that the microslip hysteresis curve lies inside the macroslip hysteresis curve in full slip conditions, Fig. 3.

Let A be greater than x_{fs} i.e., both dampers are slipping fully. The microslip hysteresis curve lies inside the macroslip hysteresis curve if, for all times, t , the microslip damper force, p_m , is less than or equal to the macroslip damper force, p_M , and if there is a range of t for which p_m is strictly less than p_M . Clearly, for fully stuck ($A \leq x_s$) and for fully slipping ($A \geq x_{fs}$), $p_m = p_M$. It only remains to show that during partial slip, $p_m < p_M$.

The condition $p_m < p_M$ will be satisfied if, at the transition between the fully stuck and the partial slip regions, the slopes of p_m and p_M are the same, and the slope of p_m decreases throughout the region while still remaining positive. In other words:

$$\left. \frac{dp_m}{dx} \right|_{x=x_s} = \left. \frac{dp_M}{dx} \right|_{x=x_s} = \epsilon \quad (\text{B.1a})$$

$$\frac{dp_m}{dx} > 0 \quad (\text{B.1b})$$

$$\frac{d^2p_m}{dx^2} < 0 \quad (\text{B.1c})$$

The first condition eq. B.1a is easily checked by evaluating the derivative of eq. A.9 at $a = 0$. Using equations A.7 and A.9,

$$\frac{dp_m}{dx} = \frac{dp_m}{da} \left(1/\frac{dx}{da}\right) = \frac{\epsilon \coth(\lambda - a\lambda) [1 + a\lambda \coth(\lambda - a\lambda)]}{x_s \lambda^2 [a\lambda + \coth(\lambda - a\lambda)]} \quad (\text{B.2a})$$

$$\frac{d^2p_m}{dx^2} = \frac{d^2p_m}{da^2} \left(\frac{dx}{da}\right)^{-2} - \frac{dp_m}{da} \frac{d^2x}{da^2} \left(\frac{dx}{da}\right)^{-3} = -\frac{\epsilon \coth(\lambda - a\lambda)^4}{x_s^2 \lambda [a\lambda + \coth(\lambda - a\lambda)]^3} \quad (\text{B.2b})$$

The right hand side of eq. B.2a is positive for $0 < a < 1$, proving that the slope of the microslip hysteresis curve is strictly positive in the partial slip region. The right hand side of eq. B.2b is negative for $0 < a < 1$, proving that the slope of the microslip hysteresis curve decreases in the partial slip region. Therefore, $p_m < p_M$ and it can be concluded that, when the $A > x_{fs}$, the macroslip damper provides more damping than the microslip damper.

Comparison between microslip dampers with different slip distances

Now energy dissipation by two microslip dampers with different values of x_s will be compared in full slip conditions. Substituting eq. A.12 into eq. B.2a,

$$\frac{dp_m}{dx} = \frac{\epsilon \lambda \coth(\lambda - a\lambda) [1 + a\lambda \coth(\lambda - a\lambda)]}{\lambda^2 \tanh(\lambda) [a\lambda + \coth(\lambda - a\lambda)]} \quad (\text{B.3})$$

The right hand side of eq. B.3 is strictly decreasing with respect to λ (for $0 < a < 1$) and λ decreases as x_s increases, from eq. A.12. Hence, as x_s increases, the slope of p_m must increase to reach the constant damper force at full slip for a smaller value of $x_{fs} - x_s$. Therefore the hysteresis curve for the damper with a lower value of x_s , which will have a lower value of damper force at which partial slip starts, will be inside the hysteresis curve of the damper with a higher value of x_s (provided the displacement is large enough that both dampers are slipping fully). This shows that when two microslip dampers with different values of x_s are

slipping fully, the damper with a larger value of x_s will provide more damping.

Appendix C

Proof That the Sum of MAC Values of a Vector and Its Basis is 1

Mathematically, the MAC value of vectors $\boldsymbol{\alpha}$ and $\boldsymbol{\beta}$ can be written [113]

$$\text{MAC}(\boldsymbol{\alpha}\boldsymbol{\beta}) = \frac{|\boldsymbol{\alpha}^T\boldsymbol{\beta}|^2}{|\boldsymbol{\alpha}^T\boldsymbol{\alpha}||\boldsymbol{\beta}^T\boldsymbol{\beta}|} \quad (\text{C.1})$$

Let a set of vectors $\mathbf{b}_1, \dots, \mathbf{b}_n$ be defined such that they form an orthogonal basis for vector \mathbf{a} and

$$\mathbf{a} = \sum_{i=1}^n \gamma_i \mathbf{b}_i \quad (\text{C.2})$$

where γ_i is the coefficient of basis vector \mathbf{b}_i . The MAC value of \mathbf{a} and \mathbf{b}_j is

$$\text{MAC}(\mathbf{a}, \mathbf{b}_j) = \frac{\left| \left(\sum_{i=1}^n \gamma_i \mathbf{b}_i \right)^T \mathbf{b}_j \right|^2}{\left| \left(\sum_{i=1}^n \gamma_i \mathbf{b}_i \right)^T \left(\sum_{i=1}^n \gamma_i \mathbf{b}_i \right) \right| |\mathbf{b}_j^T \mathbf{b}_j|} = \frac{|\gamma_j^2 \mathbf{b}_j^T \mathbf{b}_j|}{\left| \sum_{i=1}^n \gamma_i^2 \mathbf{b}_i^T \mathbf{b}_i \right|} \quad (\text{C.3})$$

The sum of the MAC values of \mathbf{a} and each \mathbf{b}_i is then

$$\sum_{j=1}^n \text{MAC}(\mathbf{a}, \mathbf{b}_j) = \sum_{j=1}^n \left(\frac{|\gamma_j^2 \mathbf{b}_j^T \mathbf{b}_j|}{\left| \sum_{i=1}^n \gamma_i^2 \mathbf{b}_i^T \mathbf{b}_i \right|} \right) \equiv 1 \quad (\text{C.4})$$

Appendix D

Supplemental Numerical Analyses of Carbon Nanotubes with Multi-Vacancy Defects

The analyses of CNTs containing multi-vacancy defects presented in Chapter 5 are representative of the results of MDR and MDA under the worst-case scenarios (when the combination of parameters causes the natural frequencies of the perturbed systems to deviate by the greatest amount from those of the pristine system). Included here are the results for the full range of parameters tested. These results were omitted from the body of this dissertation for the sake of brevity.

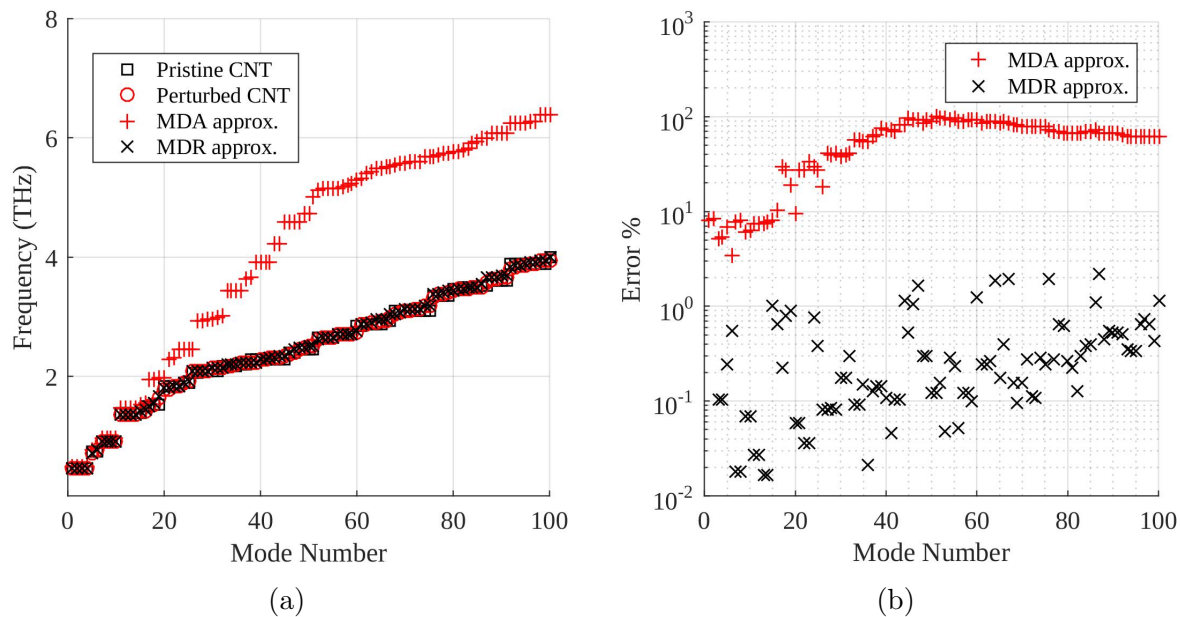


Figure D.1: Frequency (a) and frequency error (b) for MDR ($\omega = 0$) and MDA approximations of a (6,6) CNT with a single 2-atom MVD.

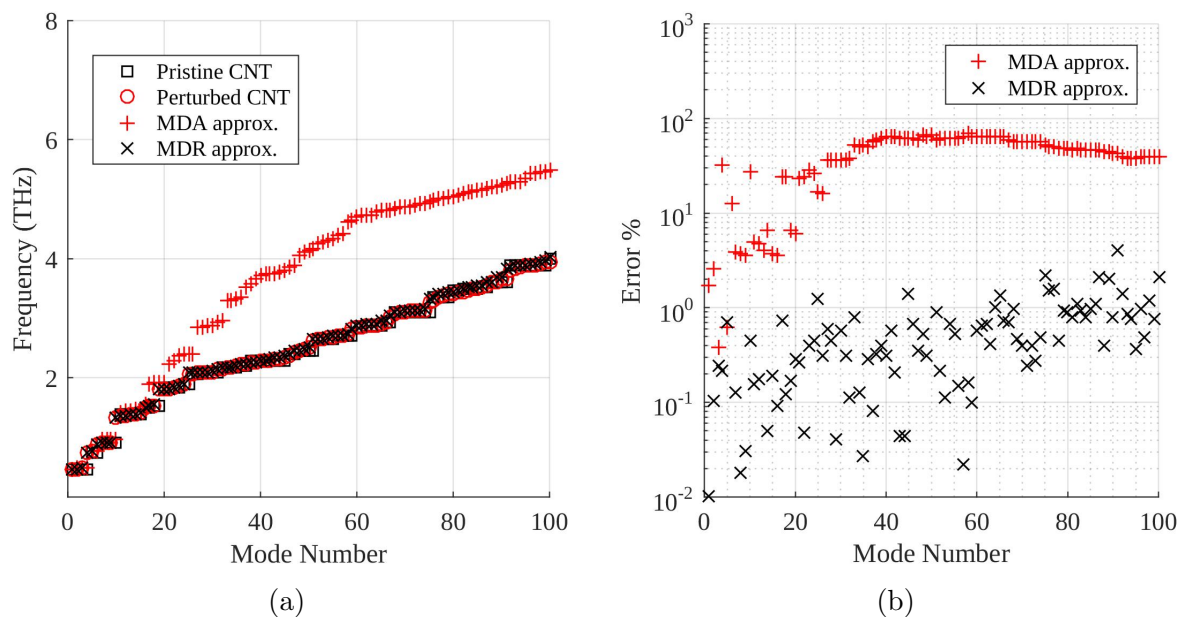


Figure D.2: Frequency (a) and frequency error (b) for MDR ($\omega = 0$) and MDA approximations of a (6,6) CNT with a single 4-atom MVD.

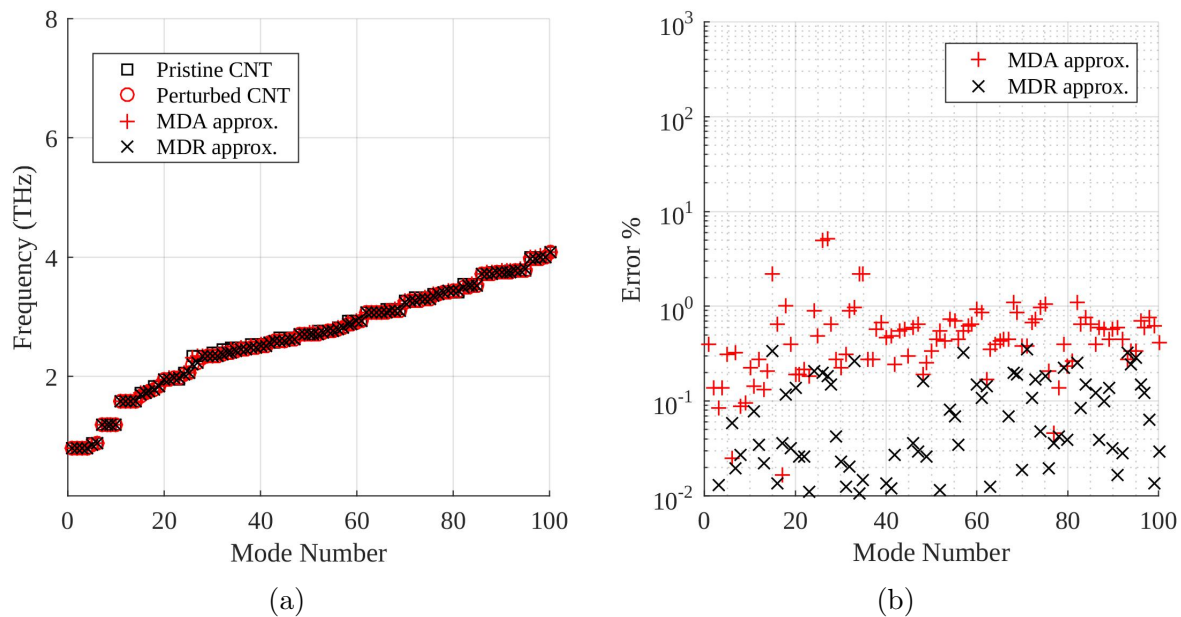


Figure D.3: Frequency (a) and frequency error (b) for MDR ($\omega = 0$) and MDA approximations of a (10,0) CNT with a single 2-atom MVD.

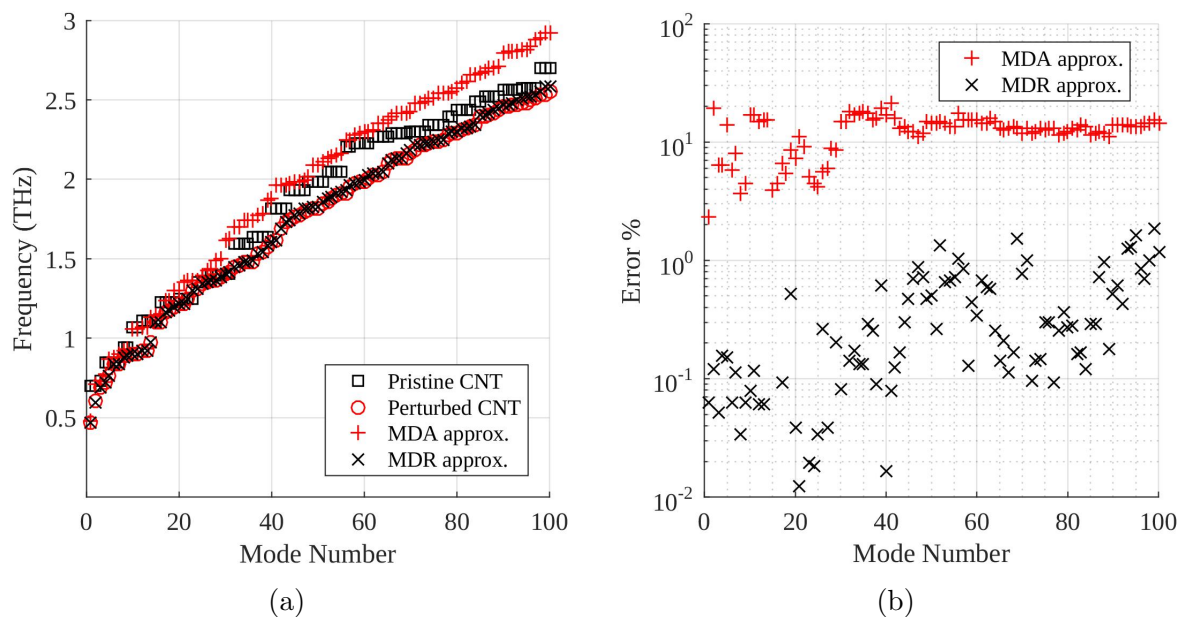
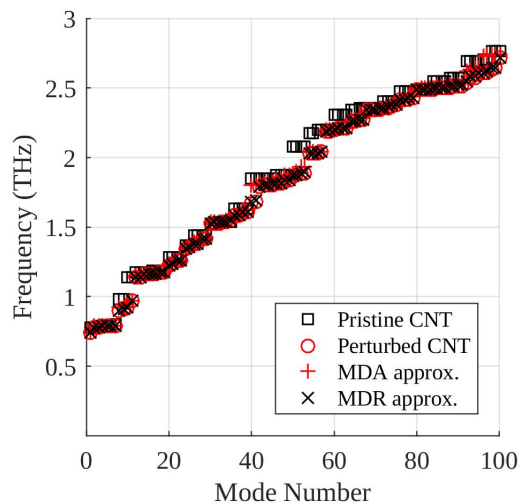
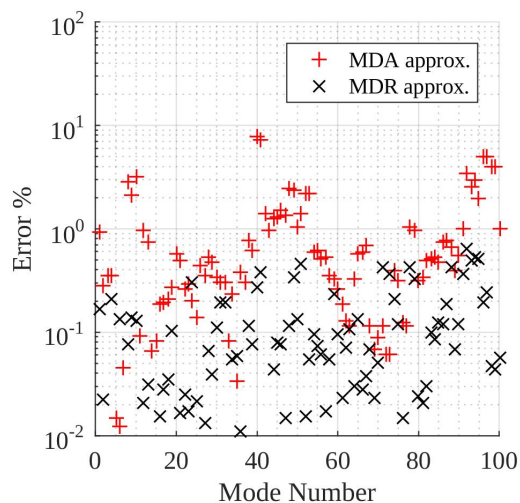


Figure D.4: Frequency (a) and frequency error (b) for MDR ($\omega = 0$) and MDA approximations of a (10,10) CNT with a single 4-atom MVD.

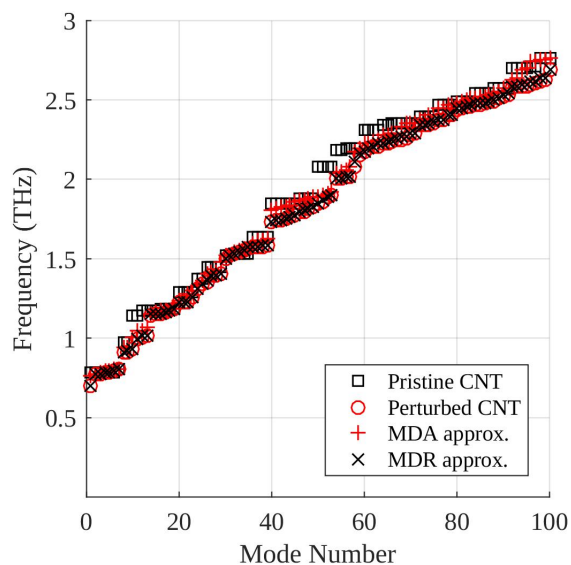


(a)

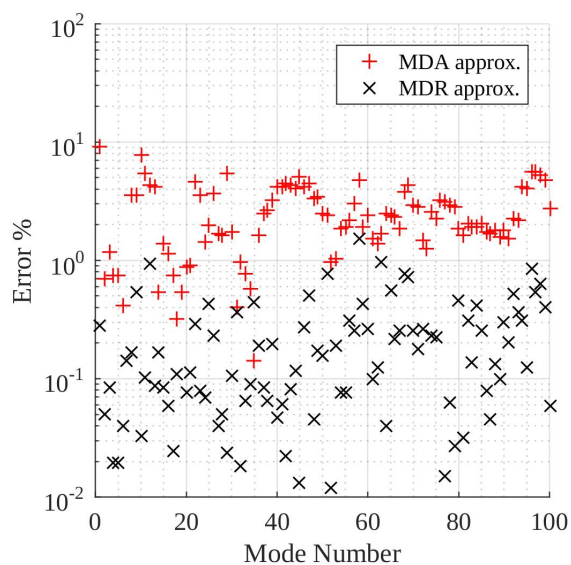


(b)

Figure D.5: Frequency (a) and frequency error (b) for MDR ($\omega = 0$) and MDA approximations of a (17,0) CNT with a single 2-atom MVD.



(a)



(b)

Figure D.6: Frequency (a) and frequency error (b) for MDR ($\omega = 0$) and MDA approximations of a (17,0) CNT with a single 4-atom MVD.

Appendix E

Loss Factor of a Macroslip Damper in Parallel with a Spring

A macroslip damper is characterized by two quantities: the displacement at which slipping occurs (x_s) and the force at which slipping occurs (f_s). In virtually all cases, the damper is modeled as a stick-slip interface in series with a linear spring to simulate the compliance of a physical damper. Given a spring with stiffness k_1 , the parameter f_s is clearly equal to $k_1 x_s$. The energy dissipated by a damper is equal to the area enclosed by its hysteresis curve — in the case of a macroslip damper, this curve forms a parallelogram with height $2f_s = 2kx_s$ and with a base of length $2(a - x_s)$, where a is the amplitude of excitation. If a is less than x_s , no slipping and therefore no energy dissipation occurs. For $a > x_s$, the energy dissipated per cycle is equal to $4kx_s(a - x_s)$.

Before a spring is added in parallel with the damper, the only device in the system that is capable of storing energy is the linear spring. Therefore, the maximum kinetic energy per cycle is $1/2k_1x_s^2$, provided that $a > x_s$. The loss factor of a system is simply the average energy dissipation per radian (the energy dissipation per cycle divided by 2π) divided by the maximum potential energy in a cycle [148]. Therefore, the loss factor of the damper alone

(\mathcal{L}_d) can be calculated as follows

$$\mathcal{L}_d = \frac{4k_1x_s(a - x_s)}{2\pi(1/2k_1x_s^2)} = \frac{4(a - x_s)}{\pi x_s} \quad (\text{E.1})$$

When a spring with stiffness k_2 is added in parallel with the damper, it does not alter the energy dissipation for a given cycle amplitude. However, this additional spring continues to store energy after the damper begins slipping, radically altering its loss factor. Once again, the loss factor is exactly zero until $x = x_s$, as no energy loss is incurred until the damper begins to slip. When $x > x_s$, the potential energy stored by the spring within the damper remains constant at $1/2k_1x_s^2$, and the energy stored by the parallel spring increases with displacement, as $1/2k_2x^2$. Therefore, the maximum potential energy stored by the system during one cycle is $1/2(k_1x_s^2 + k_2a^2)$. The loss factor for the damper in parallel with a spring is

$$\mathcal{L} = \frac{4k_1x_s(a - x_s)}{\pi(k_1x_s^2 + k_2a^2)} \quad (\text{E.2})$$

For $k_2 \gg k_1$ or $a \gg x_s$, this reduces to

$$\mathcal{L} \approx \frac{4k_1x_s}{\pi k_2a} \left(1 - \frac{x_s}{a}\right) \quad (\text{E.3})$$

Bibliography

- [1] E. T. Thostenson, Z. Ren, and T.-W. Chou, “Advances in the science and technology of carbon nanotubes and their composites: a review,” *Composites science and technology*, vol. 61, no. 13, pp. 1899–1912, 2001.
- [2] D. Qian, G. J. Wagner, W. K. Liu, M.-F. Yu, and R. S. Ruoff, “Mechanics of carbon nanotubes,” *Applied mechanics reviews*, vol. 55, no. 6, pp. 495–533, 2002.
- [3] P. Harris, “Carbon nanotube composites,” *International Materials Reviews*, vol. 49, no. 1, pp. 31–43, 2004.
- [4] A. N. Cleland, *Foundations of nanomechanics: from solid-state theory to device applications*. Springer Science & Business Media, 2013.
- [5] A. Jorio, M. S. Dresselhaus, R. Saito, and G. Dresselhaus, *Raman spectroscopy in graphene related systems*. John Wiley & Sons, 2011.
- [6] J. Maultzsch, S. Reich, C. Thomsen, E. Dobardžić, I. Milošević, and M. Damnjanović, “Phonon dispersion of carbon nanotubes,” *Solid state communications*, vol. 121, no. 9–10, pp. 471–474, 2002.
- [7] O. Dubay and G. Kresse, “Accurate density functional calculations for the phonon dispersion relations of graphite layer and carbon nanotubes,” *Physical Review B*, vol. 67, no. 3, p. 035401, 2003.
- [8] H. G. Craighead, “Nanoelectromechanical systems,” *Science*, vol. 290, no. 5496, pp. 1532–1535, 2000.
- [9] M. Roukes, “Nanoelectromechanical systems face the future,” *Physics World*, vol. 14, no. 2, p. 25, 2001.
- [10] K. Ekinici, “Kl ekinici and ml roukes, rev. sci. instrum. 76, 061101 (2005).,” *Rev. Sci. Instrum.*, vol. 76, p. 061101, 2005.
- [11] R. Schaller, “Metal matrix composites, a smart choice for high damping materials,” *Journal of Alloys and Compounds*, vol. 355, no. 1, pp. 131–135, 2003.
- [12] A. Sinha and J. H. Griffin, “Effects of friction dampers on aerodynamically unstable rotor stages,” *Journal of Aircraft*, vol. 23, no. 2, pp. 262–270, 1985.
- [13] E. H. Dowell, *A modern course in aeroelasticity*, vol. 217. Springer, 2014.

- [14] A. Sinha, *Vibration of Nearly Periodic Structures and Mistuned Bladed Rotors*. Cambridge University Press, 2017.
- [15] K.-H. Koh, J. H. Griffin, S. Filippi, and A. Akay, “Characterization of turbine blade friction dampers,” *Journal of engineering for gas turbines and power*, vol. 127, no. 4, pp. 856–862, 2005.
- [16] M. De Volder, S. Tawfick, R. Baughman, and A. J. Hart, “Carbon nanotubes: Present and future commercial applications,” vol. 339, pp. 535–539, 02 2013.
- [17] S. Iijima *et al.*, “Helical microtubules of graphitic carbon,” *Nature*, vol. 354, no. 6348, pp. 56–58, 1991.
- [18] S. Reich, C. Thomsen, and J. Maultzsch, *Carbon nanotubes: basic concepts and physical properties*. John Wiley & Sons, 2008.
- [19] A. Krishnan, E. Dujardin, T. Ebbesen, P. Yianilos, and M. Treacy, “Young’s modulus of single-walled nanotubes,” *Physical Review B*, vol. 58, no. 20, p. 14013, 1998.
- [20] H. Wagner, O. Lourie, Y. Feldman, and R. Tenne, “Stress-induced fragmentation of multiwall carbon nanotubes in a polymer matrix,” *Applied physics letters*, vol. 72, no. 2, pp. 188–190, 1998.
- [21] G. Gao, T. Cagin, and W. A. Goddard III, “Energetics, structure, mechanical and vibrational properties of single-walled carbon nanotubes,” *Nanotechnology*, vol. 9, no. 3, p. 184, 1998.
- [22] E. Hernandez, C. Goze, P. Bernier, and A. Rubio, “Elastic properties of c and b x c y n z composite nanotubes,” *Physical Review Letters*, vol. 80, no. 20, p. 4502, 1998.
- [23] Y. Han and J. Elliott, “Molecular dynamics simulations of the elastic properties of polymer/carbon nanotube composites,” *Computational Materials Science*, vol. 39, no. 2, pp. 315–323, 2007.
- [24] T. Chang and H. Gao, “Size-dependent elastic properties of a single-walled carbon nanotube via a molecular mechanics model,” *Journal of the Mechanics and Physics of Solids*, vol. 51, no. 6, pp. 1059–1074, 2003.
- [25] A. Sears and R. Batra, “Macroscopic properties of carbon nanotubes from molecular-mechanics simulations,” *Physical Review B*, vol. 69, no. 23, p. 235406, 2004.
- [26] R. Batra and A. Sears, “Continuum models of multi-walled carbon nanotubes,” *International Journal of Solids and structures*, vol. 44, no. 22, pp. 7577–7596, 2007.
- [27] H.-C. Cheng, Y.-L. Liu, Y.-C. Hsu, and W.-H. Chen, “Atomistic-continuum modeling for mechanical properties of single-walled carbon nanotubes,” *International Journal of Solids and Structures*, vol. 46, no. 7, pp. 1695–1704, 2009.

- [28] A. Kalamkarov, A. Georgiades, S. Rokkam, V. Veedu, and M. Ghasemi-Nejhad, “Analytical and numerical techniques to predict carbon nanotubes properties,” *International Journal of Solids and Structures*, vol. 43, no. 22, pp. 6832–6854, 2006.
- [29] Q. Wang and V. Varadan, “Vibration of carbon nanotubes studied using nonlocal continuum mechanics,” *Smart Materials and Structures*, vol. 15, no. 2, p. 659, 2006.
- [30] C. Li and T.-W. Chou, “A structural mechanics approach for the analysis of carbon nanotubes,” *International Journal of Solids and Structures*, vol. 40, no. 10, pp. 2487–2499, 2003.
- [31] M. Meo and M. Rossi, “Prediction of young’s modulus of single wall carbon nanotubes by molecular-mechanics based finite element modelling,” *Composites Science and Technology*, vol. 66, no. 11, pp. 1597–1605, 2006.
- [32] J. Xiao, B. Gama, and J. Gillespie, “An analytical molecular structural mechanics model for the mechanical properties of carbon nanotubes,” *International Journal of Solids and Structures*, vol. 42, no. 11, pp. 3075–3092, 2005.
- [33] H. Terrones, R. Lv, M. Terrones, and M. S. Dresselhaus, “The role of defects and doping in 2d graphene sheets and 1d nanoribbons,” *Reports on Progress in Physics*, vol. 75, no. 6, p. 062501, 2012.
- [34] T. Ebbesen and T. Takada, “Topological and sp³ defect structures in nanotubes,” *Carbon*, vol. 33, no. 7, pp. 973–978, 1995.
- [35] J.-C. Charlier, “Defects in carbon nanotubes,” *Accounts of chemical research*, vol. 35, no. 12, pp. 1063–1069, 2002.
- [36] Y. Fan, B. R. Goldsmith, and P. G. Collins, “Identifying and counting point defects in carbon nanotubes,” *Nature materials*, vol. 4, no. 12, pp. 906–911, 2005.
- [37] R. Gao, Z. L. Wang, Z. Bai, W. A. de Heer, L. Dai, and M. Gao, “Nanomechanics of individual carbon nanotubes from pyrolytically grown arrays,” *Physical Review Letters*, vol. 85, no. 3, p. 622, 2000.
- [38] S. Zhang, S. L. Mielke, R. Khare, D. Troya, R. S. Ruoff, G. C. Schatz, and T. Belytschko, “Mechanics of defects in carbon nanotubes: atomistic and multiscale simulations,” *Physical Review B*, vol. 71, no. 11, p. 115403, 2005.
- [39] N. Sakharova, A. Pereira, J. Antunes, and J. Fernandes, “Numerical simulation study of the elastic properties of single-walled carbon nanotubes containing vacancy defects,” *Composites Part B: Engineering*, vol. 89, pp. 155–168, 2016.
- [40] A. Chandrasher, S. Adhikari, and M. Friswell, “Quantification of vibration localization in periodic structures,” *Journal of Vibration and Acoustics*, vol. 138, no. 2, p. 021002, 2016.

- [41] Y. Chen and I. Shen, “Mathematical insights into linear mode localization in nearly cyclic symmetric rotors with mistune,” *Journal of Vibration and Acoustics*, vol. 137, no. 4, p. 041007, 2015.
- [42] P. Dean, “The vibrational properties of disordered systems: numerical studies,” *Reviews of modern physics*, vol. 44, no. 2, p. 127, 1972.
- [43] J. N. Coleman, U. Khan, W. J. Blau, and Y. K. Gun’ko, “Small but strong: a review of the mechanical properties of carbon nanotube–polymer composites,” *Carbon*, vol. 44, no. 9, pp. 1624–1652, 2006.
- [44] E. Bekyarova, E. Thostenson, A. Yu, H. Kim, J. Gao, J. Tang, H. Hahn, T.-W. Chou, M. Itkis, and R. Haddon, “Multiscale carbon nanotube-carbon fiber reinforcement for advanced epoxy composites,” *Langmuir*, vol. 23, no. 7, pp. 3970–3974, 2007.
- [45] G. Pal and S. Kumar, “Multiscale modeling of effective electrical conductivity of short carbon fiber-carbon nanotube-polymer matrix hybrid composites,” *Materials & Design*, vol. 89, pp. 129–136, 2016.
- [46] T. Kuzumaki, K. Miyazawa, H. Ichinose, and K. Ito, “Processing of carbon nanotube reinforced aluminum composite,” *Journal of Materials Research*, vol. 13, no. 09, pp. 2445–2449, 1998.
- [47] R. Chandra, S. Singh, and K. Gupta, “Damping studies in fiber-reinforced composites—a review,” *Composite structures*, vol. 46, no. 1, pp. 41–51, 1999.
- [48] R. George, K. Kashyap, R. Rahul, and S. Yamdagni, “Strengthening in carbon nanotube/aluminium (cnt/al) composites,” *Scripta Materialia*, vol. 53, no. 10, pp. 1159–1163, 2005.
- [49] C. Deng, D. Wang, X. Zhang, and Y. Ma, “Damping characteristics of carbon nanotube reinforced aluminum composite,” *Materials Letters*, vol. 61, no. 14, pp. 3229–3231, 2007.
- [50] A. Kelly and a. W. Tyson, “Tensile properties of fibre-reinforced metals: copper/tungsten and copper/molybdenum,” *Journal of the Mechanics and Physics of Solids*, vol. 13, no. 6, pp. 329–350, 1965.
- [51] J. Suhr, W. Zhang, P. M. Ajayan, and N. A. Koratkar, “Temperature-activated interfacial friction damping in carbon nanotube polymer composites,” *Nano letters*, vol. 6, no. 2, pp. 219–223, 2006.
- [52] M. Yadollahpour, J. Kadkhodapour, S. Ziaei-Rad, and F. Karimzadeh, “An experimental and numerical investigation on damping capacity of nanocomposite,” *Materials Science and Engineering: A*, vol. 507, no. 1, pp. 149–154, 2009.
- [53] B. Glaz, J. Riddick, E. Habtour, and H. Kang, “Interfacial strain energy dissipation in hybrid nanocomposite beams under axial strain fields,” *AIAA Journal*, vol. 53, no. 6, pp. 1544–1554, 2015.

- [54] X. Zhou, E. Shin, K. Wang, and C. Bakis, “Interfacial damping characteristics of carbon nanotube-based composites,” *Composites Science and Technology*, vol. 64, no. 15, pp. 2425–2437, 2004.
- [55] A. Liu, J. H. Huang, K. Wang, and C. Bakis, “Effects of interfacial friction on the damping characteristics of composites containing randomly oriented carbon nanotube ropes,” *Journal of intelligent material systems and structures*, vol. 17, no. 3, pp. 217–229, 2006.
- [56] X. He, M. Rafiee, S. Mareishi, and K. Liew, “Large amplitude vibration of fractionally damped viscoelastic cnts/fiber/polymer multiscale composite beams,” *Composite Structures*, vol. 131, pp. 1111–1123, 2015.
- [57] S. T. Latibari, M. Mehrali, L. Mottahedin, A. Fereidoon, and H. S. C. Metselaar, “Investigation of interfacial damping nanotube-based composite,” *Composites Part B: Engineering*, vol. 50, pp. 354–361, 2013.
- [58] R. Lin and C. Lu, “Modeling of interfacial friction damping of carbon nanotube-based nanocomposites,” *Mechanical Systems and Signal Processing*, vol. 24, no. 8, pp. 2996–3012, 2010.
- [59] A. Buldum and J. P. Lu, “Atomic scale sliding and rolling of carbon nanotubes,” *Physical Review Letters*, vol. 83, no. 24, p. 5050, 1999.
- [60] R. F. Gibson, E. O. Ayorinde, and Y.-F. Wen, “Vibrations of carbon nanotubes and their composites: a review,” *Composites science and technology*, vol. 67, no. 1, pp. 1–28, 2007.
- [61] C.-H. Menq, J. Bielak, and J. H. Griffin, “The influence of microslip on vibratory response, part i: A new microslip model,” *Journal of Sound and Vibration*, vol. 107, no. 2, pp. 279–293, 1986.
- [62] R. Hudson and A. Sinha, “Frictional damping of flutter: Microslip versus macroslip,” *Journal of Vibration and Acoustics*, vol. 138, no. 6, p. 061010, 2016.
- [63] A. R. Leach, *Molecular modelling: principles and applications*. Pearson education, 2001.
- [64] F. Bloch, “Über die quantenmechanik der elektronen in kristallgittern,” *Zeitschrift für physik*, vol. 52, no. 7-8, pp. 555–600, 1929.
- [65] G. Floquet, “Sur les équations différentielles linéaires à coefficients périodiques,” in *Annales scientifiques de l’École normale supérieure*, vol. 12, pp. 47–88, 1883.
- [66] A. Sinha, “Reduced-order model of a bladed rotor with geometric mistuning,” *Journal of Turbomachinery*, vol. 131, no. 3, p. 031007, 2009.
- [67] R. Bladh, M. Castanier, and C. Pierre, “Component-mode-based reduced order modeling techniques for mistuned bladed disks—part i: Theoretical models,” *Journal of Engineering for Gas turbines and Power*, vol. 123, no. 1, pp. 89–99, 2001.

- [68] A. Sinha, *Vibration of mechanical systems*. Cambridge University Press, 2010.
- [69] M.-T. Yang and J. Griffin, “A reduced order model of mistuning using a subset of nominal system modes,” in *ASME 1999 International Gas Turbine and Aeroengine Congress and Exhibition*, pp. V004T03A032–V004T03A032, American Society of Mechanical Engineers, 1999.
- [70] E. P. Wigner and F. Seitz, “On the constitution of metallic sodium,” in *The Collected Works of Eugene Paul Wigner*, pp. 365–371, Springer, 1997.
- [71] C. Kittel, *Introduction to solid state physics*. John Wiley & Sons, 1966.
- [72] G. R. Bhimanapati, Z. Lin, V. Meunier, Y. Jung, J. Cha, S. Das, D. Xiao, Y. Son, M. S. Strano, V. R. Cooper, *et al.*, “Recent advances in two-dimensional materials beyond graphene,” *Acs Nano*, vol. 9, no. 12, pp. 11509–11539, 2015.
- [73] X. Ji, Y. Xu, W. Zhang, L. Cui, and J. Liu, “Review of functionalization, structure and properties of graphene/polymer composite fibers,” *Composites Part A: Applied Science and Manufacturing*, vol. 87, pp. 29–45, 2016.
- [74] J. B. Min, D. L. Harris, and J. Ting, “Advances in ceramic matrix composite blade damping characteristics for aerospace turbomachinery applications,” in *52nd AIAA/ASME/ASCE/AHS/ASC Structures, Structural Dynamics and Materials Conference 19th AIAA/ASME/AHS Adaptive Structures Conference 13t*, p. 1784, 2011.
- [75] A. Sinha and J. Griffin, “Friction damping of flutter in gas turbine engine airfoils,” *Journal of Aircraft*, vol. 20, no. 4, pp. 372–376, 1983.
- [76] G. Gregori, L. Lì, J. A. Nychka, and D. R. Clarke, “Vibration damping of superalloys and thermal barrier coatings at high-temperatures,” *Materials Science and Engineering: A*, vol. 466, no. 1, pp. 256–264, 2007.
- [77] J. Griffin, “Friction damping of resonant stresses in gas turbine engine airfoils,” *Journal of Engineering for Gas Turbines and Power*, vol. 102, no. 2, pp. 329–333, 1980.
- [78] A. Kelly and N. Macmillan, *Strong Solids*. Clarendon Press, third ed., 1986.
- [79] E. P. Petrov, “Analysis of flutter-induced limit cycle oscillations in gas-turbine structures with friction, gap, and other nonlinear contact interfaces,” *ASME Journal of Turbomachinery*, vol. 134, no. 6, p. 061018, 2012.
- [80] A. A. Ferri and W. E. Whiteman, “Free response of a system with negative viscous damping and displacement-dependent dry friction damping,” *Journal of Sound and Vibration*, vol. 306, no. 3, pp. 400–418, 2007.
- [81] C.-H. Menq, J. H. Griffin, and J. Bielak, “The influence of microslip on vibratory response, part ii: A comparison with experimental results,” *Journal of Sound and Vibration*, vol. 107, no. 2, pp. 295–307, 1986.

- [82] B. J. Deaner, M. S. Allen, M. J. Starr, D. J. Segalman, and H. Sumali, “Application of viscous and iwan modal damping models to experimental measurements from bolted structures,” *Journal of Vibration and Acoustics*, vol. 137, no. 2, p. 021012, 2015.
- [83] C. Martel, R. Corral, and R. Ivaturi, “Flutter amplitude saturation by nonlinear friction forces: Reduced model verification,” *ASME Journal of Turbomachinery*, vol. 137, no. 4, p. 041004, 2015.
- [84] U. Olofsson, “Cyclic microslip under unlubricated conditions,” *Tribology International*, vol. 28, no. 4, pp. 207–217, 1995.
- [85] D.-Y. Chiang, “The generalized masing models for deteriorating hysteresis and cyclic plasticity,” *Applied Mathematical Modelling*, vol. 23, no. 11, pp. 847–863, 1999.
- [86] A. Sinha and J. Griffin, “Stability of limit cycles in frictionally damped and aerodynamically unstable rotor stages,” *Journal of Sound and Vibration*, vol. 103, no. 3, pp. 341–356, 1985.
- [87] J.-C. Charlier, X. Blase, and S. Roche, “Electronic and transport properties of nanotubes,” *Reviews of Modern Physics*, vol. 79, pp. 677–732, may 2007.
- [88] M. Dresselhaus, G. Dresselhaus, and P. Avouris, eds., *Carbon Nanotubes*. Springer: Berlin, 2001.
- [89] M. Collet, M. Ouisse, M. Ruzzene, and M. Ichchou, “Floquet–bloch decomposition for the computation of dispersion of two-dimensional periodic, damped mechanical systems,” *International Journal of Solids and Structures*, vol. 48, pp. 2837–2848, oct 2011.
- [90] P. Sheng, *Introduction to wave scattering, localization and mesoscopic phenomena*, vol. 88. Springer Science & Business Media, 2006.
- [91] A. Stone and D. Wales, “Theoretical studies of icosahedral c60 and some related species,” *Chemical Physics Letters*, vol. 128, pp. 501–503, aug 1986.
- [92] L. J. Chen, Q. Zhao, and Z. Q. Gong, “The effects of different defects on vibration properties of single-walled carbon nanotubes,” *Advanced Materials Research*, vol. 225-226, pp. 1133–1136, apr 2011.
- [93] S. K. Georgantzinou, G. I. Giannopoulos, and N. K. Anifantis, “The effect of atom vacancy defect on the vibrational behavior of single-walled carbon nanotubes: A structural mechanics approach,” *Advances in Mechanical Engineering*, vol. 6, p. 291645, jan 2014.
- [94] M.-T. Yang and J. H. Griffin, “A reduced-order model of mistuning using a subset of nominal system modes,” *Journal of Engineering for Gas Turbines and Power*, vol. 123, no. 4, p. 893, 2001.
- [95] B. Leimkuhler and C. Matthews, “Molecular dynamics,” 2015.

- [96] K. Kunc and R. M. Martin, “Ab Initio Force constants of GaAs: A new approach to calculation of phonons and dielectric properties,” *Physical Review Letters*, vol. 48, pp. 406–409, feb 1982.
- [97] D. Sánchez-Portal, E. Artacho, J. M. Soler, A. Rubio, and P. Ordejón, “Ab initio structural, elastic, and vibrational properties of carbon nanotubes,” *Physical Review B*, vol. 59, pp. 12678–12688, may 1999.
- [98] L. Lindsay and D. Broido, “Optimized Tersoff and Brenner empirical potential parameters for lattice dynamics and phonon thermal transport in carbon nanotubes and graphene,” *Physical Review B*, vol. 81, no. 20, p. 205441, 2010.
- [99] J. Tersoff, “New empirical approach for the structure and energy of covalent systems,” *Physical Review B*, vol. 37, pp. 6991–7000, apr 1988.
- [100] J. Tersoff, “Modeling solid-state chemistry: Interatomic potentials for multicomponent systems,” *Physical Review B*, vol. 39, pp. 5566–5568, mar 1989.
- [101] D. W. Brenner, O. A. Shenderova, J. A. Harrison, S. J. Stuart, B. Ni, and S. B. Sinnott, “A second-generation reactive empirical bond order (rebo) potential energy expression for hydrocarbons,” *Journal of Physics: Condensed Matter*, vol. 14, no. 4, p. 783, 2002.
- [102] S. J. Stuart, A. B. Tutein, and J. A. Harrison, “A reactive potential for hydrocarbons with intermolecular interactions,” *The Journal of chemical physics*, vol. 112, no. 14, pp. 6472–6486, 2000.
- [103] S. Plimpton, “Fast parallel algorithms for short-range molecular dynamics,” *Journal of Computational Physics*, vol. 117, pp. 1–19, mar 1995.
- [104] H. K. Khalil, *Nonlinear systems*. Upper Saddle River, NJ: Prentice Hall, 3 ed., 2002.
- [105] A. S. Phani, J. Woodhouse, and N. A. Fleck, “Wave propagation in two-dimensional periodic lattices,” *The Journal of the Acoustical Society of America*, vol. 119, pp. 1995–2005, apr 2006.
- [106] S. Friedberg, A. Insel, and L. Spence, *Linear algebra*. Upper Saddle River, NJ: Prentice Hall, 4 ed., 2003.
- [107] A. Sinha and Y. Bhartiya, “Modeling geometric mistuning of a bladed rotor: Modified modal domain analysis,” in *IUTAM Symposium on Emerging Trends in Rotor Dynamics*, pp. 177–184, Springer, 2011.
- [108] Y. Liang, H. Lee, S. Lim, W. Lin, K. Lee, and C. Wu, “Proper orthogonal decomposition and its applications—part i: theory,” *Journal of Sound and Vibration*, vol. 252, pp. 527–544, may 2002.
- [109] A. Chatterjee, “An introduction to the proper orthogonal decomposition,” *Current science*, pp. 808–817, 2000.

- [110] J. Ma, D. Alfè, A. Michaelides, and E. Wang, “Stone-wales defects in graphene and other planar sp²-bonded materials,” *Physical Review B*, vol. 80, jul 2009.
- [111] J. Rumble, ed., *CRC handbook of chemistry and physics*. Boca Raton, FL: CRC Press, 2017.
- [112] W. Humphrey, A. Dalke, and K. Schulten, “VMD: Visual molecular dynamics,” *Journal of Molecular Graphics*, vol. 14, pp. 33–38, feb 1996.
- [113] M. Pastor, M. Binda, and T. Harčarik, “Modal assurance criterion,” *Procedia Engineering*, vol. 48, pp. 543–548, 2012.
- [114] P. B. Allen and J. Kelner, “Evolution of a vibrational wave packet on a disordered chain,” *American Journal of Physics*, vol. 66, pp. 497–506, jun 1998.
- [115] J. A. Rodriguez-Manzo and F. Banhart, “Creation of individual vacancies in carbon nanotubes by using an electron beam of 1 Å diameter,” *Nano Letters*, vol. 9, pp. 2285–2289, jun 2009.
- [116] A. V. Krasheninnikov, K. Nordlund, and J. Keinonen, “Production of defects in supported carbon nanotubes under ion irradiation,” *Physical Review B*, vol. 65, apr 2002.
- [117] A. Hashimoto, K. Suenaga, A. Gloter, K. Urita, and S. Iijima, “Direct evidence for atomic defects in graphene layers,” *Nature*, vol. 430, pp. 870–873, aug 2004.
- [118] M. Sammalkorpi, A. Krasheninnikov, A. Kuronen, K. Nordlund, and K. Kaski, “Mechanical properties of carbon nanotubes with vacancies and related defects,” *Physical Review B*, vol. 70, no. 24, p. 245416, 2004.
- [119] Z.-Q. Qu, *Model order reduction techniques with applications in finite element analysis*. London: Springer Science & Business Media, 2013.
- [120] A. Krasheninnikov and F. Banhart, “Engineering of nanostructured carbon materials with electron or ion beams,” *Nature materials*, vol. 6, no. 10, p. 723, 2007.
- [121] T. D. Yuzvinsky, W. Mickelson, S. Aloni, G. E. Begtrup, A. Kis, and A. Zettl, “Shrinking a carbon nanotube,” *Nano Letters*, vol. 6, pp. 2718–2722, dec 2006.
- [122] D. J. Evans and B. L. Holian, “The nose–hoover thermostat,” *The Journal of Chemical Physics*, vol. 83, pp. 4069–4074, oct 1985.
- [123] D. C. Kammer, “Test-analysis model development using an exact modal reduction,” *International Journal of Analytical and Experimental Modal Analysis*, vol. 2, no. 4, pp. 174–179, 1987.
- [124] J. O’Callahan, P. Avitabile, and R. Riemer, “System equivalent reduction expansion process (serep),” in *Proceedings of the 7th international modal analysis conference*, vol. 1, pp. 29–37, Union College Schnectady, NY, 1989.

- [125] C.-K. Li and R.-C. Li, “A note on eigenvalues of perturbed hermitian matrices,” *Linear Algebra and its Applications*, vol. 395, pp. 183–190, jan 2005.
- [126] N. Bouhaddi and R. Fillod, “Model reduction by a simplified variant of dynamic condensation,” *Journal of Sound and Vibration*, vol. 191, pp. 233–250, mar 1996.
- [127] N. A. Koratkar, J. Suhr, A. Joshi, R. S. Kane, L. S. Schadler, P. M. Ajayan, and S. Bartolucci, “Characterizing energy dissipation in single-walled carbon nanotube polycarbonate composites,” *Applied physics letters*, vol. 87, no. 6, p. 063102, 2005.
- [128] E. T. Thostenson and T.-W. Chou, “Aligned multi-walled carbon nanotube-reinforced composites: processing and mechanical characterization,” *Journal of physics D: Applied physics*, vol. 35, no. 16, p. L77, 2002.
- [129] S. C. Tjong, *Carbon Nanotube Reinforced Composites*. Wiley-VCH Verlag GmbH & Co. KGaA, may 2009.
- [130] B. K. Choi, G. H. Yoon, and S. Lee, “Molecular dynamics studies of cnt-reinforced aluminum composites under uniaxial tensile loading,” *Composites Part B: Engineering*, vol. 91, pp. 119–125, 2016.
- [131] N. Silvestre, B. Faria, and J. N. C. Lopes, “Compressive behavior of cnt-reinforced aluminum composites using molecular dynamics,” *Composites Science and Technology*, vol. 90, pp. 16–24, 2014.
- [132] S. R. Bakshi, D. Lahiri, and A. Agarwal, “Carbon nanotube reinforced metal matrix composites-a review,” *International materials reviews*, vol. 55, no. 1, pp. 41–64, 2010.
- [133] T. Kawaguchi and H. Matsukawa, “Dynamical frictional phenomena in an incommensurate two-chain model,” *Physical Review B*, vol. 56, no. 21, p. 13932, 1997.
- [134] A. Bylinskii, D. Gangloff, I. Counts, and V. Vuletić, “Observation of aubry-type transition in finite atom chains via friction,” *Nature materials*, vol. 15, no. 7, p. 717, 2016.
- [135] J. Suhr, N. Koratkar, P. Keblinski, and P. Ajayan, “Viscoelasticity in carbon nanotube composites,” *Nature materials*, vol. 4, no. 2, p. 134, 2005.
- [136] R. J. Guyan, “Reduction of stiffness and mass matrices,” *AIAA journal*, vol. 3, no. 2, pp. 380–380, 1965.
- [137] M. S. Daw and M. I. Baskes, “Embedded-atom method: Derivation and application to impurities, surfaces, and other defects in metals,” *Physical Review B*, vol. 29, no. 12, p. 6443, 1984.
- [138] Y. Mishin, D. Farkas, M. Mehl, and D. Papaconstantopoulos, “Interatomic potentials for monoatomic metals from experimental data and ab initio calculations,” *Physical Review B*, vol. 59, no. 5, p. 3393, 1999.
- [139] J. E. Lennard-Jones, “Cohesion,” *Proceedings of the Physical Society*, vol. 43, no. 5, p. 461, 1931.

- [140] J. R. Shewchuk *et al.*, “An introduction to the conjugate gradient method without the agonizing pain,” 1994.
- [141] R. Fletcher and C. M. Reeves, “Function minimization by conjugate gradients,” *The computer journal*, vol. 7, no. 2, pp. 149–154, 1964.
- [142] L. Armijo, “Minimization of functions having lipschitz continuous first partial derivatives,” *Pacific Journal of mathematics*, vol. 16, no. 1, pp. 1–3, 1966.
- [143] P. Wolfe, “Convergence conditions for ascent methods,” *SIAM review*, vol. 11, no. 2, pp. 226–235, 1969.
- [144] P. Wolfe, “Convergence conditions for ascent methods. ii: Some corrections,” *SIAM review*, vol. 13, no. 2, pp. 185–188, 1971.
- [145] J. Stein, B. Lenczowski, N. Fréty, and E. Anglaret, “Mechanical reinforcement of a high-performance aluminium alloy aa5083 with homogeneously dispersed multi-walled carbon nanotubes,” *Carbon*, vol. 50, no. 6, pp. 2264–2272, 2012.
- [146] S. Cahangirov, C. Ataca, M. Topsakal, H. Sahin, and S. Ciraci, “Frictional figures of merit for single layered nanostructures,” *Physical review letters*, vol. 108, no. 12, p. 126103, 2012.
- [147] S. Aubry, “The twist map, the extended frenkel-kontorova model and the devil’s staircase,” *Physica D: Nonlinear Phenomena*, vol. 7, no. 1-3, pp. 240–258, 1983.
- [148] M. Carfagni, E. Lenzi, and M. Pierini, “The loss factor as a measure of mechanical damping,” in *Proceedings-spie the international society for optical engineering*, vol. 1, pp. 580–284, SPIE - the international society for optics and photonics, 1998.

Vita

Robert B. Hudson

Education

The Pennsylvania State University, University Park, PA

Ph.D., Mechanical Engineering — *expected August 2018*

M.S., Mechanical Engineering — May 2017

University of Rochester, Rochester, NY

B.S., Mechanical Engineering — May 2014

cum laude, Tau Beta Pi, With High Distinction in Engineering

B.A., Mathematics — May 2014

cum laude, With Distinction in Mathematics

Awards and Honors

University Graduate Fellowship — *The Pennsylvania State University*, 2014

College of Engineering Fellowship — *The Pennsylvania State University*, 2014

Wilder Trustee Scholarship for Overall Excellence — *University of Rochester*, 2010

National Merit Scholarship — *National Merit Scholarship Corporation*, 2010

Publications and Presentations

Hudson, R. B., A. Sinha. An Order Reduction Method for Single Walled Carbon Nanotubes with Multi-Vacancy Defects. *Accepted for publication by Carbon*

Hudson, R. B., A. Sinha. Vibration of Carbon Nanotubes with Defects: Order Reduction Methods. *Proceedings of the Royal Society A*, 474(2211):20170555, March 2018.

Hudson, R., A. Sinha. Frictional Damping of Flutter: Microslip Versus Macroslip. *Journal of Vibration and Acoustics*, 138(6):061010, December 2016.

Hudson, R., A. Sinha. Frictional Damping of Flutter: Microslip Versus Macroslip. In: *Proceedings of the 2016 ASME International Design Engineering Technical Conferences and Computers and Information in Engineering Conference (IDETC/CIE 2016)*, August 21–24, 2016.